UC Davis
UC Davis Electronic Theses and Dissertations

Title

Using microARPES and Machine Learning to Accelerate Experiments and Elucidate the Local Electronic and Chemical Structure of Quantum Materials

Permalink

https://escholarship.org/uc/item/1207d032

Author

Staab, Matthew Craig

Publication Date

2024

Peer reviewed|Thesis/dissertation

eScholarship.org Powered by the California Digital Library
University of California

Using microARPES and Machine Learning to Accelerate Experiments and Elucidate the Local Electronic and Chemical Structure of Quantum Materials

By

MATTHEW C. STAAB
DISSERTATION

Submitted in partial satisfaction of the requirements for the degree of

DOCTOR OF PHILOSOPHY

in

Physics

in the

OFFICE OF GRADUATE STUDIES

of the

UNIVERSITY OF CALIFORNIA

DAVIS

Approved:

Inna M. Vishik, Chair

Valentin Taufour

Rajiv R.P. Singh

Committee in Charge

2024

Contents

Abstract **iv**

Acknowledgments **vi**

Funding Acknowledgments **ix**

List of Figures **xi**

1 Overview of Photoemission Experiments **1**
1.1 Introduction . . . 1
1.2 Theory of Photoemission . . . 2
1.2.1 Three-Step Model . . . 2
1.2.2 Measuring Binding Energy and Parallel Momentum . . . 3
1.2.3 Perpendicular Momentum . . . 5
1.3 Photoemission Intensity Formula . . . 8
1.3.1 Energy and Momentum Resolution Effects . . . 10
1.3.2 Geometry of ARPES Data in Momentum Space . . . 12
1.3.3 Spatially resolved ARPES . . . 13
1.3.4 X-ray Photoemission Spectroscopy (XPS) . . . 14
1.3.5 Surface Sensitivity . . . 14
1.4 Anatomy of an ARPES Experiment . . . 15
1.4.1 Sample Mounting and Ultra-High Vacuum Preparation . . . 15
1.4.2 The ARPES Chamber . . . 18
1.5 Beamline Endstations . . . 25

2 Quantum Materials **27**
2.1 Introduction to Quantum Materials . . . 27
2.2 Light-Like Dispersions in Quantum Materials . . . 27
2.2.1 Graphene . . . 29
2.2.2 Topological Insulators . . . 29
2.2.3 Dirac Semimetals . . . 31
2.2.4 Weyl Semimetals . . . 31
2.3 Momentum-Resolved Spectroscopy . . . 32

3 Symmetry-Enforced Fermi Surface Degeneracies Observed in the Purported Time-Reversal Symmetry-Broken Superconductor $LaNiGa_2$ **34**
3.1 Introduction . . . 35
3.2 Methods . . . 36
3.3 Results . . . 40
3.4 Discussion . . . 43
3.5 Conclusions . . . 49

4 AARDVARK: Adaptive Automation and Real-time Data Visualization for All Research Kit **50**
4.1 Introduction . . . 50
4.2 Methods . . . 52
4.2.1 Uniform Manifold Approximation and Projection (UMAP) . . . 52
4.2.2 Gaussian Process Regression . . . 54
4.3 Results . . . 56
4.4 Discussion . . . 57
4.5 Conclusions . . . 59

5 Spatial Heterogeneity and Machine Learning Analysis of $Co_3Sn_2S_2$ **60**
5.1 Introduction . . . 60
5.2 Machine Learning Identification of Surface Heterogeneity . . . 64
5.2.1 k-Means Clustering . . . 64
5.2.2 Dimensionality Reduction . . . 65
5.3 Analysis of ARPES and XPS Spectral Correlation . . . 67
5.4 Conclusions . . . 70

6 Conclusions **73**

Abstract

Photoemission experiments are an information rich probe into the electronic structure of materials. Angle-resolved photoemission spectroscopy (ARPES) focusing on the valence bands and X-ray photoemission spectroscopy (XPS) focusing on tightly bound core electrons give a wholistic view into the features of occupied electronic states. In this dissertation I: (1) perform the first ARPES studies of $LaNiGa_2$, (2) develop an autonomous machine learning control system to improve the speed at which ARPES data can be taken, and (3) analyze the correlation between spatially resolved XPS and ARPES studies on $Co_3Sn_2S_2$. These together demonstrate the utility of ARPES and XPS for studying quantum materials as well as incorporating modern machine learning practices to extract otherwise hidden data from these rich datasets.

$LaNiGa_2$ is an unconventional superconductor that is reported to break time-reversal symmetry in its superconducting state, despite the absence of nearby magnetism. $LaNiGa_2$ has a nonsymmorphic Cmcm space group, which enforces symmetry-protected electronic degeneracies in its band structure. ARPES measurements across the three-dimensional Brillouin zone reveal features broadly consistent with density functional theory calculations. These measurements provide direct evidence for both predicted symmetry-enforced degeneracies and accidental near-degeneracies throughout the electronic structure. These findings suggest that the interplay between these degeneracies and the Fermi surface topology may play a role in the superconducting pairing mechanism of $LaNiGa_2$. This work on $LaNiGa_2$, detailed in Chapter 3, lead to two publications [1, 2].

ARPES experiments often require substantial time to locate optimal sample regions for detailed study. AARDVARK, an autonomous machine learning control system, addresses this challenge by analyzing data in real time to guide measurements efficiently. The system uses uniform manifold approximation and projection (UMAP) for dimensionality reduction, followed by Gaussian process modeling to map spatial inhomogeneity. This pipeline reduces the number of measurements needed by approximately 75% compared to traditional grid-search approaches while providing the same spatial heuristics to users. AARDVARK demonstrates the potential for integrating machine learning into photoemission spectroscopy workflows, enhancing the speed of collection of spatially resolved studies. This project is detailed in Chapter 4 and constitutes a manuscript

that at the time of writing this dissertation is in preparation to be submitted for peer review.

$Co_3Sn_2S_2$ exhibits surface heterogeneity with distinct sulfur, tin, and mixed terminations, which influence its local electronic structure. ARPES and XPS measurements were performed across a $500\,\mu m \times 300\,\mu m$ area using a micro-focused beam ($15\,\mu m \times 15\,\mu m$), providing spatially resolved insight into the correlation between valence and core-level spectra. By combining traditional spectral integration methods with machine learning, the analysis captures termination-dependent variations in the electronic structure, forming a basis for interpreting spatial heterogeneity in hyperspectral datasets. These experiments highlight the critical role of synchrotron light sources in enabling simultaneous, high-resolution ARPES and XPS measurements, which are essential for studying spatially complex quantum materials. The study of surface heterogeneity in $Co_3Sn_2S_2$ in Chapter 5 is a portion of a manuscript that is still being prepared at the time of writing this dissertation.

Acknowledgments

A PhD is something like a time machine: One day you enter a program, often moving across the country or world to do so, and after what feels simultaneously like an eternity and no time at all you look up and 5, 6, 7, even 8 years may have passed. In this span it is likely that some life-altering events will happen: family members passing away, finding a person you want to spend forever with, birth of children, loss of friends, even a world-stopping pandemic. I had both the good fortune and misfortune to have all of these and more happen during my PhD. If you, reader, are pursuing a PhD or in a similar multi-year focused endeavor let this be a reminder to call your loved ones often, take time to meet new people, spend time with friends, and enjoy this crazy ride of life while it lasts.

First, I want to thank my advisor Inna Vishik. Thank you for your close guidance during my first year, giving me small coding projects to make tools for the group, and having me join on every beamtime. As I matured as a scientist you seamlessly found ways for me to input my ideas without letting me go down fruitless rabbit holes for too long. I often tell the joke to friends that one day during my first year you said something to the effect of, "[Our group] doesn't focus on software and making the tools, we utilize them to target our scientific goals". Regardless of that, I kept coming back to you with new ideas for tools or software that I could write. Your continued open mindedness to me exploring these topics allowed me to flourish in my own niche and I think we accomplished some very interesting projects because of it. I am deeply grateful for your mentorship, advise, and expertise during this program.

Thank you to all the other Vishik Lab members. Especially to Adam Gross for teaching me the ways of the 6eV laser as we built it my first year. Sudheer Sreedhar, for all of your advice on XPS and ARPES and our great discussions driving to beamtime. To Antonio Rossi for teaching me all night during those first beamtimes while simultaneously running the experiment. To Bobby Prater, I'm so happy you joined the group, bouncing ideas off you in the office made the PhD much more enjoyable. To Journey Byland, your knowledge of obscure material growth information and tools continues to surprise me. To Kevin Fillhouer for keeping the laser going after Adam and having great spontaneous talks in the hallway. Thank you to the rest of the group and always remember to have a chocolate before you cleave, listen to Linkin Park when

going to beamtime, because in the end it doesn't even matter.

For sparking my interest in ARPES I want to thank my undergraduate research advisor Elaine Li. After emailing many people about doing some undergraduate research, you are the only one who responded. I should also thank Marshall Campbell, who you sent to have an initial meeting with me, for seeing some possibility in me. Little did I know it then, this was truly a turning point in my life. One day during our meeting I noticed you putting sticky notes in a book about ARPES and asked you what it was. I thought to myself that if my professor I respect so well thinks this technique is so interesting maybe I should look into it for my graduate school applications. Thank you for bringing me in to your "army of undergrads" and lighting my research fire.

Thank you to my undergraduate academic advisor and quantum mechanics professor Greg Sitz. Your intuitive explanations, love for the subject, and passion for teaching were pivotal in forming my understanding of physics. I am deeply grateful for the many office hours I spent listening to you explain quantum mechanics.

I also want to thank all of the faculty and staff I have interacted with in the physics and astronomy department. Especially to the graduate student coordinators Angela Sharma and Lenna Crabbe-Charlesworth, the chief academic officer Trace Lade, fiscal officer and personnel coordinator Falicia Savala, you all keep the department running in ways the students and faculty can never fully understand all while answering every question we throw at you. Thank you to all of the professors who supported me in many ways during this program, especially Richard Scalletar, Warren Pickett, Rajiv Singh, and Valentin Taufour.

Thank you to Eli Rotenberg for giving me the valuable experience of making AARDVARK for the Maestro beamline. My time at the ALS working on AARDVARK was extremely rewarding. Your passion for ARPES and continuing to keep pushing the edge is remarkable. Thank you to Aaron Bostwick and Chris Jozwiak as well for all their mentorship and guidance operating the beamline. Thank you to the compute group of the ALS for their assistance tackling such a complex topic as beamline automation, especially Alex Hexemer, Tanny Esparza, Weibke Koepp, Dylan McReynolds. Thank you to all of the other beamline scientists at ALS and SSRL who spend countless nights awake helping me and others troubleshoot during stressful beamtimes, particularly Jonathan Denlinger, Makoto Hashimoto, Donghi Lu, and Alexei Fedorov. Finally thank you to the Maestro lunch group for all the wonderful discussion and variety of meals we had. Those lunches looking over the Bay while sharing home cooked meals and wonderful stories will forever be phenomenal memories.

The support and friendship that my cohort fostered in the program was absolutely unwavering. I am so grateful for the lifelong friendships I have made with you all. Especially thank you to Samantha and JB Abbott for organizing gatherings and particularly the "Hot Ones" parties where our cohort gathered, ate more than 200 very spicy chicken wings, shared feelings, and stayed connected. Thank you again to Bobby Prater, this time as a friend (and Dungeon Master), you and Alaina have brought so much support and joy

to our friend group. Thank you to Jean Donet and Ari Storm, Chris McPherson, Hyun-Soo Kim, Phurba Sherpa, Cameron Chaffey, Bob Wang, Ian Lim, Spence Norwood, Erin Huntzinger, Fiona McCluskey, Joe Yazbeck, M.A. Mort, Rodrigo Alvez, Saeahram Yoo, Jamie Barnhill, Michael Spiegel. An especially large thank you to Zach Sweger, for bringing Priti and I together as our officiant, being a thoughtful and caring friend, and a great scientist. You all have made a fantastic family away from home and I am forever thankful for the memories we have made.

Thank you to my family, all 14 of my siblings, all ∞ of my cousins, in-laws, nephews, nieces. Especially to my brother James, I wish you were still with us to give me a high-4 at the end of this. To my parents, Pam Hadley, Bob Staab, Robin Staab, and Johnny Hadley for believing in me to go on this crazy 5.5 year adventure across the country and all of your help along the way. And to my grandparents, especially my Granny Nancy Staab, for all of the kindness, curiosity, and passion you taught me to have, you will be deeply missed. And to my other Granny Deni Hadley, I am so happy for the years I knew you and that you were able to meet Priti before you passed, we miss you. Thank you to my best friend Josh McIntosh-Beatson, for always being there for me when I need you and all of the amazing discussions we have. To my daughter Chloe, I am so excited for this new chapter of life spending time with you. I am already infinitely proud to be your father, I know you will grow into an amazing person.

Finally but most importantly I want to thank my wife Priti. It is clear now that the reason for me doing this PhD was not for the degree itself, but to meet you. You have supported me in ways I did not know I could be or know that I needed to be. Through coursework, research ideas, long nights of beamtime, my constant side projects, family members passing away, and long nights with Chloe as I finish writing this. I am eternally grateful for meeting you and cannot wait to see what the rest of life has in store for our family. You will always be my eigenket.

Funding Acknowledgments

Chapter 3, $LaNiGa_2$: The natural-cleave measurements in this manuscript were supported by AFOSR Grant No. FA9550-18-1-0156, while the thin-edge cleave measurements were supported by the Alfred P. Sloan Foundation(FG-2019-12170). Most of the experiments were performed at the Stanford Synchrotron Radiation Lightsource, SLAC National Accelerator Laboratory, which is supported by the U.S. Department of Energy, Office of Science, Office of Basic Energy Sciences under Contract No. DE-AC02-76SF00515. This work was also supported by the advanced lightsource (ALS) graduate fellowship and the Dean's faculty fellowship at UC Davis. The Advanced Light Source is a DOE Office of Science User Facility under contract no. DE-AC02-05CH11231.

Chapter 5, $Co_3Sn_2S_2$: This was supported by the U.S.-Israel Binational Science Foundation grant 2020067. This work was also supported by the advanced lightsource (ALS) graduate fellowship and the Dean's faculty fellowship at UC Davis. The Advanced Light Source is a DOE Office of Science User Facility under contract no. DE-AC02-05CH11231. Experiments were also performed at the Stanford Synchrotron Radiation Lightsource, SLAC National Accelerator Laboratory, which is supported by the U.S. Department of Energy, Office of Science, Office of Basic Energy Sciences under Contract No. DE-AC02-76SF00515.

Chapter 4, AARDVARK: This was supported by the U.S.-Israel Binational Science Foundation grant 2020067. This work was also supported by the advanced lightsource (ALS) doctoral fellowship in residence and the Dean's faculty fellowship at UC Davis. The Advanced Light Source is a DOE Office of Science User Facility under contract no. DE-AC02-05CH11231.

Building 6eV laser ARPES: DOE contract number DE-SC0014697

List of Figures

1.1 Schematic description of the three-step model for photoemission. 2
1.2 Measured and interpreted quantities in ARPES. 4
1.3 Fermi surface reconstruction using photon energy dependence. 6
1.4 $k_\perp$ dispersions compared to direct ARPES. 6
1.5 Section of momentum space probed by ARPES 7
1.6 Constant energy maps at multiple photon energies of $LaNiGa_2$. 8
1.7 Anatomy of an ARPES system. 16
1.8 Straight vs curved slits for hemispherical analyzer. 24

2.1 Schematic depiction of quantum material light-like electronic structure. 28
2.2 ARPES spectrum of Bi_2Se_3. 30

3.1 Predicted Fermiology and Nodal Plane Features 37
3.2 Laue image of $LaNiGa_2$. 38
3.3 Sample Dimensions and XPS 39
3.4 Observed Fermiology for selected planes in BZ. 41
3.5 Band merging in momentum at zone boundaries. 42
3.6 Band merging in energy, thin-edge cleave. 43
3.7 Linear crossings for cuts perpendicular to nodal plane. 44
3.8 Orbital projections of $LaNiGa_2$'s band structure without SOC. 45

4.1 Schematic overview for the the AARDVARK system. 51
4.2 Colorized UMAP embeddings. 53
4.3 Progression of an AARDVARK scan on ARPES data. 55
4.4 Progression of an AARDVARK scan on XPS data. 56
4.5 Comparison of AARDVARK operation on ARPES data with random or grid search. 57

5.1 $Co_3Sn_2S_2$ crystal structure, terminations, and Brillouin zone. 61
5.2 Spatial Dependence of ARPES and XPS on $Co_3Sn_2S_2$. 62
5.3 Correlation of XPS and ARPES spectral features. 62
5.4 ARPES and XPS of the mixed termination. 63
5.5 Dimensionality reduction methods applied to $Co_3Sn_2S_2$. 66
5.6 Silhouette score differences of PCA and UMAP embeddings. 67
5.7 Spectral features relationship to UMAP embeddings. 68
5.8 UMAP Colorization of XPS and ARPES spectra of $Co_3Sn_2S_2$. 69
5.9 Spatial visualizations of machine learning on $Co_3Sn_2S_2$. 70
5.10 Relationship of ARPES and XPS spectra in $Co_3Sn_2S_2$. 71

Chapter 1

Overview of Photoemission Experiments

1.1 Introduction

Einstein did not win his Nobel prize for any of the results that the general public associates with him[1]: "$E = mc^2$", "his mustache", "theory of relativity", "string theory", "math", "2 Chickens and a goat?"[2], "quantum physics", "black holes", "some crazy theory that no one understands", "Don't ask us, aren't you the physicist? Are you done with the thesis yet?"[3]. In fact, Einstein won the 1921 Nobel prize, "for his services to Theoretical Physics, and especially for his discovery of the law of the photoelectric effect" [3]. Indeed, not even Einstein winning the Nobel prize for the photoelectric effect is enough for people to remember it. This trivia fact is perhaps the only relatable thing I can mention to make the motivation for photoemission studies interesting to a non-physicist audience. Thankfully no one from such an audience will ever choose of their own free will to read dissertation discussing the utility of photoemission experiments in the modern day on quantum materials and how machine learning can help us dive deeper into these information rich datasets. Photoemission studies have come a long way since 1921 and the development of angle-resolved photoemission spectroscopy (ARPES) has enabled the only direct and generally applicable method for probing the energy and momentum resolved single-particle behavior of electrons in a material. Using only high-school level algebraic equations to conserve momentum and energy we can understand very precisely how electrons are moving inside of materials.

[1] I solicited these responses from friends and family.
[2] Not sure how that one came up... However it would be unscientific of me to exclude showing the outliers of the data.
[3] Ouch.

My intention with this chapter is to provide a foundation for understanding photoemission experiments. There are two main parts of this chapter: (1) The theoretical basis of photoemission, experimental limitations, and the types of photoemission experiments used in this dissertation. (2) An "anatomy" of the most common ARPES experimental setups to illustrate all of the important components of the experiment. The second half is intended as as resource for future students to quickly find the subsection they are curious about and have a brief introduction with relevant terms to search for more details. For more information there exist many wonderful reviews of ARPES and its application to many materials, a few of my recommendations are refs. [4, 5, 6].

1.2 Theory of Photoemission

1.2.1 Three-Step Model

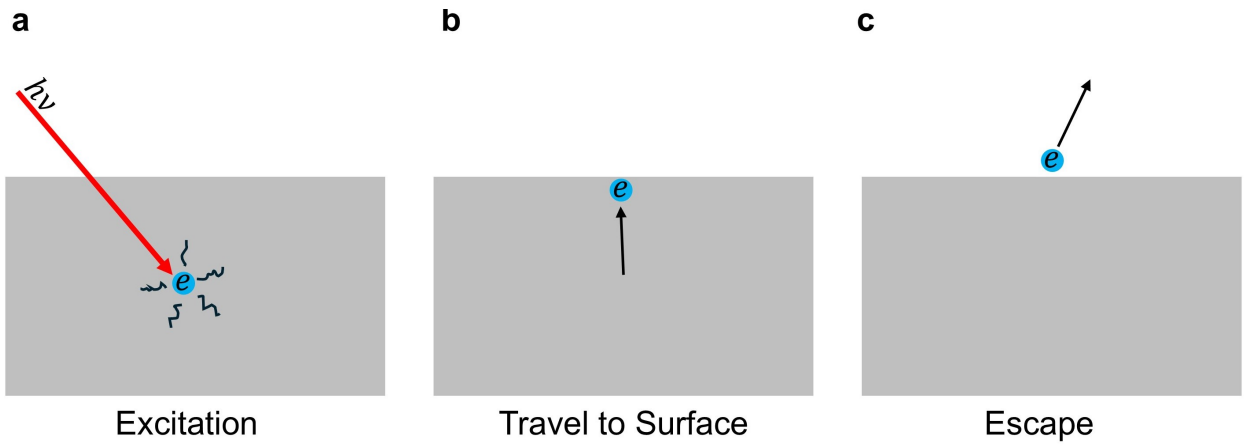

Figure 1.1: Schematic description of the three-step model for photoemission. (a) Step 1: Optical excitation of the electron in the material to a higher energy state. (b) Step 2: Travel from the initial bulk position to the surface. (c) Step 3: Escape into the vacuum as a free electron.

In the most general sense, the process of photoemission involves an incident light source interacting with a material in a way that causes the ejection of an electron into a free final state. This emission process can be treated in a single step as a direct transition mediated by an interaction with an incident photon of an initial N-body wavefunction where all of the electrons are bound in the material to a final excited state where there is a high probability of detecting an emitted electron. In practice, it is typically more convenient to break this emission up into three steps which correspond to intuitively significant steps[4] I have provided a schematic of the three-step model in Figure 1.1 which describes the photoemission through the following

[4]Ironically, the original coining of the three-step model in Berglund and Spicer [7] the paper begins with "Photoemission from solids is a two-step process". In modern discussions, we break their second step into two and hence have a three-step model.

processes:

1. An incident photon causes an electron bound in the material at some energy $E_{\mathbf{k}}$ and momentum $\mathbf{k}$ to transition to a higher final energy[5] $E_f(\mathbf{k})$.

2. The electron travels to the surface of the material, possibly being scattered by other electrons or ions. The inelastic mean free path (IMFP) λ_{IMFP} (typical values for the IMFP are around $1nm$ [8]) of electrons in the material exponentially prohibits electrons reaching the surface of the material without scattering, making ARPES extremely surface sensitive. The surface sensitivity is discussed further in Section 1.3.5.

3. The electron escapes the surface of the material and is approximated as a free-electron plane wave. The potential energy shift of the from being within the material to outside is often approximated by a constant V_0 called the inner potential. The inner potential will be discussed more in the perpendicular momentum Section 1.2.3.

1.2.2 Measuring Binding Energy and Parallel Momentum

The fundamental formulae of photoemission experiments can be derived using only the principles of energy and momentum conservation. We begin by defining the electron's initial energy while bound in the material to be E_B and it's momentum to be $\mathbf{k}$ with in plane component $\mathbf{k}_{||}$ and out of plane component $\mathbf{k}_{\perp}$ relative to the plane of the surface of the material. The electron after being emitted from the material will have some kinetic energy E_{kin} and final state momentum $\mathbf{k}_f$. There is only a change in potential along the direction perpendicular to the surface of the material which means that the parallel momentum must be conserved during the emission $k_{f,||} = k_{||}$. Using simple trigonometry with the angle of emission θ measured with respect to the surface normal we find:

$$
\begin{aligned}
E_{\text{kin}} &= \frac{\hbar^2 |\mathbf{k}|^2}{2m} \\
E_{\text{kin}} &= \frac{\hbar^2 |\mathbf{k}_{||} \sin(\theta)|^2}{2m} \\
\mathbf{k}_{||} &= \frac{1}{\hbar}\sqrt{2mE_{\text{kin}}}\sin(\theta)
\end{aligned}
\tag{1.1}
$$

From equation 1.1 we can take the experimentally observable kinetic energy E_{kin} and emission angle θ and recover the in plane momentum that the electron had while inside the sample. Using energy conservation

[5] While the photon does impart some momentum into the electron it can generally be neglected as discussed in Section 1.2.2.

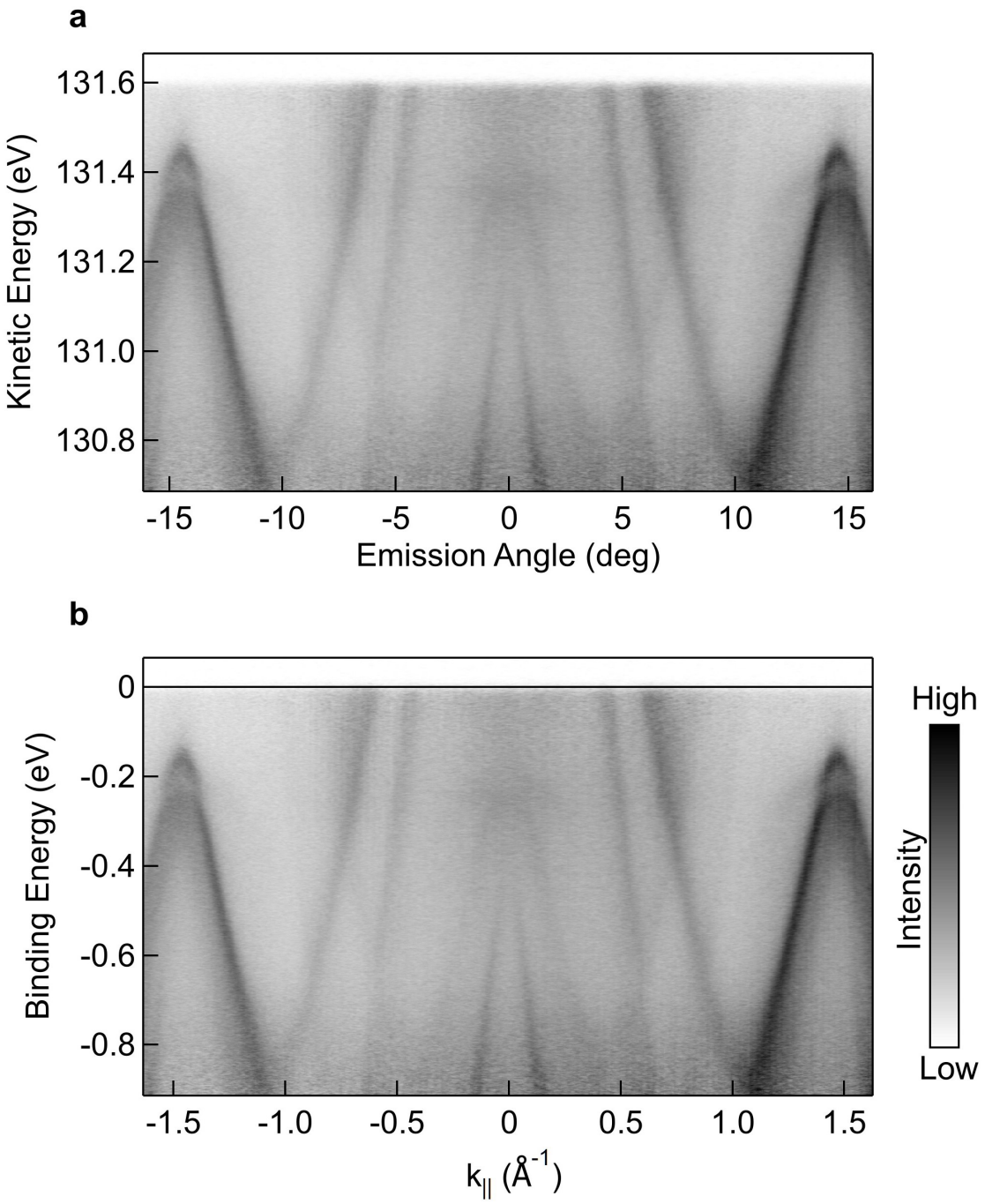

Figure 1.2: Measured and interpreted quantities in ARPES. (a) A raw ARPES spectrum of $LaNiGa_2$ using 136eV photons showing the intensity as a function of the observed emission angle and kinetic energy. (b) The same ARPES data with the axes converted using equations 1.1 and 1.2 to display the binding energy and parallel momentum. It is common for ARPES to report the wave number (k, in Å^{-1}) instead of the momentum ($p = \hbar k$).

we can find the binding energy the electron had inside the material E_B with respect to the photon energy $h\nu$ and the work function ϕ:

$$E_B = h\nu - \phi - E_{\text{kin}} \tag{1.2}$$

In practice, the kinetic energy of the electron is measured with respect to the work function of the analyzer as that is the relevant electronic reference point in the detector. This has the advantage that means the Fermi energy E_F will be measured at the same kinetic energy for all materials measured with the same ARPES system and at the same photon energy. The material's work function is still relevant to the energetic cost of emission and must be taken into account to determine the minimum kinetic energy electrons that can be emitted for a given photon energy (more details are given in Section 1.4). Measuring the exact binding energy reference during an experiment is most commonly done by measuring a Fermi crossing and fitting a Fermi function to the curve. In cases where a gap is being measured we must take care to perform an equivalent parameter measurement on piece of a polycrystalline metal such as gold or copper so that a Fermi level can be found and any angle dependent detector variations can be corrected for.

In Figure 1.2 I show an example of what the conversion looks like between the observed quantities (kinetic energy, emission angle) and the desired information (biding energy, parallel momentum). The ARPES community generally converts the parallel momentum to a wavenumber, referencing k, in Å^{-1} instead of p. In this example, the Fermi energy ($E_B = 0$) was found by observing the kinetic energy where the metallic bands sharply drop in intensity.

1.2.3 Perpendicular Momentum

In photoemission experiments the perpendicular component of the electron's momentum is not strictly conserved due to the potential energy change by escaping the sample. This potential difference is referred to as the "inner potential" V_0 and is phenomenologically determined in most experiments. The out of plane momentum conservation is altered by this term in the following way:

$$\frac{\hbar^2 \mathbf{k}_{f,\perp}^2}{2m} = \frac{\hbar^2 (\mathbf{k}_f \cos(\theta))^2}{2m} = E_{\text{kin}} \cos^2(\theta) = \frac{\hbar^2 \mathbf{k}_{\perp}^2}{2m} - V_0$$

$$\mathbf{k}_{\perp} = \frac{1}{\hbar} \sqrt{2m \left(E_{\text{kin}} cos^2(\theta) + V_0\right)} \tag{1.3}$$

There are two factors that I will draw attention to about the above perpendicular momentum equation: (1) The dependence on E_{kin} and therefore $h\nu$. (2) The determination of the inner potential V_0.

Combining equations 1.2 and 1.3 it is clear that the perpendicular momentum of photoemitted electrons has an offset square root dependence on the photon energy $k_{\perp} \propto \sqrt{h\nu + \alpha}$. This dependence means that by

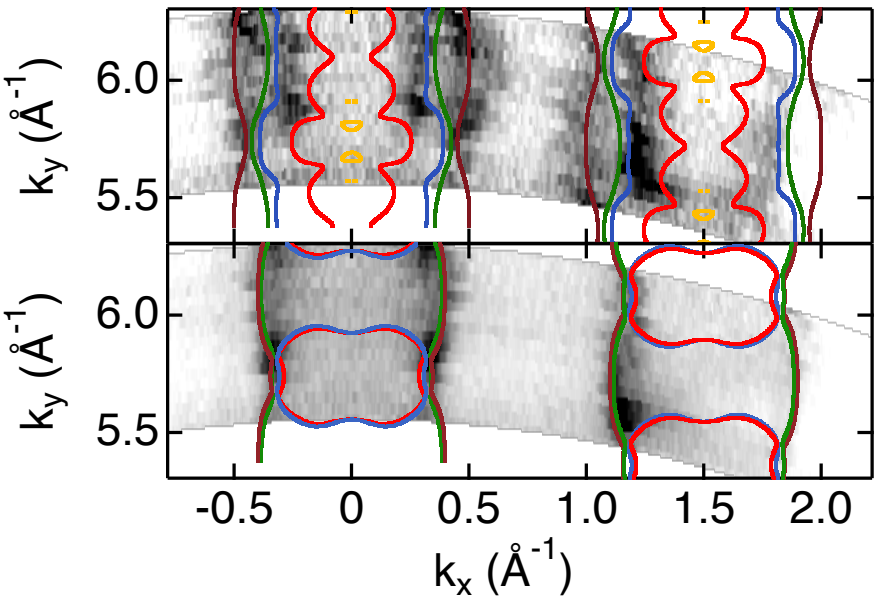

Figure 1.3: Fermi surface reconstruction using photon energy dependence. The top and bottom panels both show constant binding energy maps of $LaNiGa_2$ over a range of photon energies from 110eV to 144eV. The bottom panel shows the $k_z = \pi/c$ plane and the top panels shows a nearby parallel plane to illustrate the variation through the Brillouin zone. Overlaid on both panels in color are the predicted Fermi crossings.

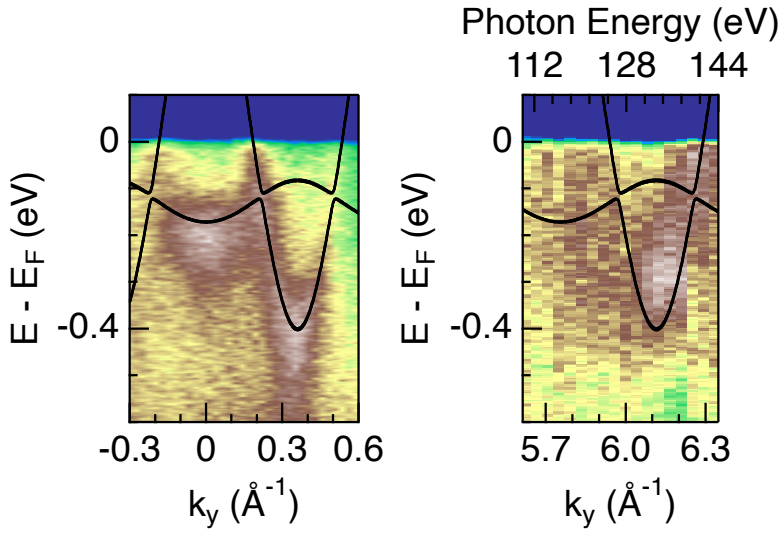

Figure 1.4: $k_\perp$ dispersions compared to direct ARPES. The left panel shows an ARPES spectrum along the $Z - T$ line in $LaNiGa_2$ on a thin-edge cleaved sample. The right panel shows the same area in the Brillouin zone probed through varying the photon energy. The conversion of photon energy to perpendicular momentum was done using equation 1.3 with an inner potential of 15eV in order to find a value that best aligns the spectra with the predictions.

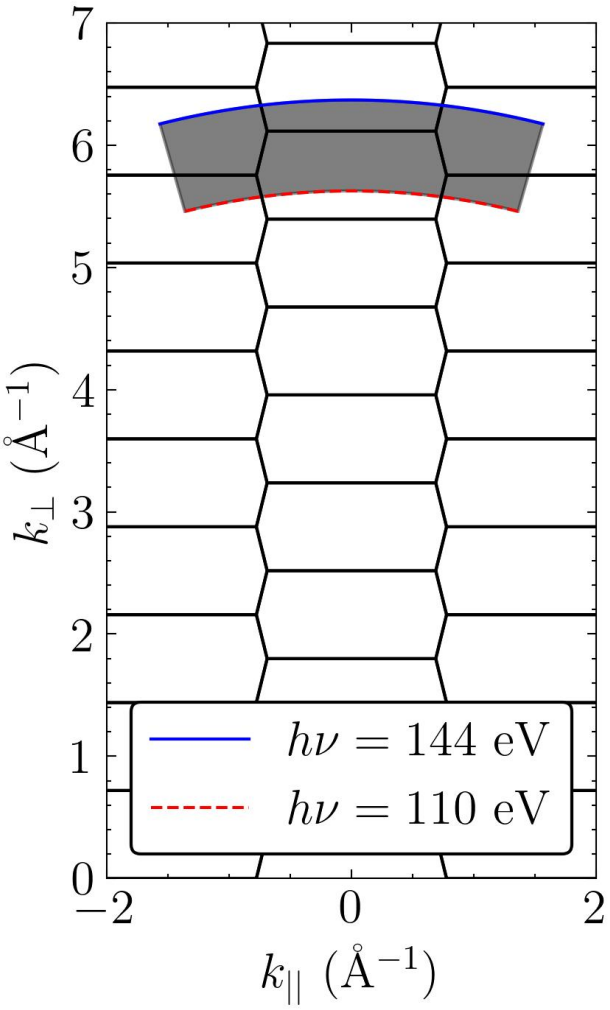

Figure 1.5: The grey shaded region shows the section of momentum space probed by an ARPES experiment with an acceptance angle range of (-15° to 15°) and photon energy range from 110eV (red dashed arc) to 144eV (blue solid arc). The hexagonal shape tiling the figure is the repeated zone scheme for $LaNiGa_2$ where $k_{||} = k_x$ and $k_\perp = k_y$ in order to illustrate the scale of a Brillouin zone to the region probed by ARPES. Geometrically this region is a section of a sphere centered around $\mathbf{k} = 0$ with the radius altered by the addition of an inner potential V_0.

varying photon energy, ARPES can probe the out-of-plane momentum dependence of the electronic structure as well as the more obvious in-plane dependence. A diagram demonstrating the range of momentum space that can be accessed by an ARPES experiment by varying photon energy is shown in Figure 1.5. This method of exploring the three-dimensional electronic structure was used to map $LaNiGa_2$ in the first ARPES measurements of it. Figure 1.6 shows the variation in the electronic structure near the Fermi level of $LaNiGa_2$ from a photon energy of 110eV to 144eV. The range and Brillouin zones depicted in 1.5 correspond to the experimental data shown in Figure 1.6.

The inner potential V_0 is usually determined as a phenomenological fitting parameter to the observed electronic structure and typically in the range of 0eV to 20eV. The inner potential is sometimes described

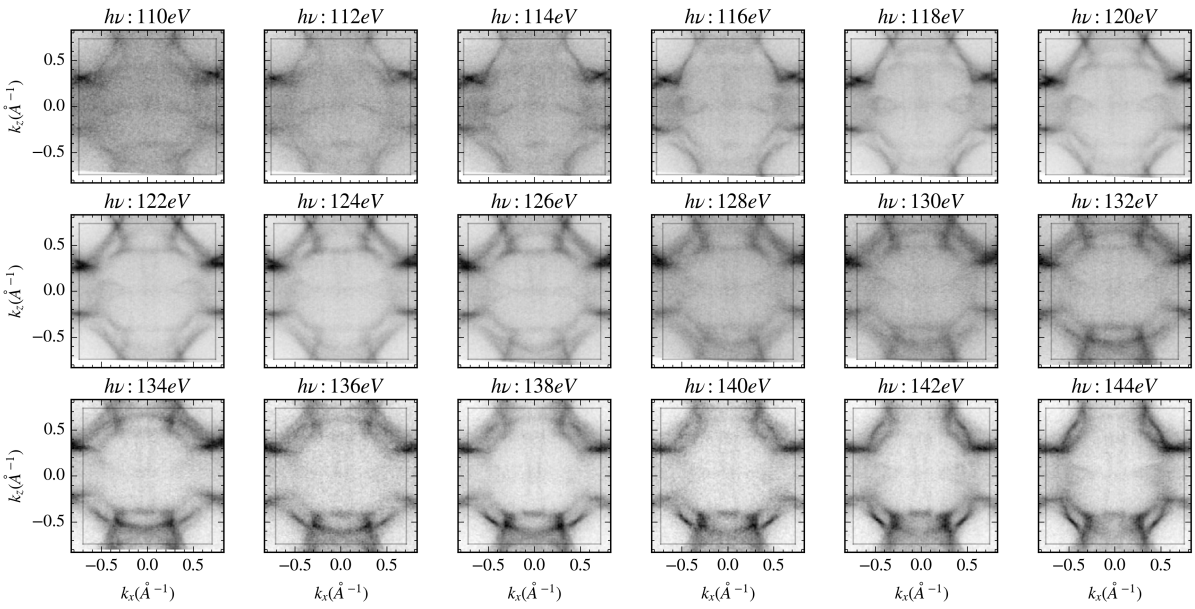

Figure 1.6: Constant energy maps at multiple photon energies of $LaNiGa_2$. Fermi surface maps integrated $50meV$ around the Fermi energy are shown at a range of photon energies from $110eV$ to $144eV$ in steps of $2eV$. Gray box in each panel outlines the Brillouin zone boundary at that photon energy as determined by an inner potential of $15eV$.

physically as being the depth of the valence band beneath the vacuum [4]. Figure 1.3 shows a stacking of the same ARPES measurements from Figure 1.6 instead as a function of perpendicular momentum[6] along two different planes. Overlaid on the ARPES data are the calculated Fermi surface crossings. In addition to the constant binding energy data shown in Figure 1.3 the perpendicular momentum dependent dispersions can be seen by stacking the energy distribution curves at the same k_x, k_z point at each photon energy. The perpendicular momentum dispersion for the the same $LaNiGa_2$ data at $k_z = \pi/c$ and $k_x = 0$ is shown in Figure 1.4. Overlaid on the dispersion in black is the calculated band structure. Utilizing a combination of both the stacked Fermi surface in Figure 1.3 and the perpendicular momentum dispersion in Figure 1.4 we can adjust the inner potential to find the value that best aligns the data with the overlaid calculations. For the examples shown here, the inner potential for photoemission of $LaNiGa_2$ normal to the **b** axis is $V_0 = 15\text{eV}$.

1.3 Photoemission Intensity Formula

Here I will briefly address the interpretation and meaning of the photoemission intensity $I(E, \mathbf{k})$ which can be thought of as:

[6]Be warned, here k_y is listed as the perpendicular direction because the crystal being probed has it's **b** axis normal to the surface. However, frequently the ARPES community will call the out-of-plane direction k_z regardless of the crystal structure being examined.

$$I(E,\mathbf{k}) = I_0(E,\mathbf{k},h\nu,\mathbf{A})f(E)A(E,\mathbf{k}) \otimes R_E(E) \otimes R_{\mathbf{k}}(\mathbf{k}) + B \tag{1.4}$$

In most ARPES experiments, the goal is to measure something about the electronic structure in a material. This electronic structure can be summarized in the single particle spectral function $A(E,\mathbf{k})$ which describes the likelihood for an electron to be at a particular energy and momentum at any time. To be more precise, $A(E,\mathbf{k})$ describes the probability for the whole many body system to have a change in it's energy by amount E when a single electron of momentum $\mathbf{k}$ is removed from the system. It is intuitively clear how the change of the many-body system's energy can be directly linked to the binding energy of the electron. The goal of ARPES can be restated as to measure $A(E,\mathbf{k})$, which contains the intrinsic electronic structure information.

There are a number of aggravating factors which stop ARPES from being able to measure $A(E,\mathbf{k})$ directly. First, the photoemission process can only remove electrons from occupied states, which introduces the Fermi-Dirac distribution term $f(E) = 1/(1+e^{(E-E_F)/k_BT})$. Second, the photoemission process requires the interaction with a photon with energy $h\nu$ and described by the vector potential $\mathbf{A}$. The matrix element governing this interaction can attenuate photoemission intensity if the transition from a particular electron energy and momentum is forbidden. These matrix element effects are encompassed in the $I_0(E,\mathbf{k},h\nu,\mathbf{A})$ term. As with any experiment, ARPES has some finite resolution in detecting energy and momentum which is encompassed in the two convolutions with $R_{\mathbf{E}}(\mathbf{E})$ and $R_{\mathbf{k}}(\mathbf{k})$. The energy resolution can typically be treated as Gaussian and while the momentum resolution can typically be treated as Gaussian as well, it may differ from Gaussian somewhat due to effects like the finite analyzer slit width/shape and broadening in the k_perp direction. Finally, there is a background term B which may originate from the sample (such as in elastically scattered electrons) or it may be from the detector (inhomogeneity in the camera after prolonged use).

Additionally, it should be mentioned that the because of the finite energy budget from the light source and the emission cost of the work function the deepest binding energy that can be accessed is $E_B^{\text{deepest}} = h\nu - \phi$. Further, the largest parallel momentum that can be accessed would be at an emission angle of 90° and the least bound electron such that all of the kinetic energy is utilized by the parallel momentum. The maximum parallel momentum is then given by $k_{||}^{\max} = \sqrt{2m(h\nu-\phi)}/\hbar$. Using a typical work function of $\phi = 4.5$eV, a synchrotron based experiment with photon energy $h\nu = 100$eV would have $k_{||}^{\max} = 5.0\text{Å}^{-1}$ while a 6eV laser system only has $k_{||}^{\max} = 0.63\text{Å}^{-1}$. In most ARPES experiments the analyzer detects an angular range of ±15° which would correspond to $\pm 1.3\text{Å}^{-1}$ and $\pm 0.16\text{Å}^{-1}$ momentum windows for the synchrotron and laser based experiments respectively. These numbers are useful to keep in mind when planning an experiment as it

may restrict what science goals are achievable. For example the 6eV system cannot access the full Brillouin zone for many materials and can only see a small portion of the Brillouin zone for each measurement. Alternatively the higher photon energies and monochromators of synchrotron experiments means that they cannot achieve the same energy or momentum resolutions as a laser based system.

1.3.1 Energy and Momentum Resolution Effects

The experimental resolutions can be found from propagating the uncertainties in the: incident photon energy $h\Delta\nu$, analyzer energy resolution ΔE_a, and analyzer angle resolution $\Delta\theta$. The uncertainty in the measured kinetic energy or the binding energy is the quadrature sum of the incident photon energy uncertainty and analyzer energy resolution:

$$\Delta E_{\text{kin}} = \Delta E_B = \sqrt{(h\Delta\nu)^2 + \Delta E_a^2} \tag{1.5}$$

The analyzer's resolution originates from the finite width of the acceptance slit in the radial direction of the hemispherical analyzer and can be computed using the slit width w, analyzer radius $R_0 = (R_1 + R_2)/2$, and acceptance angle α as:

$$\Delta E_a = E_{\text{pass}} \left(\frac{w_{\text{slit}}}{R_0} + \frac{\alpha^2}{4} \right) \tag{1.6}$$

The resolution in the photon energy $h\Delta\nu$ introduces an important trade off for synchrotron experiments that use a variable exit slit on their monochromator. In this case, widening the exit slit can increase the intensity of the signal dramatically. Unfortunately because the light coming off the diffraction grating is dispersing in space opening the exit slit increases the bandwidth of the X-rays hitting your sample, worsening your energy resolution by making $h\Delta\nu$ larger. The balance of counts, photon bandwidth (through the exit slit), analyzer resolution (through slit width) depends heavily on the science goals of your experiment as these three effects all contribute similar magnitudes of uncertainty in synchrotron ARPES experiments. Additionally, when targeting extremely low energy resolutions (meV) electrical noise of the system can become a problem. To combat this, some endstations try adding extra grounding wires on parts of the system and manipulator. For a more details on the hemispherical analyzer and meaning of the pass energy read Section 1.4.2.

The parallel momentum $\mathbf{k}_{||}$ has uncertainty contributions from the kinetic energy and the analyzer angle resolution:

$$\Delta k_{||} = \sqrt{\left(\frac{\partial k_{||}}{\partial \theta} \right)^2 + \left(\frac{\partial k_{||}}{\partial E_{\text{kin}}} \right)^2}$$

$$\Delta k_{||} = \sqrt{\left(\frac{1}{\hbar}\sqrt{2mE_{\text{kin}}}\cos(\theta)\Delta\theta\right)^2 + \left(\frac{1}{\hbar}\sqrt{\frac{m}{2E_{\text{kin}}}}\sin(\theta)\Delta E_{\text{kin}}\right)^2}$$

While at normal emission ($\theta = 0$) the second term vanishes completely the second term is typically small enough to be completely neglected. For a typical synchrotron experiment with $E_{\text{kin}} = 100\text{eV}$ and $\Delta E_{\text{kin}} = 5\text{meV}$ and $\Delta\theta = 0.1°$ the parallel momentum uncertainty terms are: $\Delta k_{||}(\theta = 0°) = \sqrt{\left(0.00894\text{Å}^{-1}\right)^2 + \left(0\text{Å}^{-1}\right)^2} = 0.00894\text{Å}^{-1}$ and $\Delta k_{||}(\theta = 30°) = \sqrt{\left(0.00774\text{Å}^{-1}\right)^2 + \left(0.00006\text{Å}^{-1}\right)^2} = 0.00774\text{Å}^{-1}$. Using a 6eV laser lab system where $E_{\text{kin}} = 2\text{eV}$ and $\Delta E_{\text{kin}} = 1\text{meV}$ and $\Delta\theta = 0.1°$ the parallel momentum uncertainty terms are instead: $\Delta k_{||}(\theta = 0°) = \sqrt{\left(0.00126\text{Å}^{-1}\right)^2 + \left(0\text{Å}^{-1}\right)} = 0.00126\text{Å}^{-1}$ and $\Delta k_{||}(\theta = 0°) = \sqrt{\left(0.00110\text{Å}^{-1}\right)^2 + \left(0.00009\text{Å}^{-1}\right)} = 0.00110\text{Å}^{-1}$. For an acceptance angle of 30° and a typical number of approximately 1000 angle channels in the detector, each angular pixel is approximately 0.03° which is equivalent to parallel momentum pixel size of 0.02710Å^{-1} for the synchrotron example and 0.00383Å^{-1} for the 6eV laser examples above. Neglecting the second term we can almost always compute the uncertainty in the measured parallel momentum as:

$$\Delta k_{||} = \frac{1}{\hbar}\sqrt{2mE_{\text{kin}}}\cos(\theta)\Delta\theta \tag{1.7}$$

I want to draw particular attention to the $\cos(\theta)$ dependence of the uncertainty in the parallel momentum. That factor means that by rotating our sample further from normal emission we can improve our momentum resolution. Additionally, the $\sqrt{E_{\text{kin}}}$ dependence says that a lower photon energy will give better momentum resolution. There are two an additional contributions to $\Delta k_{||}$ which are hard to quantify but may play a role if claiming very fine features. First, a large spot size can contradict the analyzer's assumptions enough to add additional error in the detected angles (another reason why small spot size synchrotron light sources are important to this field). A large spot size can be especially harmful if the sample surface is curved because the same detected angle corresponds to differing emission angles when measured from the curving surface normal. Secondly, the slit width effectively integrates some number of parallel cuts together, this can be an advantage for bands which do not disperse orthogonally to the slit or it can cause blurring of bands which disperse quickly perpendicular to the slit direction. The momentum information can also be lost if there are too many electrons being emitted such that the electron-electron repulsion while flying to the detector cannot be ignored. This effect, known as space-charging, can occur if the light source is too bright or if the photon energy is so low that the electrons spend more time propagating near each other. For laser based ARPES both of those effects are in play so extra care must be taken to ensure the light source is not too bright to cause space-charging.

It may seem that the best way to understand the uncertainty in the perpendicular momentum would be to propagate the uncertainties in the same way we did for the energy and parallel momentum above. However, the exponential surface sensitivity (discussed further in Section 1.3.5) of the photoemission process enforces a quantum mechanical uncertainty from the inelastic mean free path [9]. The values of this uncertainty typically range from 0.3Å^{-1} to 0.05Å^{-1} depending on the inelastic mean free path (3Å^{-1} and 20Å^{-1} respectively for those examples) and can be found by:

$$\Delta k_{\perp} = 1/\lambda_{\text{IMFP}} \tag{1.8}$$

I would also like to address the contribution of the photon's momentum to the emitted electron. The incident photon carries a momentum $p = E/c = h\nu/c$ which is $k = 0.05\text{Å}^{-1}$ for a photon with energy $E = 100\text{eV}$. In the three-step model we model the absorption of the photon as an optical ($\Delta k = 0$) transition which means. The size of a Brillouin zone is around 1.5Å^{-1} and therefore the photon momentum shift is around 7%. For hard X-ray ARPES with photon energies in the keV range, this effect cannot be neglected.

1.3.2 Geometry of ARPES Data in Momentum Space

When comparing ARPES data to computed electronic structures it is very common to approximate that a single ARPES E vs. k image corresponds to a line in momentum space or that a intensity map at a constant energy[7] occupies a plane of constant perpendicular momentum. These approximations improve for larger and larger photon energies thanks to the manifold that ARPES maps becoming larger at larger photon energies when compared to a single Brillouin zone.

If we take the naive approach and consider the inner potential term irrelevant ($V_0 = 0$), then the true geometry of a single ARPES spectrum takes place along an arc of a great circle with radius $|\mathbf{k}|$. Similarly, a constant energy map as a function of the two in-plane momenta would be observing a section of the same sphere bounded by four great circles. In fact, the inner potential alters the observation such that an electron we observe having momentum $\hbar|\mathbf{k}| = \sqrt{2mE_{\text{kin}}}$ must have had a slightly higher momentum $\hbar|\mathbf{k}| = \sqrt{2m(E_{\text{kin}} + V_0)}$ while inside the crystal. The addition of the term with V_0 under the square root implies that the geometry we probe with ARPES is still a sphere in the momentum space of the crystal however, the radius of that sphere is slightly larger than we may initially expect from the observed kinetic energy.

Figure 1.5 shows the section of momentum space probed by ARPES on a crystal whose inner potential is 15eV with a common detector range of $-15°$ to $15°$ and photon energy varying from 110eV to 144eV in gray.

[7] Colloquially (not in literature), it is common in the ARPES community to refer to a constant energy map as a "Fermi surface map" even when looking at energies that do not correspond to the Fermi level.

The repeated zone scheme of the Brillouin zone of $LaNiGa_2$ is displayed[8] in black in order to demonstrate the scale of a Brillouin zone with the range probed by a typical ARPES experiment. From Figure 1.5 it is clear that near normal emission an approximation of a single value for $k_\perp$ is reasonable. However, it should be kept in mind for experiments probing further Brillouin zones by having an offset rotation in the crystal that ARPES measures a spherical surface in momentum space not a plane.

1.3.3 Spatially resolved ARPES

Spatially resolved ARPES measurements, performed with a tightly focused photon source, provide detailed insights into the local electronic structure of a material. These spatially resolved experiments with micro- (μARPES) and nano- (nARPES) focused light sources have enhanced the application of ARPES to access:

1. Exfoliated two-dimensional materials and heterostructures. These materials and heterostructures composed of them frequently only span a space of tens of micrometers. Prior to μ/nARPES these samples were too small to access and could not have their electronic structure directly probed. Small spot sizes also allow for ARPES on heterostructures and monolayers of two dimensional materials. These heterostructures have become a large research field due to the novel behaviors originating from the moiré potential and hybridization between layers.

2. Rough samples. These materials do not easily cleave such that they have macroscopically homogeneous surfaces that can be probed with a large beam spot. This roughness can happen when there is not a possible neutral cleavage plane in the crystal structure or if there is strong 3D bonding.

3. Heterogeneous terminations. Some materials (such as $Co_3Sn_2S_2$) have multiple bonds that are likely to break when exposing a fresh surface. With μ/nARPES the electronic structure differences in these multiple terminations can be investigated.

4. Platelet edges and needle shaped samples. Many materials grow in a platelet style where they are large(tens of mm to cm) along two axes but thin (approximately 1mm) along the third dimension. Additionally some one dimensional materials can only be grown long along a single axis but are thin in their other two. These materials cannot yet be grown to a macroscopic size along the axis of interest which prohibits traditional ARPES experiments on them. Using a micro-focused beam we can target thin one-dimensional materials or the thin axis of a platelet style sample. Probing these materials along these thin dimensions is important because they can have important electronic structure information

[8] In Figure 1.5 the $k_{||}$ and $k_\perp$ axes correspond to the k_x and k_y axes of $LaNiGa_2$ respectively.

along those dimensions. Utilizing photon energy to scan the perpendicular momentum is insufficient for these important structures due to it's lower resolution.

In the later parts of this thesis I will utilize the advantaged provided by spatially resolved ARPES to: (1) Target the thin-edge of a $LaNiGa_2$ to access spectra directly that are otherwise impossible to observe without trying to access the $k_\perp$ dependence through varying photon energy. (2) Use machine learning to search for the spot on a sample that assesses the target science goals of a user. (3) Analyze the spatially dependent ARPES and XPS spectra of a two dimensional heterostructure of graphene using nARPES. (3) Understand the correlation between the spatial heterogeneity of the ARPES and XPS in $Co_3Sn_2S_2$.

1.3.4 X-ray Photoemission Spectroscopy (XPS)

X-ray photoelectron spectroscopy (XPS) is a photoemission experiment that targets the tightly bound core electrons as opposed to the valence band investigated with ARPES. Core electrons are heavily localized around their host ions and therefore are delocalized in momentum space. Due to this momentum delocalization XPS spectra are angle-integrated which often allows for acceptable signal to noise with a shorter measurement than an ARPES measurement. The interaction of the deeply bound core electrons with the bonding electrons allows XPS spectra of the core electrons measure the local chemistry of the atom being probed. XPS can often be performed using the same spectrometer and light source as ARPES allowing researchers to switch between the modes to collect data about the tightly bound as well as the valence electronic structure. Being a photemision experiment, XPS can be surface sensitive if performed with UV light[9] or low energy X-rays. Exploiting the surface sensitivity, researchers sometimes search for desired XPS features to locate a good spot to perform ARPES because XPS can be faster to collect.

1.3.5 Surface Sensitivity

Photoemission is a surface sensitive process due to the need for photoelectrons to propagate from their original position in the material to the surface without scattering to preserve their momenta. The inelastic mean free path (IMFP) is in general challenging to compute for any given material. However, most materials have their IMFP following a "universal curve" as a function of the electron's kinetic energy [8]. While there is a lot of materials dependence, large scale studies have found a universal behavior of the IMFP for electron energies of 50eV and above [10]. The universal curve for these higher electron kinetic energies encapsulates the tendency for faster electrons to interact less with the material and, thus, make it out of

[9]While the X in XPS stands for X-ray, the experiment is still fundamentally a photoemission experiment. That means that XPS can be performed with any light source that is capable of exciting the core levels of interest including UV and soft X-rays under the same binding energy constraints as ARPES.

material to the analyzer. At lower photon energies fewer such studies have been performed, but they show non-universality [11, 12]. The IMFP at these lower kinetic energies is found to depend on exact mechanisms of scattering which are often materials dependent. Often depth sensitivity can increase at lower photon energies due to the prevalence of elastic scattering channels, which can compete with inelastic scattering [11]. For ARPES experiments described in this dissertation the kinetic energies of the valence electrons are typically in the range of $10-150$eV where the minimum of the universal curve is. Very low or high photon energies such as a 6eV laser or soft/hard X-ray source can probe more bulk sensitive states than the more common UV ARPES light sources if the scientific goal requires bulk penetration. The surface sensitivity of photoemission experiments necessitates a careful experimental procedure to ensure an atomically clean surface can be found and persist long enough for the experiment, this is discussed further in 1.4.1.

The surface sensitivity of photoemission experiments is also used as an advantage in many research projects. It was the surface sensitivity of ARPES measurements of the predicted surface states that confirmed the topological materials Bi_2Se_3, Bi_2Te_3, and Sb_2Te_3 among others [13, 14, 15, 16, 17, 18, 19]. Topological quantum materials frequently have characteristic surface and bulk electronic structure contributions which are identified by ARPES due to the technique's ability to sense surface states while coincidentally measuring the bulk electronic structure. The attenuation of electrons propagating through the bulk has also been used in angle-resolved XPS to understand the cleavage plane of $HgBa_2CuO_{4+\delta}$ [20].

1.4 Anatomy of an ARPES Experiment

In this section I will discuss all of the aspects of an ARPES experiment that I could enumerate. This will serve as a basis for understanding the method by which almost all of the data in the remaining chapters was collected.

1.4.1 Sample Mounting and Ultra-High Vacuum Preparation

The extreme surface sensitivity of ARPES requires careful preparation of the sample surfaces prior to the experiment. This surface preparation happens in one of three ways:

1. Top-post cleaving, which involves epoxying on a small ceramic post to the top of the sample that can be hit with a stick inside the chamber to gain leverage and expose a new surface. This method was by far the most common as it is technically easy and can at least be attempted for almost any type of crystalline specimen. A modification of this is to directly cleave the crystal without using a top-post. This direct-cleave method was used in my study on $LaNiGa_2$ as probing the thin-edge of the platelet

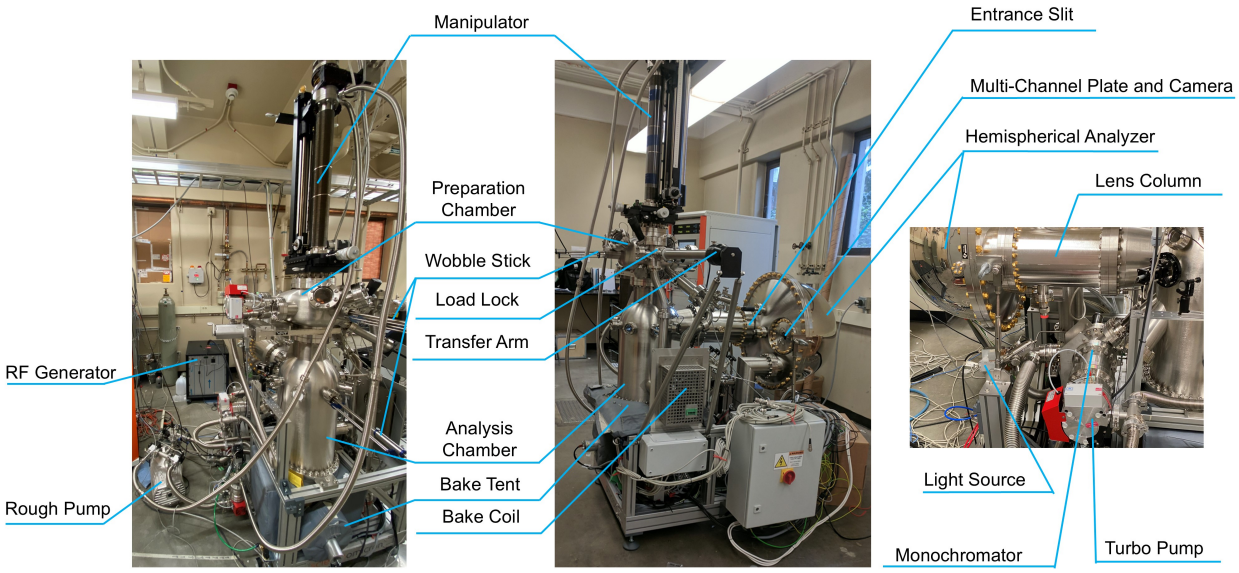

Figure 1.7: Anatomical listing of many of the key parts of an ARPES system illustrating how they fit together.

did not require the leverage of a top-post [2].

2. Exfoliating by sticking a piece of clean tape onto the top of the sample which can be torn off to expose a new surface. Due extremely weak bond between the tape and the sample when compared to epoxying a top-post on, this can only be done when the sample has a crystal structure that allows it. Exfoliation was only used in cases of Van der Waals bonded materials which have extremely weak inter-layer bonds such as transition metal dichalcogenides. The choice of tape must also be done with care because some tapes leave residue behind that can off-gas when placed in the ultra high vacuum chamber for the experiment. Exfoliation is typically only compatible with ARPES experiments if there is a glovebox attached to the chamber - as is the case at the Maestro beamline 7.0.2 at the Advanced Light Source.

3. Thin film growth. Some ARPES systems have the ability to perform thin film growth connected to the same vacuum system as the ARPES chamber. This thin film growth allows for samples to be grown and measured without ever leaving the UHV [21, 22, 23]. With growth it is possible to measure materials which would degrade if ever exposed ambient pressure or the contaminants in air.

4. Sputtering and Annealing. Sputtering is the destructive process of bombarding the material with an ion gun, removing a layers of the material similar to an atomic level sand blaster. Sputtering can be used to remove a capping layer on a material for samples which cannot have a top-post mounted

on them because they are too thin, too strongly bonded, degrade quickly in air, or otherwise. After sputtering, samples can be annealed in the vacuum chamber by raising the temperature so that the sample surface can reform and heal the craters left by sputtering. Annealing can also be used without sputtering for the same reasons.

In order to preserve the ultra-clean environment of the ARPES chamber all tools which may be exposed to the ultra-high vacuum should be cleaned prior to entering into the chamber. The cleaning process involved placing all items (tweezers, top-posts, sample holders, ...) into a sonicator bath of acetone and then a sonicator bath of isopropyl alcohol prior to sample preparation. Once all items that could be cleaned were ready the samples could be mounted.

Mounting

There are many different types of sample holders, with synchrotron beamlines typically making custom implementations for their end stations. Because photoemission is a process that ejects electrons from a material we must make a connection from our sample to an electrical ground otherwise the sample will begin accumulating a charge. When the sample charges the electrons must escape an additional electrostatic potential well in order to reach the detector. This additional potential causes the spectra to look like they are sliding 'down' to deeper binding energies. Once a sufficient charge has accumulated the sample will arc to the closest electrical ground. Depending on the light sources, sample composition, and quality of the grounding this charging process can be extremely fast such that the spectra are completely ruined or slow enough to be observed while looking at the spectra monitor.

While the exact sample holders may be different, the mounting process is typically the same:

1. Mixing a strong epoxy. Most of my samples were mounted using Epo-tek H21D which is a conductive epoxy. Some samples were mounted with a stronger but insulating epoxy such as Torr Seal. When an insulating epoxy is used we must take care to ensure a proper ground by using a silver paint or dot of conductive epoxy somewhere on the sample.

2. Toothpick sharpening. I use a razor to sharpen the tip of a toothpick to a point so that a very small amount of epoxy can be taken and placed onto the sample holder. If too much epoxy is placed on the sample holder then when the sample is put on top it can ooze around and hug the side of the sample. Epoxy around the side of the sample can ruin the ability to take spectra for a few reasons: (1) Blocking the light source by interrupting the path of the beam before it can reach the sample surface (2) Blocking emitted electrons on their way to the electron analyzer - depending on the exact orientation this can be seen on the detector as an unexpected sharp drop in intensity at a certain angle,

(3) Causing mirror charges in the conductive epoxy or paint. This can appear in the same way as (2) or it can cause a blur in the spectra in other orientations because the electrons are experiencing an additional angle dependent force for different amounts of time depending on their kinetic energies.

3. Placement of the sample on the epoxy. This is done under a microscope and the sample should be pressed carefully down using the clean tweezers so that good contact is made between the sample and the epoxy. If while pressing epoxy is seen wrapping around the size of the sample we must remove the sample and clean excess epoxy off of the sample and holder.

4. Mounting the top-post on the sample if one is being used. Either by dipping the top post into the epoxy on the table or using the toothpick to place a dot of epoxy onto the sample and then placing the top post onto the sample. If the epoxy wraps around the side of the sample after placing the top post the sample is much more likely to fall off completely instead of cleaving as desired.

5. Curing the epoxy. This step depends on the exact epoxy being used and should be done according to their directions. Typical curing for my samples was 20-30min at 120° C.

6. Verifying sample grounding. There are two methods I used to verify this: (1) The safer indirect way is to cure a small spot of epoxy on a piece of foil at the same time as the sample and then measure that there is a good electrical connection from the top of the epoxy through to the foil. (2) The direct way is to use sharp tips on a multimeter and a microscope it is possible to measure the conductivity from the top of the sample through to the sample plate.

1.4.2 The ARPES Chamber

Vacuum Tight Chamber

The mean free path of an electron in air is $0.68\mu m$ [24] which is far less than the $\approx 1.5m$ needed for the electron to traverse the electron optics and analyzer in a typical ARPES system. In addition, a fresh sample surface would be immediately dirtied by contaminants in the air. For these reasons we need not a water- or air-tight chamber but a vacuum-tight chamber to keep as tight of a vacuum as possible in the chamber. A typical operating pressure for ARPES chambers is $< 10^{-10}$mbar[10] so that a fresh surface can remain fresh after being exposed.

Obtaining a chamber pressure of $< 10^{-10}$mbar requires a series of pumps, a procedure called a bake, and atomically tight gaskets connecting different sections of the system. The mechanism to form an atomically

[10]Using Boyle's law $P_1V_1 = P_2V_2$ with an approximate chamber volume of $1m^3$ the entire chamber contains approximately the same amount of gas as a sphere of air with radius $30\mu m$ which is less than having a diameter of a human hair ($100\mu m$).

tight seal between sections without welding is a having a knife-edge on each side that is pressed into a fresh gasket of copper when tightened with joining bolts. The groove that is pressed into the copper is unique to the exact knife edge on each side and even the orientation of the ring allowing for a tight seal even if the knife edge is not perfectly uniform. Because of the unique groove, the copper gaskets must be discarded after each use and must be discarded if they have a scratch in their surface that would cross the knife edge[11]. The important parts of obtaining and keeping a chamber pressure so low are described in the next few sections.

Rough Pump

Roughing pumps are used as the first stage and pump the chamber down to 10^{-2}mbar. Typically, scroll pumps are used because they are "dry" and do not risk contaminating the vacuum system with pump oil. Scroll pumps use an oscillation of two intersecting spirals (scrolls) to capture pockets of gas from the inlet and push them through the inlet on the exterior of the scroll and push them through the center of the scroll. Scroll pumps alone can not reach a pressure low enough for our system to operate so we must use turbo-molecular pumps as described next.

Turbo Pump

A turbo-molecular (or turbo) pump can bring the pressure of a chamber down from the rough pump pressure to around 10^{-10}mbar for a clean system and 10^{-9}mbar for a dirty system. Turbo pumps use a series of extremely fast rotating blades ($> 60,000$rpm) stacked by stationary blades. When a gas molecule enters the opening of the turbo pump the blades hit it and add momentum in the pumping direction. The molecule then bounces off of a stationary blade - again being directed outward - and the process repeats with steeper and steeper angled blades until the molecule is pushed out the back of the pump. Relying on the fast rotating blades and kinematics of individual gas molecules rather than fluid dynamical properties of a more dense gas, turbo pumps rely on having a low pressure on both their input and output. The output port of the turbo pumps are plumbed to the input of the rough pump which then evacuates the gas to the room.

Ion an Sublimation Pumps

In addition to the mechanical pumping from the turbo pumps, many UHV systems use ion pumps or titanium sublimation pumps. Ion pumps function by ionizing the molecules that pass into them and the ions are then attracted to the pump using a high voltage. Titanium sublimation pumps (TSPs) function by sublimating a thin film of titanium and depositing it on walls of the chamber. Titanium is very reactive and therefore

[11] When installing a copper gasket with a large diameter it can be useful to bounce it on-edge on a desk or the ground and then clean it before installation. This bounce slightly deforms the ring so that it can hold itself in the pipe while aligning the other end of the flange.

when a gas molecule hits the walls coated with it there is a chance that the molecule will bond to the wall. Both ion pumps and TSPs do not actually evacuate the gas from inside the chamber to the outside air and instead work by bonding stray gas molecules to the chamber walls.

Bake Tent and Coils

While the stainless steel interior of a UHV chamber may seem completely dry before the pumps start evacuating there is in fact a layer of water (and a few other trace gasses) that has adsorbed onto the walls of the chamber. The steel walls of the chamber also absorb significant hydrogen which will lead the dominant chamber pressure to be caused by H_2. In ambient conditions this process reaches an equilibrium where the water is probabilistically desorbed by the thermal energy in the steel and at the same rate more water is adsorbed. When the system is evacuated using the rough and turbo pumps it reaches a pressure floor that is caused by the water being adsorbed from the walls of the system. This off-gassing pressure will slowly (very slowly) decrease over time as the gaseous water eventually runs into the blades of a turbo pump and get evacuated. Because the mechanism for desorption is almost entirely thermal the process can be sped up by heating the walls of the chamber. To perform a 'bake-out' the system is wrapped with heater tape entirely enclosed in a thick thermally insulated blanket[12]. A series of coils much like the ones on an electric stove are turned on and a fan blows blows hot air around the system inside the blanket. This bake-out will raise the pressure from 10^{-9}mbar to a much higher level 10^{-6}mbar due to the additional off-gassing from being at $> 100°$C. After the system has been heated and pumped on for a few days it is let to cool where the pressure will drop below the previous level and reach its base pressure around $10^{-10} - 10^{-11}$mbar. ARPES systems are baked at a lower temperature (120° C) than other UHV systems because there are some components that cannot withstand high temperatures. In particular, the multi-channel plate detector cannot be overheated for risk of ruin. We attempt to alleviate this problem by performing the bake for a much longer time (a week or longer) than other UHV systems.

Load Lock

Once an ultra-high vacuum has been reached we want to do everything possible to maintain it and avoid adding any off-gassing materials inside. To load a sample into the chamber we use a small section as a load lock where we can vent to air pressure and then pump down quickly. Some systems implement a bake-out on just the load lock after every opening which keeps the interior vacuum as clean as possible. In the case of our lab system at Davis, we vent with Nitrogen gas and try to keep a small positive pressure of nitrogen in the

[12]During this time any expandable components such as the bellows of the manipulator should be expanded to their maximum size to increase surface area and probability that desorbed gas will scatter to a turbo pump as much as possible.

load lock while moving sample in to avoid water from the air entering the load lock. Once the samples are in the load lock it can reach near the base pressure of the system once again. Sometimes we perform a bake on the load lock after transferring samples to keep the UHV as pure as possible. The step of transferring a sample from the load lock into the main chambers should be done quickly so to avoid having gas flow from the load lock into the main chambers. The load lock or adjacent chambers also frequently operate as a garage where many samples can be stored at once. Having many sample inside at one time allows us to change samples many times without having to vent the system.

Transfer Arm

To move the samples around while inside the UHV chamber we use magnetically coupled transfer arms. These arms have a set of very strong magnets on a cuff on the outside that couple to a set of magnets on a rod in the UHV system. This allows the samples to be moved while inside the chamber without any worry of mechanical deterioration of a gasket or bellows.

Preparation Chamber

The preparation chamber is a section that is usually adjacent to the chamber where the ARPES will be performed. In this chamber there are usually a set of tools that can be used to prepare a sample for the experiment. Examples of preparation tools are ion sputtering guns, material evaporators, wobble sticks. The preparation chamber is in principle optional, but provides an opportunity to close off the analysis chamber from any dirtier processes that may need to happen before the experiment is performed.

Analysis Chamber

The analysis chamber is typically the largest chamber in the system and is where the entrance cone to the electron analyzer is. This chamber is also the most clean and where we try to keep any gasses away from as much as possible. In the analysis chamber the sample is mounted on the manipulator which provides the most maneuverability of the sample during the experiment.

Manipulator

Manipulators (also sometimes called a goniometer) follow their namesake by allowing many axes of manipulation for the sample while it is inside the UHV chamber. Typical manipulators have 5 or 6 axes of manipulation (X, Y, Z, Polar, Azimuthal, and sometimes 'Tilt'). The manipulator angles can be measured along with the angles measured in the electron optics to allow us to find the angle of emission from the

sample normal[13] In addition to manipulation, the manipulator usually contains a cold finger (a good heat conductor) behind the sample location to allow a coolant like liquid nitrogen or liquid helium to cool the sample while in the UHV. There are also frequently small heaters on the sample holder to allow for temperatures higher than the coolant temperature. While there are temperature sensors right next to the sample or on the cold finger the sample will always be some amount warmer than the temperature reading because the analysis chamber walls are at room temperature and radiate heat onto the sample.

Wobble Stick

A wobble stick is much like a transfer arm however it can also be pivoted around the point where it couples with the system. The wobble stick is used to break cleave the sample by breaking the top post off of the sample in the UHV system. Our Davis lab system also uses a wobble stick with a special tip to transfer the sample from the transfer arm onto the manipulator. Other wobble sticks have a screwdriver like head that can be used to adjust complex sample holders such as strain devices while on the manipulator.

Light Source

The light source of a photoemission experiment is critical to the photoemission portion of the experiment. The three most common light sources are:

1. Synchrotron light source. These are large user facilities which produce a broad spectrum of X-rays such that the user can choose their desired photon energy with a diffraction grating and are the most versatile type of light source. This variable photon energy allows for the exploration of different perpendicular momenta as described in Section 1.2.3. The bright and variable light coming from synchrotron light sources enable many otherwise impossible ARPES experiments including nano-ARPES, on-resonance ARPES, and tuning to access favorable matrix elements.

2. Gas discharge lamps are compact X-ray sources that can be used to perform ARPES in a university lab setting. Our lab system at UC Davis uses a He discharge lamp where a cavity is filled with low pressure He and a high intensity RF generator ionizes the gas. The primary intensity of the He discharge lamp is the He I line which is the $2p \rightarrow 1s$ transition of neutral He at 21.2eV. This 21.2eV line is the most common for lab based ARPES measurements. There is also a $\approx 10\times$ weaker discharge from singly ionized He atoms where the remaining electron makes a $2p \rightarrow 1s$ which produces 40.8eV. This secondary line can allow for some exploration of XPS and photon energy dependence of spectra. These

[13]It should be mentioned again, many times, that when the sample is mounted onto the sample holder the sample normal will not be perfectly level with the normal of the sample holder because the epoxy underneath it. This means that we must experimentally find the sample normal for every new sample.

lines can be separated with the inclusion of a monochromator or without a monochromator for a lower cost experimental setup.

3. Lasers are another light source used for lab based ARPES experiments. Lasers generally provide very low photon energies (6eV - 11eV) which allows for extreme momentum and energy resolutions (see Section 1.2.2. Our lab system at Davis uses a double second harmonic generation setup to provide a 6eV light source for our ARPES system[14].

Electronic Lens Column

The electron lens uses electric fields to image the electrons emitted from the sample onto the analyzer. There are two primary modes of operation for the electron lens. First, transmission mode images the photoelectrons directly in real space such that they are spatially distributed on the analyzer as they were when they came from the sample. Transmission mode functionally operates similar to a standard optical lens. Second is angular mode which distributes the electrons according to their angle of emission from the sample. Angular mode works similarly to imaging a Fourier plane in traditional optics.

The other job of the electron lens is to scale the kinetic energy of the electrons from their initial values to a range that is expected by the energy analyzer. The energy the analyzer is expecting is referred to as the "pass energy" and will be described more in the hemispherical analyzer Section 1.4.2. In almost all cases the electrons must be slowed down to enter the analyzer but it is also possible for the fields to reverse in strength slightly to accelerate electrons to the pass energy.

Analyzer Entrance Slit

The electron lens images the desired information about the emitted electrons onto an entrance slit at the analyzer. This entrance slit can either be straight or have the same curvature as the hemispherical analyzer it is attached to. When performing the experiment we typically have many options for the size of slit to use. The thin direction of the slit will be used to measure the kinetic energy of the electrons later. Therefore, a larger slit will cause lower energy resolution as it allows electrons to start at slightly different positions along the radius of the hemisphere. Using a straight slit will lead to variation in the measured kinetic energy along the angle axis where a curved slit is curved to keep the same kinetic energy along the same row of pixels on the camera. Instead, a curved slit breaks the assumptions of the angle detection by not mapping a straight line in angle space. A depiction of the pros and cons of both a straight curved slit is given in Figure 1.8. Each style of slit prefers the assumptions of a different portion of the analyzer where electron lens wants a

[14]In my first year at Davis I set up a 6eV laser light source for our ARPES system with the help of Adam Gross.

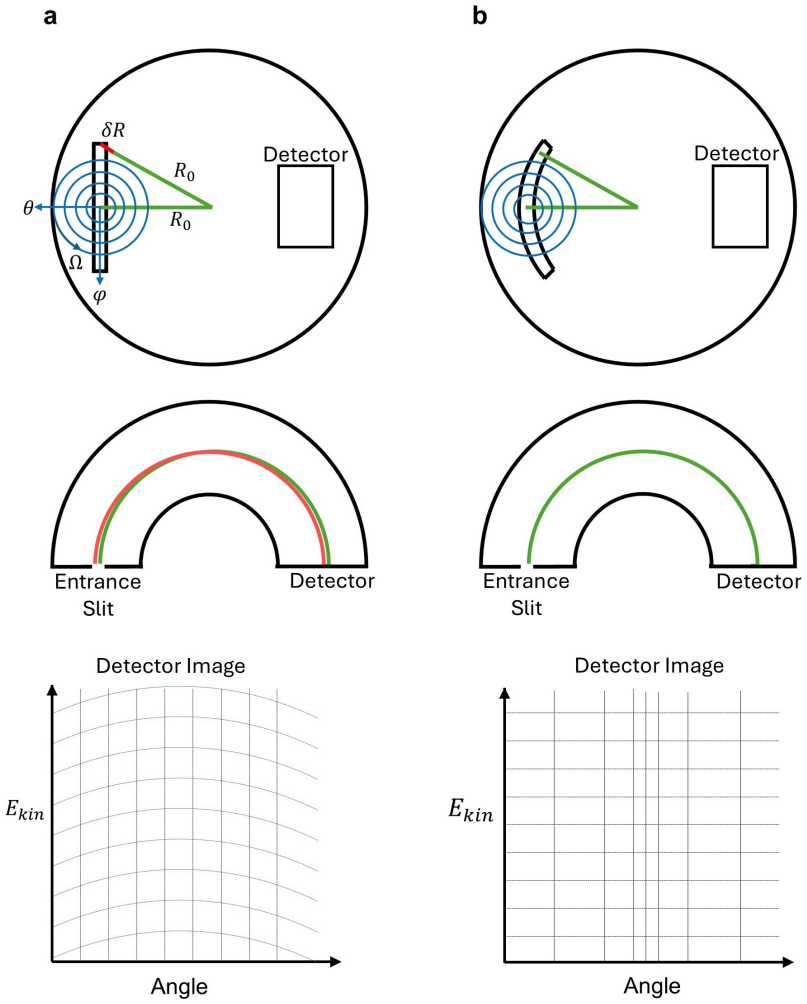

Figure 1.8: Illustration of straight vs curved slits for hemispherical analyzers. (a) The top panel shows that a straight slit images electrons along a constant azimuthal (Ω) angle of detection. The straight slit is not a constant distance from the hemispherical analyzer center which causes electrons of the same kinetic energy to be imaged at slightly different radii on the detector. This slit-dependent kinetic energy shift can be corrected during analysis by correcting the Fermi level to be the same kinetic energy across the data. The angle naming convention shown is that used in the Vishik lab. It should be noted that the relevant angles for the physics of ARPES are the emission angles measured from the surface normal which may be arbitrarily rotated compared to the analyzer. (b) A slit curved with the same curvature as the hemisphere correctly maps electrons of the same kinetic energy to the same radius on the detector. However, a curved slit does not image constant detected azimuthal angles. The bottom panel shows lines of constant kinetic energy and angle of emission (as imaged by the electron lens, which may differ from the sample). For a straight slit, the angles are regularly spaced while the kinetic energies follow a circular arc with the radius of the analyzer. The curved slit however has lines of constant kinetic energy regularly spaced while the angles are not linearly spaced.

straight slit, hemispherical analyzer wants a curved slit.

Hemispherical Electron Analyzer

The hemispherical analyzer is uses two concentric hemispheres of different electrical potentials to create a radial electric field. As in the common electricity and magnetism homework question given to students,

electrons will have a different radius of curvature of their path in a radial electric field depending on their kinetic energy. This fact is used to map the electrons who originate from the slit to a detector where one axis is mapped using the electron lens column and the other is mapped using the kinetic energy.

The kinetic energy which allows the electrons to propagate through the hemisphere without changing their radius is known as the pass energy. The pass energy is dependent on the potential energy difference between and the radii of the inner and outer hemispheres as [4]:

$$E_{\text{pass}} = e\Delta V \left(\frac{R_1}{R_2} - \frac{R_2}{R_1} \right) \tag{1.9}$$

A useful mental image for the effect of the pass energy on the detected spectra is as "zoom-out" factor. In this way, a larger pass energy will image a larger range of binding energies onto the fixed detector than a smaller pass energy. It is clear then that using a smaller pass energy one can achieve a better experimental resolution as the kinetic energy of the electrons is better distinguished.

Multi-Channel Plate

To boost the signal, a multi-channel plate (MCP) is placed on the imaging plane of the hemispherical analyzer. The MCP effectively operates as a grid of micro fabricated electron multipliers using electron avalanches. Depending on the voltage applied to the plate this can boost the signal of the incident electrons at the cost of some increased noise. To have the highest accuracy in data, the lowest MCP voltage that gives a signal should be used. In practice, one can often slightly (+-100V) increase or decrease the MCP voltage to alter the brightness of the image. Care should be taken when increasing the MCP voltage (only in small steps such as 10V) as if it becomes too large it can burn out pixels in the camera or contribute to nonlinearity in the intensity sensitivity of the camera.

Camera

Finally a camera images the electrons via a phosphor screen where the data can be recorded to a computer. Depending on the age and how it has been treated the camera can gain significant nonlinearity which should be regularly calibrated in order to provide quantitative statements about absolute intensities of features.

1.5 Beamline Endstations

The importance of synchrotron based photoemission experiments to this dissertation is hard to overstate. While I have worked frequently with the lab based ARPES system we have on campus for our group, all of

the data used in this dissertation came from a synchrotron endstation. The two facilities I used were the Advanced Light Source (ALS) at the Lawrence Berkeley National Laboratory and the Stanford Synchrotron Radiation Lightsource (SSRL). At SSRL, all of my experiments were performed at beamline 5-2 where I collected the data for the $LaNiGa_2$ project. At the ALS I was able to perform ARPES at beamlines 4.0.3 ("Merlin" High energy resolution ARPES), 10.0.1 (Spin-resolved ARPES), and 7.0.2 ("Maestro" micro- and nano- ARPES). In addition, I was able to join the Maestro group working with Eli Rotenberg to develop and implement the autonomous real-time machine learning control system for the micro-ARPES endstation for one year during the end of my PhD under a doctoral fellowship. The photon energy variability and micro-focused spot sizes that are only possible at synchrotron endstations are the only reason I was able to pursue the research interests that made this dissertation possible.

Chapter 2

Quantum Materials

2.1 Introduction to Quantum Materials

Quantum materials encompass a diverse class of systems with electronic properties arising from quantum mechanical effects, such as strong correlations, nontrivial topology, or reduced dimensionality. Examples include superconductors, topological insulators, and semimetals. Research in these materials has been increasingly popular due to their potential to realize novel physics and enable new technologies in electronics, spintronics, and quantum computing. This dissertation discusses several quantum materials in upcoming chapters, with multiple points of interest, but a common ingredient light-like dispersions, the relevance of which is described below. More detailed treatments of the theory and measurements of quantum materials have been done in other works [25, 26, 27, 28, 29, 30], here I will focus my discussion on materials directly relevant to the later chapters.

2.2 Light-Like Dispersions in Quantum Materials

Light-like dispersions are defined by a linear band structure ($E = \hbar v k$). These linear dispersions are analogues to the massless Dirac fermions studied in particle physics[1], enabling the realization of relativistic quasiparticles in condensed matter systems, such as Dirac and Weyl fermions. Materials with these dispersions, including graphene, topological insulators (TIs), and Dirac or Weyl semimetals, offer platforms to explore fundamental quantum phenomena, including the chiral anomaly, Fermi arcs, and spin-momentum locking. In addition to their interest for studying fundamental physics, these materials exhibit unique electronic,

[1]The common formula cited for effective mass $m^* = \hbar^2/(\partial^2 E/\partial k^2)$ only applies to parabolic bands. For non-parabolic bands a more general form, sometimes called the optical effective mass, must be applied [31, 32]: $m^* = \hbar^2 k/(\partial E/\partial k)$.

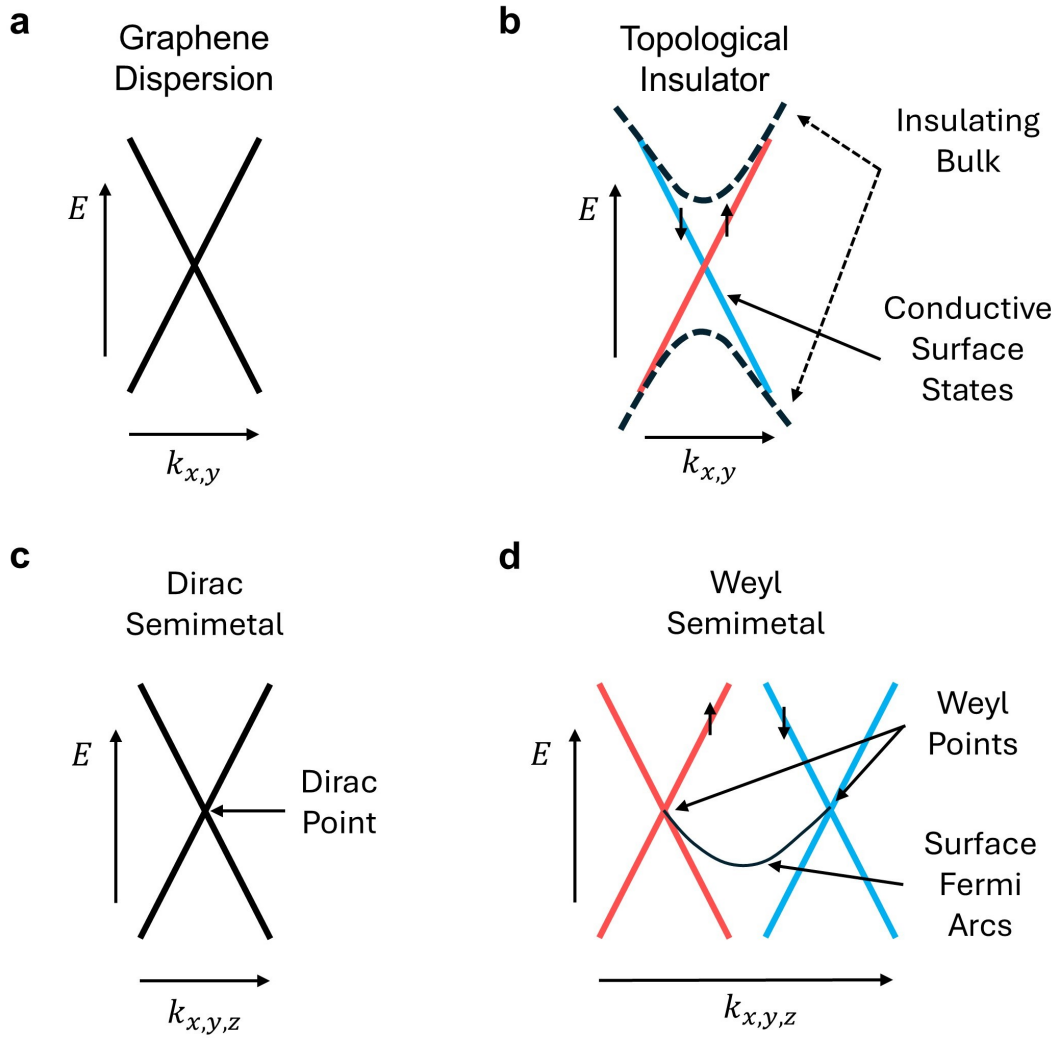

Figure 2.1: Schematic depiction of quantum material light-like electronic structure. (a) A light-like, linear, band dispersion similar to that of graphene at the K and K' valleys of the Brillouin zone. (b) A depiction of a topological insulator (TI) where the bulk of the crystal is insulating but there exist topologically enforced surface states connecting the two bulk bands. These conductive surface states are spin-locked, indicated by the differing colors of the bands. (c) Dirac semimetal bands are illustrated by a light-like dispersion which is partially filled allowing these states to be accessed in transport. (d) Weyl semimetals have the spin degeneracy broken and the differing spin bands separated in momentum. The Weyl points are connected by an extra set of states called Fermi arcs which are surface state sheets that connect the two cones and persist at lower and higher binding energies than the Weyl points (only lower shown for clarity).

optical, and spintronic properties that arise from their symmetry-protected band structures and topological nature, making them important for both basic science research and novel technology applications.

The high mobility of carriers in these systems supports their use in electronic and optoelectronic devices. Their nonlinear optical responses, broadband light absorption, and ultrafast carrier dynamics make them suitable for photodetectors, modulators, and solar cells. In spintronics, effects such as spin-momentum locking and chirality-dependent transport enable efficient spin current generation and manipulation. Fur-

thermore, the ability to tune their electronic structure using external fields, strain, or chemical doping provides flexibility for applications in thermoelectric and quantum technologies. These properties connect fundamental physical principles with practical applications in a wide range of fields.

2.2.1 Graphene

Graphene, a single layer of carbon atoms arranged in a hexagonal lattice, is a Dirac semimetal which is likely the most well known quantum material to the general public. At the K and K' points of its Brillouin zone, graphene exhibits a linear band structure, leading to massless Dirac fermions with high mobility. This electronic structure underlies many of graphene's extraordinary properties, including its ballistic transport at room temperature [33].

As a quantum material, graphene has attracted significant interest due to its exceptional electronic and transport properties. Its linear dispersion results in high carrier mobility, even at room temperature, making it suitable for high-speed electronic devices. Furthermore, the absence of a bandgap allows ballistic transport over micrometer scales, enabling low-dissipation electronic applications. Graphene's unique density of states at the Dirac point contributes to its tunable electronic and optical properties, which can be controlled through electrostatic gating or chemical doping. In addition to these transport properties, graphene exhibits strong interactions with light, making it a valuable material for photodetectors, modulators, and other optoelectronic applications. These properties underscore its importance as a model system for studying quantum phenomena and as a potential component in emerging technologies. In Chapter 4 I utilize a heterogeneous graphene heterostructure as a case study for a real-time machine learning control system for photoemission experiments.

2.2.2 Topological Insulators

Topological insulators are materials that exhibit an insulating bulk and conducting surface states protected by time-reversal symmetry. The reason for the topological character of these materials comes from a strong spin-orbit coupling perturbing the conduction and valence bands to overlap (known as band inversion). The crossings of these overlapping bands are gapped due to the splitting from the spin-orbit interaction. It is this inverted bulk gap where the topological surface states lie, and when time reversal-symmetry is protected they must close the gap [13]. These surface states are characterized by a linear Dirac-like dispersion and spin-momentum locking, where the spin of the electrons is locked perpendicular to their momentum. Unlike graphene, where Dirac cones arise in the bulk and are spin-degenerate, TIs feature spin-polarized surface states that are robust against nonmagnetic impurities and disorder. Materials such as Bi_2Se_3, Bi_2Te_3, and

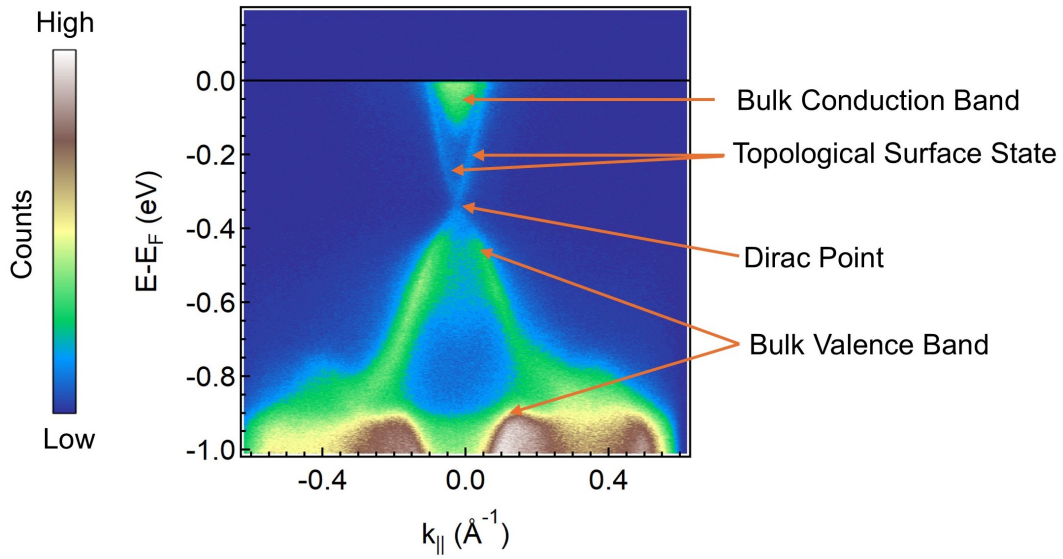

Figure 2.2: ARPES spectrum of Bi_2Se_3 taken with the 21.2eV He discharge lamp at UC Davis. The bulk valence band, bulk conduction band, topological surface state, and Dirac crossing are identified. Image credit to Inna Vishik for the ARPES figure.

Sb_2Te_3 are well-known examples of TIs, with large bulk band gaps and surface states observable at accessible energy scales, making them ideal systems for studying topological phenomena.

The unique properties of TIs have significant implications for both fundamental physics and applications. Spin-momentum locking in the surface states enables efficient spin transport, making TIs promising for spintronic devices. Additionally, the interplay between topological surface states and magnetism can give rise to exotic quantum phenomena, such as the quantum anomalous Hall effect. TIs are also of interest in proximity-induced superconductivity, where pairing in the surface states can lead to the emergence of Majorana bound states, a key ingredient for topological quantum computation. These systems provide a versatile platform to explore the interaction of topology, magnetism, and superconductivity, setting them apart as a distinct class of quantum materials.

In this dissertation, while I do not utilize TIs for a key result in later chapters they were important to my journey to this point. We utilize Bi_2Se_3 as a characteristic test sample when tuning or confirming operation of our ARPES chamber. The spectrum of Bi_2Se_3 has visible bulk and surface states even at room temperature and at low temperature we can utilize the clarity of the sharp surface states to assess the operation of the system. An example of the Bi_2Se_3 spectrum taken with the He discharge lamp at UC Davis is given in Figure 2.2. In addition I performed ARPES measurements on copper doped $Cu_xBi_2Se_3$ to illustrate the persistence of these topologically protected surface states through the intercalation of copper [34].

2.2.3 Dirac Semimetals

Dirac semimetals extend the concept of Dirac dispersions from two-dimensional systems, like graphene, into three dimensions, where Dirac points appear as symmetry-protected degeneracies in the electronic band structure. Unlike the spin-degenerate Dirac cones in graphene, the Dirac points in 3D systems can exist at specific locations in the bulk Brillouin zone, depending on the crystal symmetry and time-reversal symmetry. Examples of 3D Dirac semimetals, such as Cd_3As_2 and Na_3Bi, exhibit linear dispersions along all three momentum directions, leading to unique transport phenomena, including high mobility and large magnetoresistance. Furthermore, in 3D Dirac semimetals, the electronic structure is not restricted to a planar lattice, enabling a richer interplay between electronic, optical, and magnetic properties compared to graphene.

The relevance of Dirac dispersions extends to superconductivity, where features such as symmetry-protected degeneracies and linear band crossings can influence the pairing mechanisms. In nonsymmorphic systems like $LaNiGa_2$, symmetry-enforced degeneracies have been proposed to play a role in stabilizing unconventional superconducting states [1, 35, 2]. These connections highlight the importance of studying Dirac semimetals and related systems to understand both their fundamental properties and their potential role in emergent quantum phases. Compared to graphene, 3D Dirac semimetals provide an expanded framework for exploring how linear band crossings impact macroscopic quantum phenomena, particularly in the presence of strong correlations or external perturbations such as magnetic fields or pressure.

2.2.4 Weyl Semimetals

Weyl semimetals differ from Dirac semimetals in that their band crossings, known as Weyl points, are only singly degenerate instead of twofold degenerate due to the separation of distinct spin bands[36]. This occurs when either time-reversal or inversion symmetry is broken, splitting a Dirac point into pairs of Weyl points with opposite chirality. These points act as monopoles of Berry curvature in momentum space, giving rise to topologically protected Fermi arc surface states that connect Weyl points of opposite chirality. The connecting Fermi arcs provide a technique for experimentally identifying Weyl semimetals even in cases where the Weyl points are unoccupied because the arcs extend to both higher and deeper binding energies than the Weyl points themselves.

Weyl semimetals that break inversion symmetry feature Weyl points with opposite chirality that are separated in momentum space. These materials exhibit unique transport and optical properties arising from the breaking of inversion symmetry, which shifts the Weyl points away from the time-reversal invariant momentum points. A prominent example of such a Weyl semimetal is TaAs, where inversion symmetry

breaking leads to the formation of Weyl points that are separated in momentum space. These materials can exhibit unusual phenomena like chiral magnetic effects and the violation of the Wiedemann-Franz law, making them of interest for fundamental studies in condensed matter physics. It was the reported observation of the Fermi arcs in TaAs that provided the first spectral evidence of Weyl points [37]. The Fermi arcs in these materials also connect Weyl points of opposite chirality, revealing the topological nature of these systems and offering potential for novel applications in quantum transport and optoelectronics.

In contrast, Weyl semimetals that break time-reversal symmetry lead to the emergence of Weyl points with a twofold degeneracy, but this time the splitting is a result of the ferromagnetic ordering or other symmetry-breaking interactions. These materials often exhibit rich magnetotransport properties, such as the chiral anomaly, where the application of a parallel electric and magnetic field leads to an increase in electrical conductivity along the direction of the applied magnetic field. $Co_3Sn_2S_2$ is a well-known example of a Weyl semimetal that breaks time-reversal symmetry. Upon entering a ferromagnetic phase below a critical temperature, the system forms Weyl points that lead to large anomalous Hall conductivity and negative longitudinal magnetoresistance. This characteristic is a direct consequence of the broken time-reversal symmetry, which allows for a nonzero Berry curvature contribution from the Weyl points. The unique magnetotransport properties in these systems make Weyl semimetals that break time-reversal symmetry an important class of materials for exploring new phenomena in quantum transport and spintronic applications.

$Co_3Sn_2S_2$ is an example of a Weyl semimetal which goes through a topological phase transition below a Curie temperature of 177K [38]. Upon entering the ferromagnetic state, the band structure of $Co_3Sn_2S_2$ splits based on spin, breaking time reversal symmetry and forming six Weyl points. Weyl points are also proposed in this material to contribute to a large anomalous Hall conductivity, as well as negative longitudinal magnetoresistance associated with the chiral anomaly [39, 40, 41, 42, 43, 44]. Above the Curie temperature, the Weyl points are absent due to the restoration of T symmetry, but the persistence of local magnetic disorder and many-body effects still contribute to a complex electronic structure above the Curie temperature. The work done in Chapter 5 builds upon these prior works by enhancing our understanding of surface heterogeneity.

2.3 Momentum-Resolved Spectroscopy

Momentum-resolved spectroscopy, such as ARPES, are one of the primary tools for probing the electronic structure of quantum materials. By directly measuring the energy and momentum of electronic states using only the interaction with a photon, ARPES provides a unique window into the band structure and Fermi surface of materials. This capability is particularly crucial for systems with linear dispersions, such as Dirac

and Weyl semimetals, where the direct observations can show linear dispersions even when the light-like dispersion is well below the Fermi level and therefore does not contribute to transport or the linear crossing only contributes a small fraction to the total density of states.

For Dirac semimetals, ARPES has been instrumental in confirming the presence of symmetry-protected Dirac points and mapping their associated dispersions. In Weyl semimetals, ARPES enables the direct observation of Weyl points and their accompanying Fermi arcs, features that arise from the bulk-boundary correspondence in topological systems. These measurements are essential for understanding how symmetry breaking, such as magnetic ordering in $Co_3Sn_2S_2$, leads to the emergence or annihilation of Weyl points. Furthermore, ARPES has played a critical role in studying moiré-engineered systems like magic-angle twisted bilayer graphene, where flat bands near the Dirac points are linked to strongly correlated electronic phases, including superconductivity. This detailed insight into the momentum-resolved electronic structure provides a foundation for connecting the microscopic properties of quantum materials to their macroscopic properties.

Spatially resolved ARPES allows us to probe quantum materials in ways that large spot sizes prohibit. The small spot size improves data quality by reducing sample surface inhomogeneity across the photoemitting spot. Additionally many two-dimensional materials and especially heterostructures thereof cannot be fabricated to macroscopic scales and therefore can only be studied by micro or nano focused spot sizes. As mentioned in the surface sensitivity Section 1.3.5, the photon energy tunability of synchrotron light sources also enables ARPES to distinguish bulk from surface states in the electronic structure which has been utilized to identify TIs.

In the remainder of this dissertation I will cover ARPES experiments on three quantum materials: $LaNiGa_2$, Graphene, and $Co_3Sn_2S_2$. In Chapter 3 I describe the first ARPES studies on $LaNiGa_2$ and confirm the spectral signatures of the calculated electronic structure. Next, Chapter 4 addresses an experimental problem with ARPES by providing a real-time machine learning control system utilizing a graphene heterostructure as a prototypical example. Finally in Chapter 5 I study the correlation between the XPS and ARPES spectra in the Weyl semimetal $Co_3Sn_2S_2$.

Chapter 3

Symmetry-Enforced Fermi Surface Degeneracies Observed in the Purported Time-Reversal Symmetry-Broken Superconductor $LaNiGa_2$

The project focused on $LaNiGa_2$ spanned much of my graduate school experience with the very first attempted ARPES measurements of $LaNiGa_2$ single crystals happening on April 26th 2019, just three months before I joined the Vishik group. As a coauthor on Jackson Badger's 2022 paper reporting the growth of single crystals and the corrected space group [1] contributed the first ARPES measurements on $LaNiGa_2$. In the following years and through the Covid pandemic I performed more than a half a dozen synchrotron beamline experiments on $LaNiGa_2$. The result of these comprehensive ARPES measurements was a paper published as an editor's choice in PRB in 2024 [2]. The pursuit of high quality spectra for this project has taught me much of what I know about ARPES which inspired Section 1.4. The content of this chapter originates from the manuscript of my 2024 paper.

3.1 Introduction

Unconventional superconductors have mechanisms or phenomena that differ from superconductors described by Bardeen-Cooper-Schrieffer (BCS) theory. The normal state electronic properties of unconventional superconductors can inform their superconducting mechanism as well as identify factors that raise or lower the transition temperature, T_c. For example, the experimentally established Fermiology of iron based superconductors influenced early proposals of interband pairing [45, 46], and in cuprate high-temperature superconductors, the normal-state pseudogap presents one of the most formidable challenges to establishing the superconducting mechanism [47, 48]. Among superconductors that have been reported to break time reversal symmetry below T_c, Sr_2RuO_4 has been the most heavily investigated, and its normal-state band structure, particularly the van hove singularity [49, 50], has been implicated in the origin of superconductivity and the evolution of T_c under strain [51]. In other classes of superconductors, there are examples of isostructural materials that alternately break/maintain time reversal symmetry in the superconducting state, providing further indication that details of Fermiology can play a role in the pairing state [52].

Time-reversal symmetry breaking (TRSB) superconductivity is relatively rare, with only several dozen single-material (not heterostructure) candidates identified to date [53, 1], and many of these compounds have magnetism or magnetic fluctuations which may play a role in mediating TRSB superconductivity [54, 55, 56]. $LaNiGa_2$ is a rare example where magnetism is absent due to the Ni bands being filled [35, 57]. This material has a superconducting transition temperature, $T_c \approx 2$K [58], and most prior studies have been performed on polycrystalline specimens. μSR experiments reported the onset of spontaneous magnetization below T_c, interpreted as demonstrating TRSB superconductivity [59].

The recent synthesis of single crystals has enabled a wider array of experiments to understand structural, thermodynamic, and electronic properties relevant to the superconducting mechanism [1]. More than enabling new experiments, these single crystals demonstrated that the space group was previously mis-identified as Cmmm, with the correct space group being Cmcm, which is nonsymmorphic. The Cmcm space group imposes symmetry-enforced degeneracies at the k_z Brillouin zone boundary ($Z-T-A$ plane, figure 3.1(a)-(b)). Spin-orbit coupling (SOC) splits this degeneracy everywhere except for the $k_x = 0$ line on that plane, but only slightly [35]. The symmetry enforced degeneracies and near-degeneracies of this space group are predicted to have involvement in the order parameter in $LaNiGa_2$ [35], and nonsymmorphic symmetries may more generally enhance T_c for odd parity superconducting states [60].

Other materials in the Cmcm space group have recently garnered attention due to the degenerate features of their band structures. $TaNiTe_5$ and $TaPtTe_5$ are two such examples of non-superconducting Cmcm crystals that have been shown by ARPES to have Dirac nodal lines at the BZ boundary [61, 62]. Being

non-superconducting, these compounds show that it is not just the space group and related Fermi surface degeneracies that make $LaNiGa_2$ a superconductor.

Here we present the experimental normal-state electronic structure of TRSB superconductor $LaNiGa_2$ throughout the entire 3D BZ, as measured by ARPES. The following results are presented: (1) broad agreement between density functional theory (DFT) and measured electronic structure throughout the 3D BZ. (2) Evidence for Fermi surface degeneracies on $Z-T-A$ plane, within resolution of experiment, via distinct bands merging into one approaching this plane in parallel (figure 3.1(c)-(d)). (3) Evidence of predicted linear-crossings of all bands when cutting perpendicular to $Z-T-A$ plane (figure 3.1(e)). (4) Evidence for near-degeneracies of bands throughout the BZ separate from those on the $Z-T-A$ plane. The relevance of these features to the proposed mechanism of unconventional superconductivity are discussed.

3.2 Methods

Crystal growth and ARPES Measurements The samples were grown using the technique described in the original single-crystal growth by Badger et al. [1].

ARPES measurements were performed at Stanford Synchrotron Radiation Lightsource (SSRL) beamline $5-2$. Samples were cleaved *in-situ* at pressure better than 5×10^{-11} Torr and at temperatures less than $15K$. The photon energy was varied as stated in relevant figures. The energy and momentum resolution of the experiments were 25 meV and $\approx 0.01\text{Å}^{-1}$ respectively. The beam spot size was approximately $20\mu m\times30\mu m$ ('microARPES') for all experiments.

$LaNiGa_2$ single crystals grow in a platelet shape with typical dimensions of $2mm\times2mm\times\lesssim0.3mm$ (figure 3.3 (a)-(b)). The platelet-shaped samples are most naturally cleaved *in-situ* by mounting a ceramic top post on top of the platelet, hereafter called the 'natural cleave' orientation. Cleaving the crystal in the natural orientation allows for ARPES that approximately probes of planes of constant k_y. In order to probe band structure at roughly constant values of k_z or k_x without relying exclusively on the lower-resolution photon energy tuning method, we mounted the platelet samples on their thin-edge. This was done by etching a groove into the sample holder and adhering the sample into the groove. The samples were mounted into the groove with ultrahigh vacuum compatible Locktite, and a conductive pathway created with the silver epoxy Epo-tek H21D.

For data shown here, the samples were pre-aligned using Laue to have the $\vec{a}$ axis normal to the sample holder. Figure 3.2 shows the Laue diffraction image of a $LaNiGa_2$ platelet in a grayscale image with the simulated diffraction peaks in red. In particular, the fine peaks near the center of the image distinguish the $\vec{a}$ and $\vec{c}$ axes effectively by having two large peaks and one large peak respectively. The thin-edge-

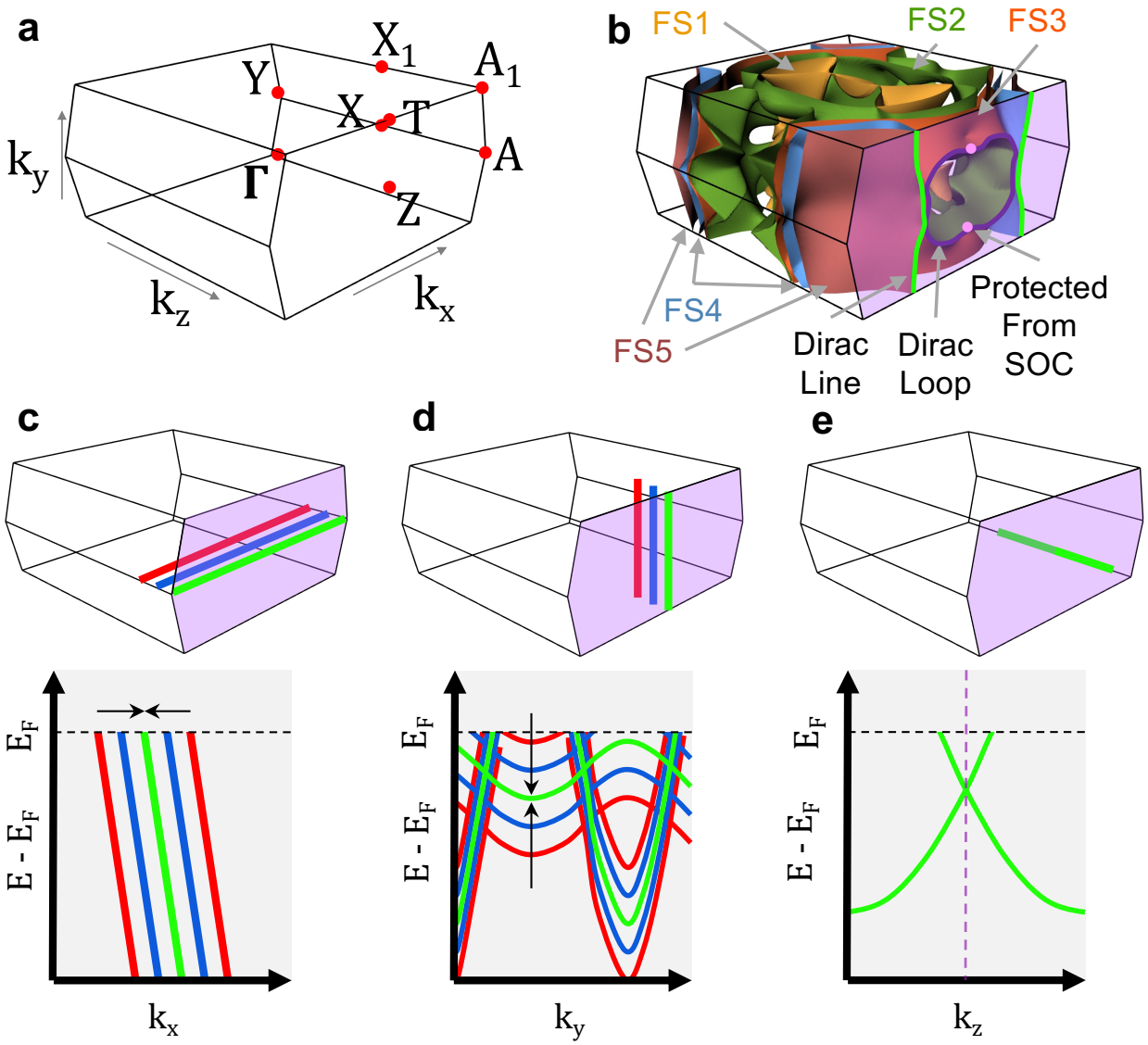

Figure 3.1: Predicted Fermiology and Nodal Plane Features (a) The base centered orthorhombic Brillouin zone with high symmetry points and axes labeled. The purported nodal plane is the k_z boundary, or the $Z-T-A$ plane, colored in purple in panels (b)-(e). (b) The five Fermi surfaces of $LaNiGa_2$ shown in the Brillouin zone, reproduced from Ref. [1]. The pink dots indicate the SOC protected nodal points. Features labeled 'nodal line' and 'nodal loop' are degenerate crossings at E_F that get split by SOC. (c)-(e) Schematic of predicted band structure when accessing the nodal plane 3 different ways. (c)-(d) cuts parallel to the nodal plane are expected to show band merging in energy and momentum. (e) When piercing the predicted nodal plane, parallel to k_z, the calculations predict a Dirac crossing of bands.

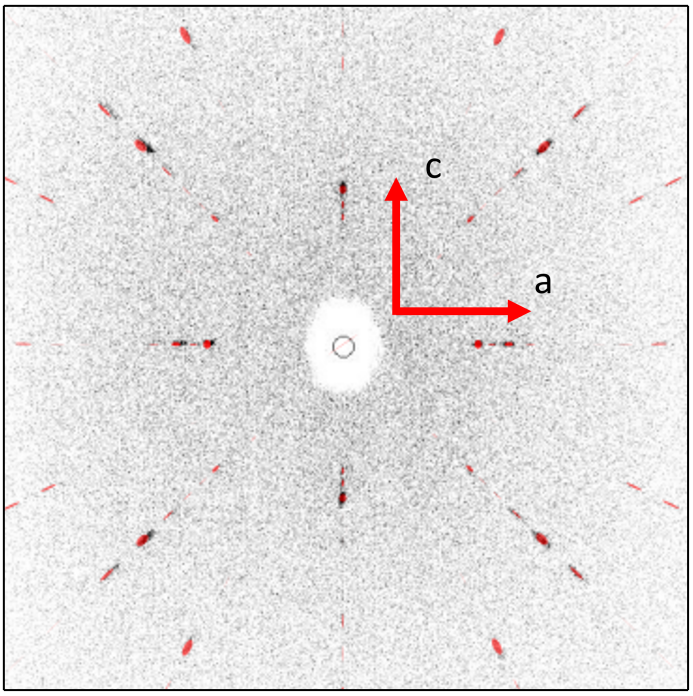

Figure 3.2: Laue image of $LaNiGa_2$ sample showing the orientations of the a and c axes. The red dots are the simulated diffraction peaks, taking into account both the X-ray source intensity and the structure factor. The simulation well distinguishes between the a and c axes. This orientation allows for samples to be mounted on the thin edge with the desired axis normal to the sample holder.

mounted samples were broken *in-situ* using a flat-edged wobble stick to apply uniform pressure across the face without using a top post. This configuration of thin-edge cleaving was used to probe the k_y dependence of the electronic structure directly with ARPES. Due to the small size of the cleaved regions that arise from the thin-edge method, microARPES is crucial for enabling measurements of these samples.

Electronic Structure Calculations

Density functional theory calculations were carried out using the full-potential linearized augmented planewave code WIEN2K [63]. We used the Perdew-Burke-Ernzerhof (PBE) version of the generalized gradient approximation as the exchange-correlation functional [64]. The atomic coordinates used for these calculations were those listed in refs. [1, 35]. The muffin-tin sphere sizes were 2.50 a.u for La; 2.32 a.u for Ni, and 2.20 a.u for Ga. The plane wave cutoff was determined by $R_{mt}^{min} K_{max} = 7$, and the k-point mesh used was $34 \times 34 \times 33$. The effects of spin-orbit coupling were included by using the second variational method as implemented in WIEN2K.

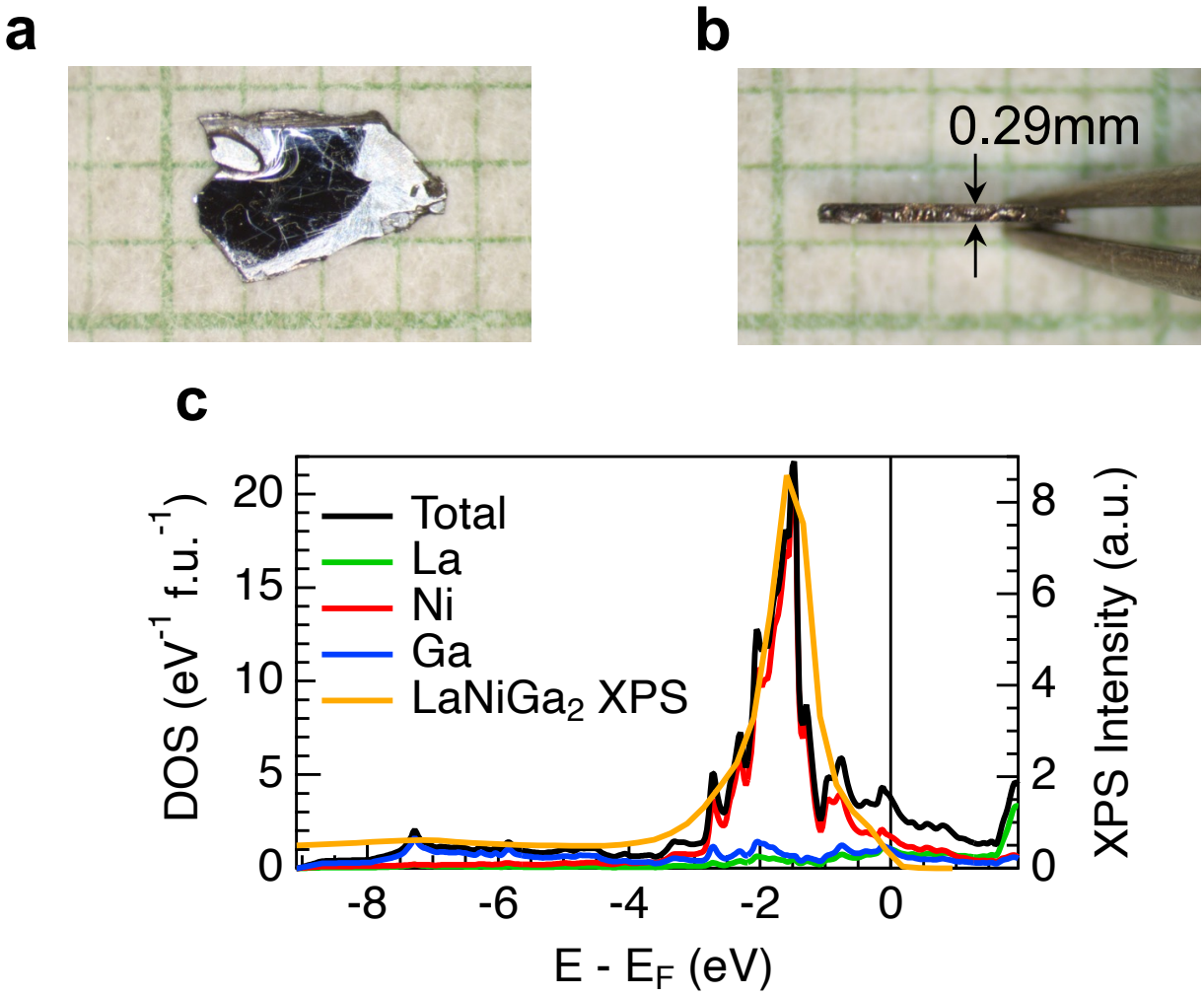

Figure 3.3: Sample Dimensions and XPS (a) $LaNiGa_2$ sample pictured on millimeter paper showing typical shape and size of the platelet crystals in the a-c plane (natural orientation). (b) Image of the sample held on its side (thin-edge orientation). (c) Projected density of states calculations along with XPS measured with 144 eV photons in the natural orientation.

3.3 Results

figure 3.3(c) shows an angle-integrated valence band spectrum, together with calculated partial and total density of states. These XPS data were collected on the same natural cleave as ARPES data. Maps of constant energy at the Fermi level (E_F), yielding Fermi surface maps, are shown for four characteristic planes in momentum space in figure 3.4. The associated DFT calculations are partially superimposed to establish the alignment between theoretical and experimental Fermiology. The displayed planes of the BZ are schematically shown in panel (a) by orange, red, green, and blue lines which correspond to (b) $k_x = 0$ (144 eV), (c) $k_y = 0$ (116 eV)), (c) $k_y = 0.516 \cdot 2\pi/c$ (124 eV), (e) $k_y = 2\pi/c$ (132 eV) respectively. Data for panel (b) were collected in the thin-edge orientation directly probing the $k_x = 0$ plane, which permits spectra orthogonal to the purported nodal plane. Broader photon energy dependence was performed from 110 eV to 144 eV, and is shown in figures 1.6 1.4, 1.5. A further discussion of photon energy dependence and determining V_0 is given in Section 1.2.3.

As discussed, one defining feature of the predicted electronic structure is pairs of bands merging together when approaching the $Z - T - A$ plane with parallel cuts. This is shown in figure 3.5 and contrasted with spectra near the orthogonal zone boundary. Panels (a1-a4) show the spectra approaching (a1,a2), on (a3), and past (a4) the predicted nodal plane. Panel (b) similarly shows the spectra approaching (b1, b2) and on (b3) the zone boundary orthogonal to the predicted nodal plane. Panel (c) shows the described locations of the cuts in panel (a) and (b) overlaid a constant energy map integrated ± 50 meV around the Fermi level. Panel (a) has two separated bands in panels (a1, a2) that appear to merge in panel (a3) and split again in (a4). Panel (b) also shows two well separated bands in panel (b1) that closely approach each other in panel (b3). Whereas spectra in (a2) and (b2) have similar linewidth, the spectrum in (a3) is considerably sharper than (b3). Calculated electronic structure for these cuts is overlaid with their color corresponding to the Fermi surface number given in figure 3.1.

With the thin-edge cleave perpendicular to k_x, we can visualize bands merging in energy approaching the $Z - T - A$ plane, because the observed bands have band bottoms at lower binding energy. In figure 3.5 we only discuss merging in momentum because the band bottoms are well below the displayed energy range. Nevertheless, for cuts approaching the purported nodal plane in parallel, bands always merge in both energy and momentum. Figure 3.6 shows spectra along three parallel cuts moving progressively further from the zone boundary (panels (b1-b3)). In panel (c), we compare energy distribution curves (EDCs) at the $k_y = 0$ point, where a band bottom is located. Panel (b1), taken along the zone boundary, shows a single band in the spectrum and a single peak in the EDC. As one moves away from the zone boundary, the bands split in two as seen both in the image plots and the EDCs. The magnitude of this split is ≈ 200 meV for cuts

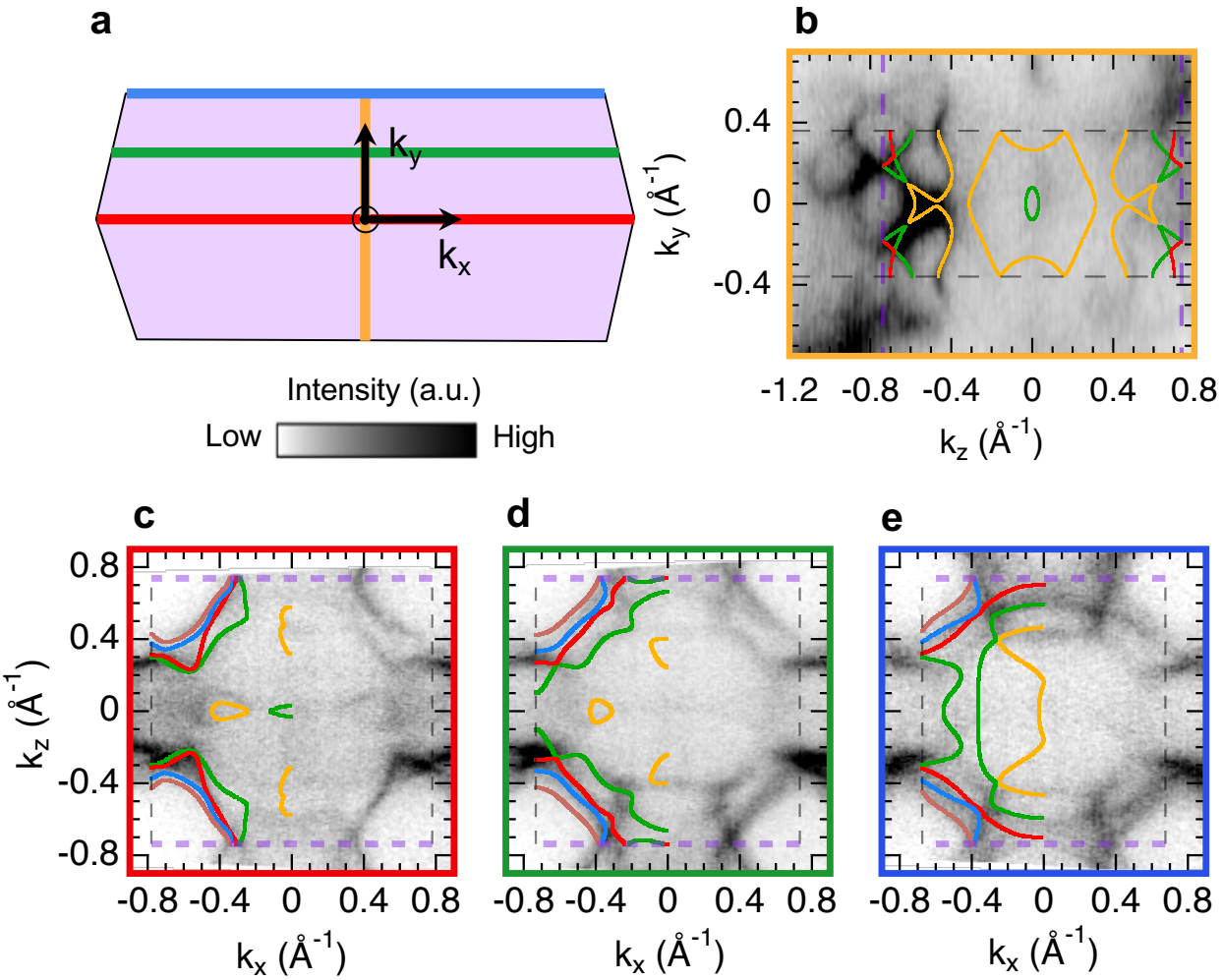

Figure 3.4: Observed Fermiology for selected planes in BZ. (a) Projection of the BZ showing locations of the planes with colored lines corresponding to the borders in (b-e). (b) Constant energy map integrated $45m$ eV around the Fermi energy at 144 eV in the thin-edge orientation. (c-e) ARPES constant energy maps integrated $50m$ eV around the Fermi energy. Measured in the natural platelet orientation at 116 eV, 124 eV and 132 eV respectively to access the center, predicted k_y of the SOC protected nodal point, and the top of the BZ. DFT calculated Fermi crossings shown in (b-e) are colored corresponding to the Fermi surfaces in figure 3.1. In (c-e) they are only overlaid on half of the zone for clarity of the data. Purple plane in (a) and dashed lines in (b-e) indicate $Z-T-A$ plane location. Black dashed lines indicate the other boundary of the BZ.

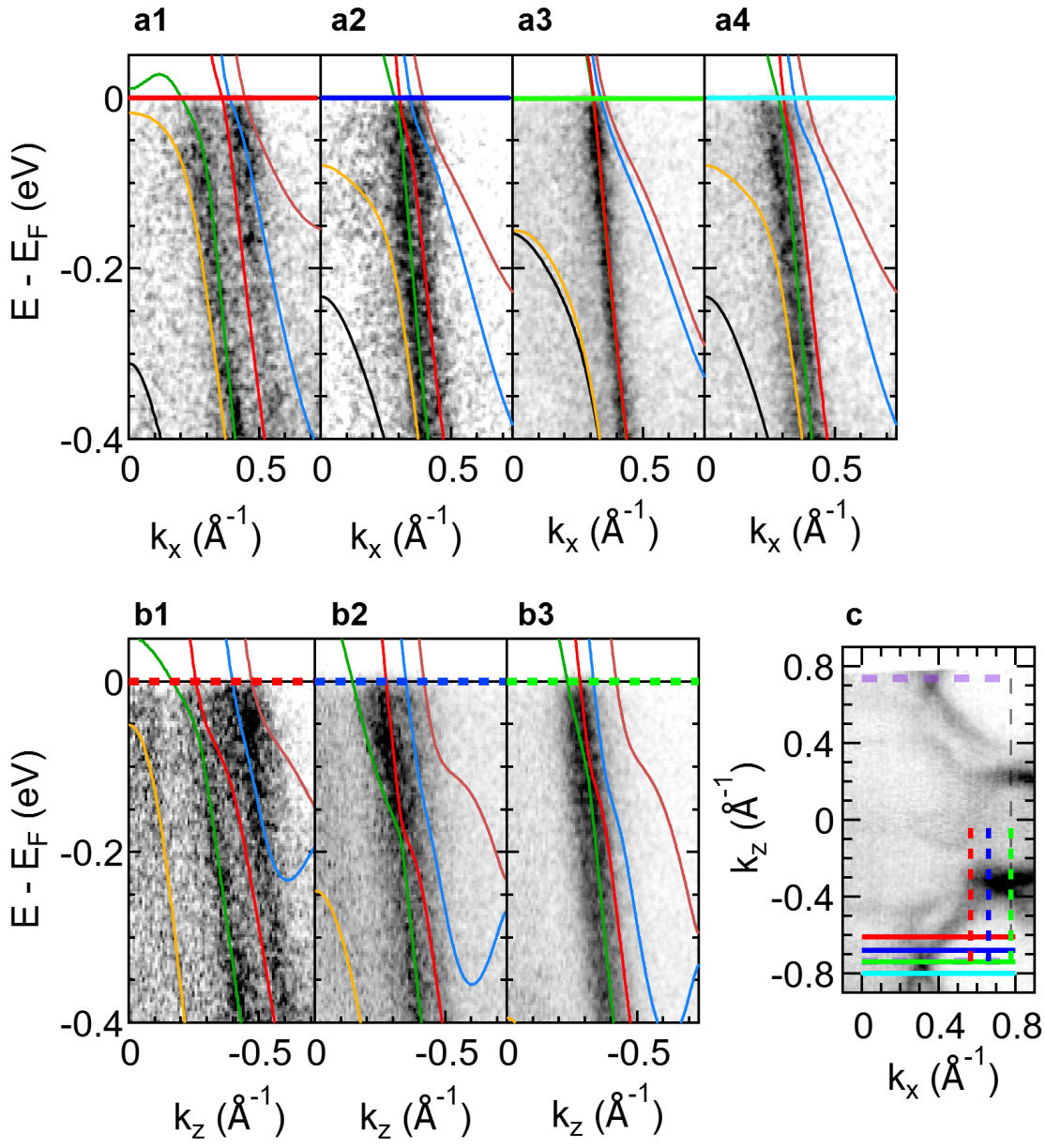

Figure 3.5: Band merging in momentum at zone boundaries. (a1-a4) Spectra approaching (a1,a2) at (a3) and beyond (a4) the $Z-T-A$ plane as a function of k_z. (b1-b3) Spectra approaching (b1,b2) and on (b3) the BZ boundary along k_x. (c) Constant energy map at the Fermi level indicating the location of the spectra in (a) and (b). (a-b) DFT predicted bands are overlaid according to the color of the FS they create in figure 3.1. All spectra collected with 120 eV photons

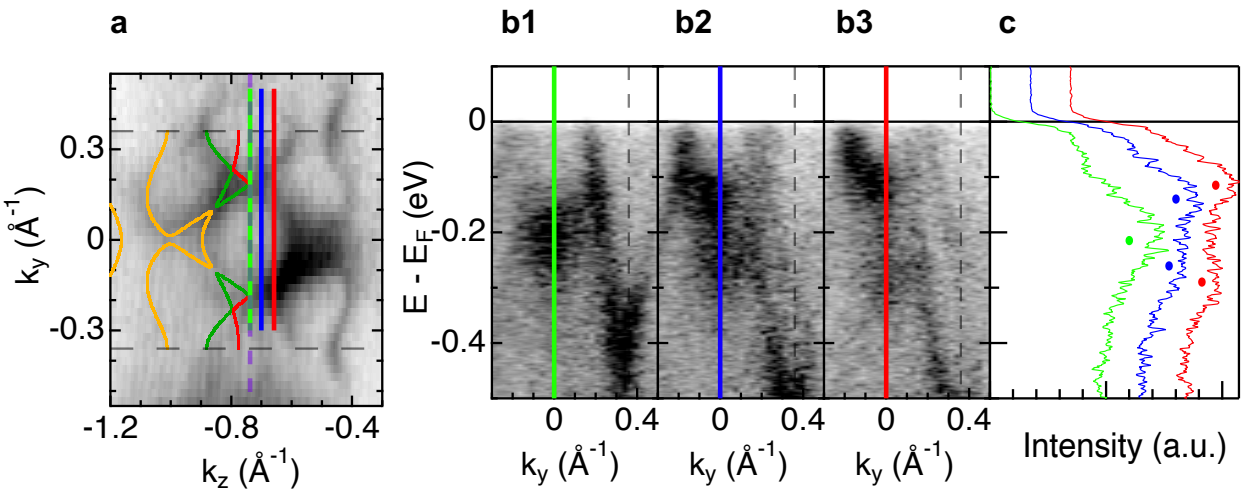

Figure 3.6: Band merging in energy, thin-edge cleave. (a) Fermi level constant energy contour cropped from figure 3.4 (b) showing locations of cuts in (b1)-(b3). Black and purple dashed lines indicate BZ boundaries. (b1)-(b3) ARPES spectra at three parallel cuts (c) $k_y = 0$ EDCs of panels (b1)-(b3) in green, blue, offset for clarity. Dots in panel (c) are guide-to-the-eye for peak position.

differing by $\approx 6\%$ of the BZ.

So far we have provided evidence for band degeneracy at the $Z-T-A$ plane by investigating the spectra along lines parallel to the $Z-T-A$ plane. The second predicted signature of the k_z BZ boundary is that for all cuts perpendicular to it, all bands which cross the $Z-T-A$ plane should do so with a Dirac-like (linear) crossing, up to SOC. In figure 3.7 (a) we show a spectrum along the k_z axis that shows a Dirac-like crossing at the $Z-T-A$ (purple dashed line) 0.2 eV below E_F. That spectrum, being along the k_z axis, intercepts the nodal plane along the $Z-T$ line and is therefore predicted to be protected against SOC splitting due to an additional symmetry. In panels (b1) - (b3) of figure 3.7 we show three parallel cuts that intersect the $Z-T-A$ plane successively closer to the purported nodal line. In the experimental spectra, two linear crossings are clearly seen in (b1), which successively move to lower binding energy approaching the momentum marked by the 'X'-shaped feature in the Fermi surface map (c). Finally, at the purported nodal line (b3), a linear crossing is observed right at E_F. The crossings in (b) are not protected from SOC and are therefore gapped, but their gap size too small to be resolved with the present experiments. The bottom of panels (a)-(b) show the DFT calculated dispersion in the corresponding locations.

3.4 Discussion

We begin by addressing the lack of magnetism in $LaNiGa_2$, previously justified by filled Ni-3d bands. In the density of states (DOS) from DFT calculations, these filled bands yield a large peak at ≈ 1.8 eV binding energy in figure 3.3 (c). The measured XPS intensity, a rough proxy for the DOS, is consistent with this

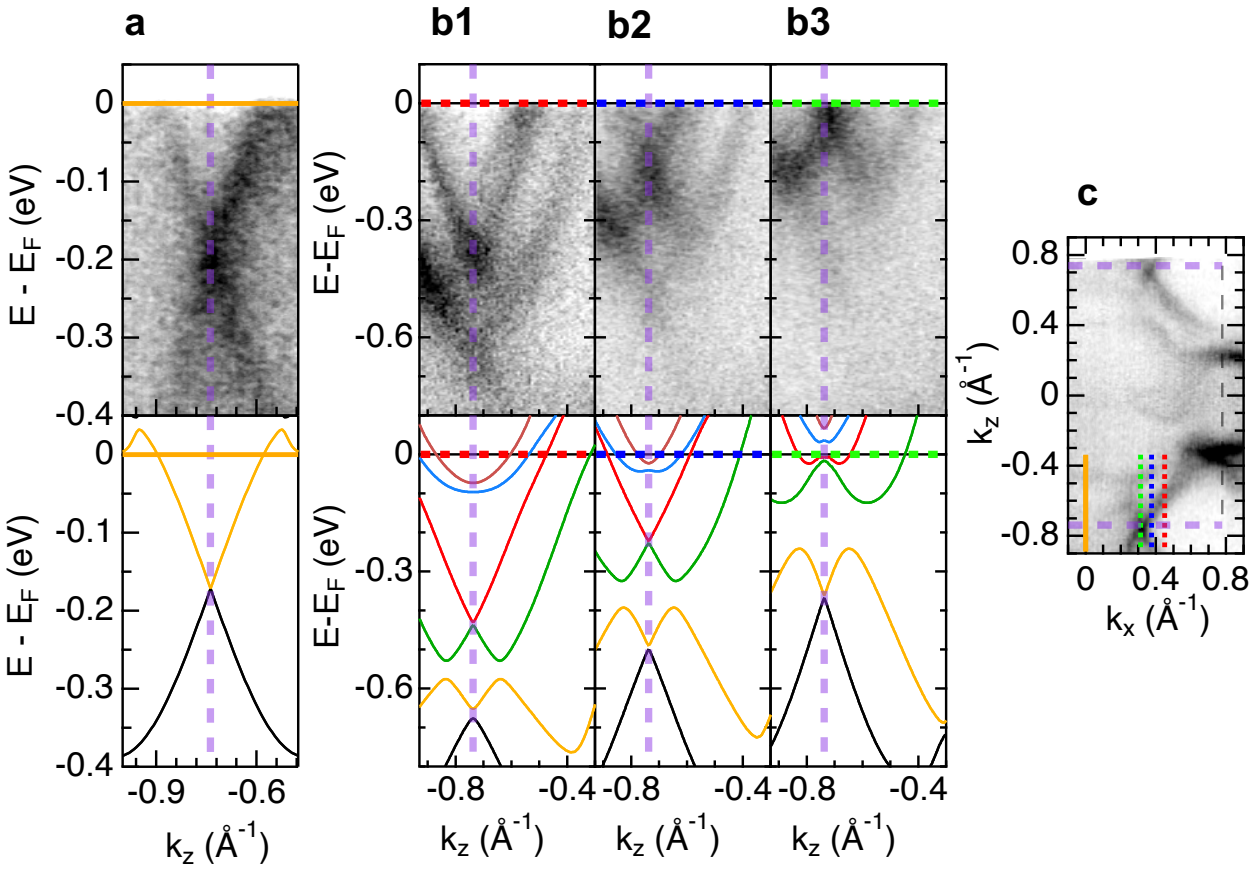

Figure 3.7: Linear crossings for cuts perpendicular to nodal plane. (a) Thin edge orientation spectrum taken along the $\Gamma - Z$ line at a photon energy of 144 eV. (b) Spectra taken in the natural orientation with 120 eV photons near a Fermi crossing at the zone boundary. (c) Constant energy contour from the natural orientation indicating the location of cuts in (a-b). The cut from (a) is at $k_y = 0\text{Å}^{-1}$ while (b-c) are at $k_y \approx 0.09\text{Å}^{-1}$. (a-b)(bottom) DFT predicted bands are shown according to the color of the FS they create in figure 3.1.

calculated feature, supporting the stated absence of magnetism in this compound. We also note that recent nuclear magnetic/quadrupolar resonance and magnetization measurements in the normal state further do not find evidence of magnetic fluctuations or enhanced paramagnetism [65].

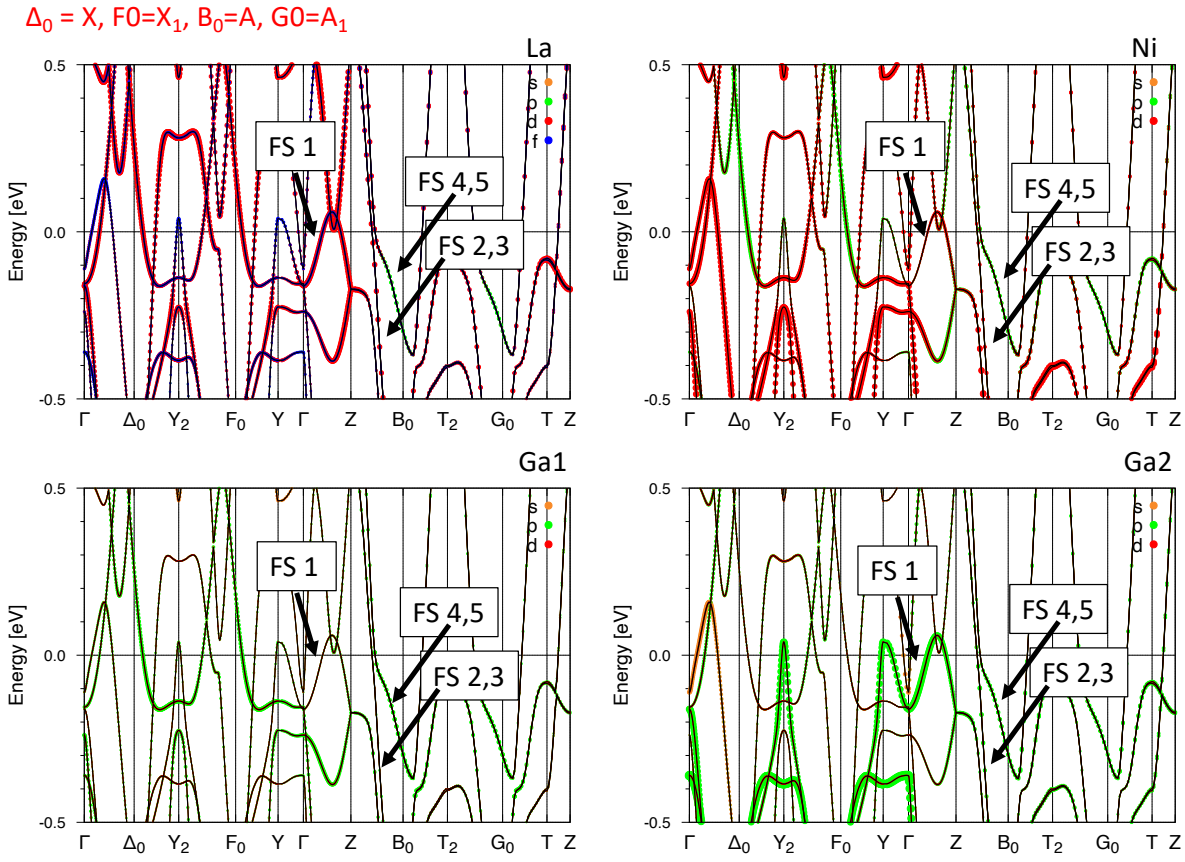

Figure 3.8: Orbital projections of $LaNiGa_2$'s band structure without SOC. The bands associated with the five Fermi surfaces are labeled in each panel. The legend at the top left shows the label associated with the Brillouin zone in Figure 3.1 (a). The nearest region in this figure to compare the main text figures are as follows: (Figure 3.5, $Z - A$ and $X - A$), (Figure 3.5, $Z - T$), (Figure 3.7, $\Gamma - Z$ and $X - A$).

We now turn to the measured band structure, where we observe overall good agreement between DFT and experiment throughout the 3D BZ. We note strong matrix element effects [66], which is the reason why certain bands are observed more, less, or not at all in certain regions of the BZ. An example of this is FS 4-5 in Figure 3.5, where photoemission signal from the bands that form FS 4-5 (blue and maroon) are not seen in the displayed cuts. In that region of the BZ, FS 2 and 3 have primarily d-orbital character, while FS 1, 4 and 5 are primarily of p-orbital character, and this difference in orbital character is the likely reason that we do not observe FS 4 and 5. The calculated orbital projected band structure is shown in 3.8. The four panels illustrate the contributions of the s, p, d, and f orbitals of each atom to the calculated band structure.

The variation of the orbital character across the Brillouin zone contributes to the variable photoemission intensity through the matrix element effect [66]. The regions which most affect our observations are labeled with the relevant Fermi surface numbers in each of the panels.

For bands that are visible in the data, there are minor discrepancies between measured and predicted bands, particularly in the most 3-dimensional bands which form FS 1 and 2. This can be seen in Figure 3.4 (c) where the 'teardrop' shaped pocket of FS 1 near $k_x = -0.4\text{Å}^{-1}$ is observed to be larger than predicted. Further, in panel (d) we observe elongated features of FS 1 and 2 that appear similar to those of panel (e). The more 2D Fermi surfaces (FS 3-5), when visible, show no substantial disagreement with the predicted electronic structure. Additionally, FS 1 and 2 show strong agreement with predictions in the thin-edge cleave shown in Figure 3.4 (b).

The disagreements seen of FS 1 and 2 are then either: (1) real features of the electronic structure not captured by the calculations, and constrained to only small portions of the BZ or (2) artifacts arising from the photoemission process due to momentum uncertainty in the $k_\perp$ direction. Arguing against scenario (1), there is very good agreement between ARPES Fermi surfaces and DFT with regards to FS1 and 2 in the thin-edge cleave data. Elaborating on (2), the short inelastic mean free path (IMFP) of electrons makes ARPES a surface sensitive measurement in the present range of photon energies. We calculate the IMFP of electrons with kinetic energy of 110 eV traveling through $LaNiGa_2$ to be $\lambda = 5$Å using a common empirical method [67]. This IMFP leads to an appreciable quantum uncertainty of the perpendicular momentum $\Delta k_\perp = 1/\lambda = 0.2\text{Å}^{-1}$ [9], comprising $\approx 25\%$ of the BZ along k_y. Additionally, in ARPES measurements there can be preferential sampling of bands which are being probed by the spectrometer slit normal to their constant-energy surface. These two effects —$k_\perp$ broadening and extremum-selective sampling —may explain the discrepancies observed in figure 3.4 as the extremum position observed for FS 1 is at $k_y \approx 0.016\text{Å}^{-1}$.

Now we turn to focus on the observed features at the purported nodal plane. The first observation is bands merging when approaching the $Z - T - A$ plane with parallel cuts (Figure 3.5, 3.6). While the calculations predict SOC splitting of the bands along the nodal plane at all positions except the $Z - T$ line, the splitting is extremely small in most locations. In figure 3.5 (a3) the splitting between FS 2 and 3 is 5 meV, much smaller than our experimental resolution. Also predicted are Dirac-like crossings for all bands when piercing the nodal plane in perpendicular. This is observed for several distinct bands in Figure 3.7 Momentum-space band merging can be additionally visualized in Fermi surface maps, particularly in figure 3.4 (c)-(e) and Figure 3.5 (c), and many other examples shown in Figure 1.6 show an 'X'-shaped feature at the BZ boundary along one direction (k_z) but not along the other (k_y), consistent with the location of the nodal plane. Notably, most of these observations are discernible from data alone, independent from comparison to DFT calculations.

Beyond the nodal plane, we also present evidence for near-degeneracies throughout the BZ. These near-degeneracies are particularly persistent at the orthogonal zone boundary (k_x). FS 2 and 3 have near degeneracies not only along the orthogonal BZ boundary but within the BZ at many values of k_y. Near-degeneracies are observed in both the thin-edge Fermi surface as well as broad ranges of the photon energy dependent natural-cleave Fermiology. Four clear examples can be seen of near-degeneracies within the BZ in figure 3.4: First, panel (b) shows degeneracy of FS 2 and 3 at $k_z \approx -0.65\text{Å}^{-1}$. Second, panel (c) shows a near-degeneracy of FS 2 and 3 at $k_x \approx -0.55\text{Å}^{-1}$ where the bands are almost stuck until they reach the k_x zone boundary. Third, panel (d) shows FS 2 and 3 again nearly degenerate and then stuck near the k_x boundary. Finally, panel (e) again shows FS 2 and 3 being nearly degenerate inside the BZ at $k_z \approx -0.35\text{Å}^{-1}$ nearly co-located with a near degeneracy of FS 3 and 4.

We now connect these results to prior work on this material. Early experiments have laid out a set of constraints for the pairing symmetry and mechanism of $LaNiGa_2$. The point group symmetry of the crystal structure, which remains unchanged with the newly assigned space group, only permits four order parameters that break time reversal symmetry [59, 35]. All are non-unitary and all have weak SOC, the latter constraint which is confirmed with the present data. Additionally, heat capacity and superfluid density were shown to be inconsistent with nodes of any kind, and also demonstrated to be more consistent with a two-gap model than a single-gap BCS fitting [68, 1, 69].

Together, these results point to a fully-gapped triplet state. The Cooper pair wavefunction must be odd overall to comport with Fermion exchange, so an even spin component implies an odd spatial component. This presents a problem when one includes information about the Fermiology, as an odd spatial wavefunction must change sign across the Γ point, so a Fermi surface that encloses Γ should have a node, inconsistent with experiments. The calculated Fermiology based on both the previous Cmmm [57] and refined Cmcm [1, 35] crystal structure includes Fermi surfaces which envelop the Γ point. In the present calculation, this includes a small pocket of FS1, as well as FS2 and 3. Previously, this apparent inconsistency was resolved by considering the multiband nature of this material, wherein triplet pairing between nearly degenerate Fermi surfaces can ensure an overall odd wavefunction [70], if the order parameter changes sign upon swapping band index. This proposed internally antisymmetric nonunitary triplet pairing (INT) state appears to be consistent with all experimental results about the superconductivity in $LaNiGa_2$ to date: TRSB below T_c [59], nodeless superconducting gap [68, 1], consistency with two gaps [71], and insensitivity of superconductivity to non-magnetic impurities [72].

The present work adds experimentally-motivated plausibility to that argument, and proposes further experiments to understand and optimize superconductivity in $LaNiGa_2$. The Cmcm space group imposes symmetry-enforced degeneracies along one plane of the BZ, the so-called 'nodal plane.' Our experiments

find support for this in three ways: bands merging in momentum approaching the nodal plane with parallel cuts (figure 3.5), bands merging in energy approaching the nodal plane with parallel cuts (figure 3.6), and all cuts perpendicular to the nodal plane yielding Dirac-like crossings for all bands at all energies (figure 3.7). Although SOC lifts this degeneracy on most of the nodal plane, there are still three sources of degeneracy and near-degeneracy to support interband pairing: (1) symmetry-enforced exact degeneracy at predicted nodal points along $Z - T$ line (2) near-degeneracy on nodal lines and nodal loop arising from symmetry coupled with a small (m̃eV) amount of SOC (3) accidental near-degeneracies including on the k_x BZ boundary (figure 3.5(b)). The latter was present in band structure calculations based on the previous Cmmm structure, but the former two are a consequence of the Cmcm structure. The overall strong agreement between DFT calculations and experiment throughout the 3D BZ further supports the prediction of a nodal plane, as well as the presence of only weak SOC [59], which is required for the experimentally-compatible pairing states.

Despite the growing body of knowledge on $LaNiGa_2$, accelerated by the availability of single crystals, questions still remain. Interband pairing benefits from near-degeneracies throughout the BZ; the ones on the nodal plane will remain as long as the space group remains unchanged, but the ones outside the nodal plane may be tunable by uniaxial strain. The effect of this tuning on T_c can further confirm the pairing mechanism that appears to be supported by a plurality of experiments. Moreover, it can clarify if there are pairing interactions outside of electron-phonon [73] which is the primary candidate in $LaNiGa_2$, such as originating magnetic phases which often accompany TRSB superconductor. As an example of this, $LaNiC_2$ was also thought to be entirely non-magnetic, until pressure-dependent studies on single-crystals revealed a hidden antiferromagnetic regime [74].

Another important direction is substitutional carrier tuning, which is expected to maintain the nodal points, maintain near-degeneracies on the nodal plane, but tune the presence of small hole-like pockets throughout the BZ, clarifying their role in superconductivity, which is heretofore not considered in detail. These new experiments should be pursued in conjunction with revisiting foundational results about this material. In other materials, claims of TRSB superconductivity have become less clear as more experimental evidence emerged, most prominently in Sr_2RuO_4 [75, 76]. With that insight, we emphasize the importance of repeating zero field μSR measurements, as well as other experiments sensitive to TRSB in the superconducting state, on single crystals of $LaNiGa_2$ where the surface/volume ratio is smaller and the constituency of impurities and inclusions may also be different.

Unconventional superconductors are a very broad class likely to contain a diverse set of novel pairing mechanisms. The subset of those that break time reversal symmetry is quite small, and the subset of these TRSB superconductors that do not contain nearby magnetism is smaller yet. The present high quality data, including in the unconventional thin-edge cleave geometry demonstrates that $LaNiGa_2$ can continue

to yield experimental insights on momentum space electronic structure and can serve as a benchmark for this set of rare superconductors. One other example of TRSB superconductivity without nearby magnetism is 4Hb-TaS_2. However, being a 2D Van der Waals material, 4Hb-TaS_2 likely does not allow for a thin-edge cleave to be achieved in the same way that $LaNiGa_2$ is shown to here.

3.5 Conclusions

We have performed the first comprehensive ARPES study of purported TRSB superconductor $LaNiGa_2$ throughout the 3D BZ and demonstrated that this material yields high quality ARPES spectra. This work has enhanced our understanding beyond the first ARPES study on $LaNiGa_2$ (Ref. [1]) in the following ways: 1) multiple distinct evidences for the nodal plane seen comprehensively throughout the BZ, including cuts both perpendicular and parallel to the nodal plane; 2) showing a filled Ni-3d band in XPS measurements and new calculations, giving evidence for a nominally-non-magnetic bulk; 3) more accurate assessment of inner potential and correspondence between photon energy and perpendicular momentum, crucial for efficient followup ARPES studies targeting specific band features; 4) demonstration of thin-edge cleaving in platelet-like specimens to yield ARPES spectra of comparable quality to conventional cleaving, with implications for further surface spectroscopy studies of platelet-shaped specimens. Superconductivity is a low-energy phenomenon which necessarily is affected by the Fermiology of a material. This is particularly true in the case of $LaNiGa_2$ which has an expected gap size of $k_B T_c \approx 0.6$ meV [35]. The Cmcm space group enforces band degeneracies at the k_z boundary, which constrains any Fermi surface that crosses that plane to be degenerate with another. $LaNiGa_2$ has 4 Fermi surfaces which cross the $Z-T$ plane, two of which cross the additionally protected $Z-T$ line and are degenerate even with SOC. These degenerate Fermi surfaces are predicted to provide the platform which allows for the interband superconductivity.

Our results have given evidence that predicted degenerate Fermi crossings are present within our measurement resolution, and also shown that in other regions of the BZ there are symmetry enforced as well as accidental nearly-degenerate crossings. These nearly degenerate crossings are most prominent at the k_x boundaries. Known superconductors in nonsymmorphic space groups are a fruitful avenue to search for TRSB [1], and $LaNiGa_2$ is emblematic of the important interplay between normal-state Fermiology and superconductivity inherent in this approach.

Chapter 4

AARDVARK: Adaptive Automation and Real-time Data Visualization for All Research Kit

The Adaptive Automation and Real-time Data Visualization for All Research Kit (AARDVARK)[1] project is the fruit of a doctoral fellowship in residence I took part in at the Advanced Light Source (ALS) synchrotron at the Lawrence Berkeley National Lab. Beamtime at synchrotron ARPES endstations, and in particular ALS's Maestro beamline 7.0.2 is a heavily sought after and oversubscribed resource. During a beamtime the users that I have spoken with all report spending 3-4 hours of a 24 hour beamtime on finding microscopic location on a macroscopic sample and alignment that they actually want to spend their time performing careful measurements on. The goal of this project was to incorporate real-time machine learning and automation to reduce the amount of time wasted not performing the measurements of scientific interest. This chapter contains the contents of a manuscript about the AARDVARK project that is currently in preparation.

4.1 Introduction

ARPES is an extremely surface sensitive technique with information rich datasets [5]. Micro- and nano-focused light sources, particularly those of synchrotron light sources like the Advanced Light Source, have broadened the types of materials that can be measured with ARPES and enabled researchers to target

[1] This acronym was inspired by a discussion with my friend Zach Sweger who when I asked what I should call the project immediately and without reason responded "Aardvark". I worked with some generative AI tools and found an acronym which described the project well enough.

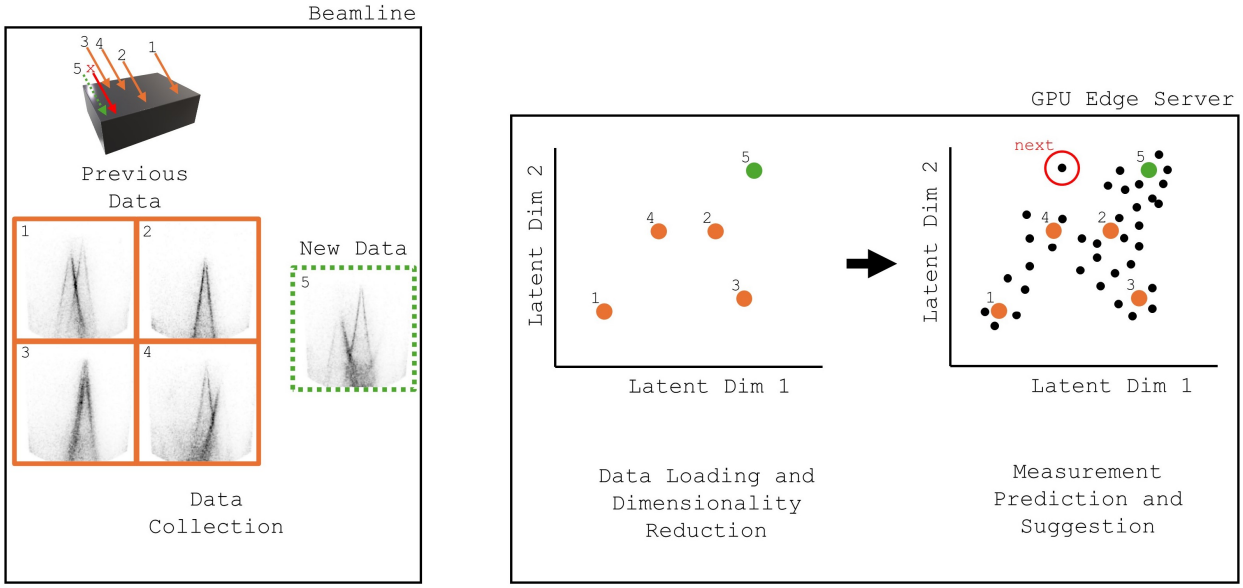

Figure 4.1: Schematic overview for the the AARDVARK system. Data is collected at the beamline end station and saved to disk. The beamline requests a new position to measure and begins measuring a new location. Asynchronously the GPU edge server is loading all new data and repeating the machine learning pipeline. The machine learning pipeline ends by overwriting the list of next positions to measure with an updated list. We schematically show only one measurement suggestion but in practice the server adapts the number of suggestions it creates to ensure there are always positions available for the beamline upon request.

desired regions of the sample. The surface sensitivity requires preparation of a clean surface right before the measurement. The types of surface preparation for ARPES experiments include cleaving, exfoliation, growth, removal of a cap layer. Due to the necessity of surface preparation it is rarely possible to characterize the surface of a sample prior to performing an ARPES experiment. The types of heterogeneity that can exist on the surface of a sample include: roughness, curvature, different atomic terminations, ripping or tearing from exfoliation, step edges. The surface of a sample also degrades over time due to a number of factors: adsorption of trace gasses in the UHV chamber, ions can migrate from one termination to another, damage from exposure to the X-ray beam. In addition to the finite experimental time due to sample degradation, most state of the art beamlines are oversubscribed which means researchers only have 24-72hrs of beamtime to perform all of their experiments. All of these factors combined emphasize the need to streamline experiments so users can spend less of their valuable beamtime on finding their desired part of a sample and more time taking the data that targets their scientific goals.

ARPES experiments typically start with a lengthy process of scanning the fresh surface for the region to understand the spatial makeup of the spectra and find which region is best suited for the particular science goals of that experiment. This 'best' quality is highly dependent on the material being studied. A few examples are: sharpest spectra, specific local chemical composition, specific structural feature such as the edge of a sample. The most regularly employed technique to find the characteristic locations on the fresh

surface is to scan a grid of locations and have the experiment user analyze the data for the best location. This raster-grid technique is very time consuming with most users performing multiple of them during a given experiment.

This work describes an alternative to the common raster-grid approach by employing real time machine learning to the sample search process enabling users to have more time for their scientific goals. As described in Figure 4.1 an AARDVARK scan works by launching an asynchronous machine learning loop to constantly provide the best next measurements to the experiment end-station. The experiment sends data about the spectrum and location to the server and then requests the next measurement location. The AARDVARK server then rapidly responds with the next measurement location due to suggestions being sent in batches that are cached for fast response times. At the same time the server is constantly running a loop of (1) load newly collected data, (2) use a machine learning pipeline to process the data, (3) evaluate current knowledge of sample surface with a Gaussian process and (4) compute an acquisition function to suggest a new batch of unmeasured points to be collected. This machine learning loop is done on a GPU accelerated edge server which allows it to provide a new batch of suggestions every 6 seconds on average.

4.2 Methods

4.2.1 Uniform Manifold Approximation and Projection (UMAP)

In order to make a decision on which location to measure next, the algorithm must predict what the spectra will look like at a given location. The most naive implementation of this prediction is prohibitively expensive as it involves fitting a model with 100 - 1,000,000 output features depending on the spectra being collected. In order to combat this version of the curse of dimensionality, we use a dimensionality reduction step to compact the information of our spectra into fewer features. In this work we use Uniform Manifold Approximation and Projection (UMAP) [77, 78] in order to reduce the space which we must train our model on. The implementation of UMAP used here is from the RAPIDS cuML package [79] which is based on the implementations from refs [77, 78]. With this acceleration we are able to fit and transform hundreds of full resolution (approximately 1000×1000) ARPES spectra in approximately one second. The rapidity of prediction using GPU acceleration allows for our algorithm to provide new optimal measurement suggestions every few seconds depending on how many spectra and of what size are being collected.

The choice of embedding into a 3 dimensional UMAP space enables immediate user feedback on the progress of the experiment by visualizing the 3 UMAP dimensions as red, green, and blue channels as shown in Figure 4.2. For the visualization, each of the 3 UMAP dimensions (x, y, z) are scaled to the same range

[0, 255] such that they can be visualized as a color. With this visualization similar colors in general have similar spectra while distinct colors generally have distinct spectra. Because the UMAP algorithm is non-deterministic and heavily dependent on the spectra as well as a random seed that each run of the UMAP visualization will in general have different colors representing each region.

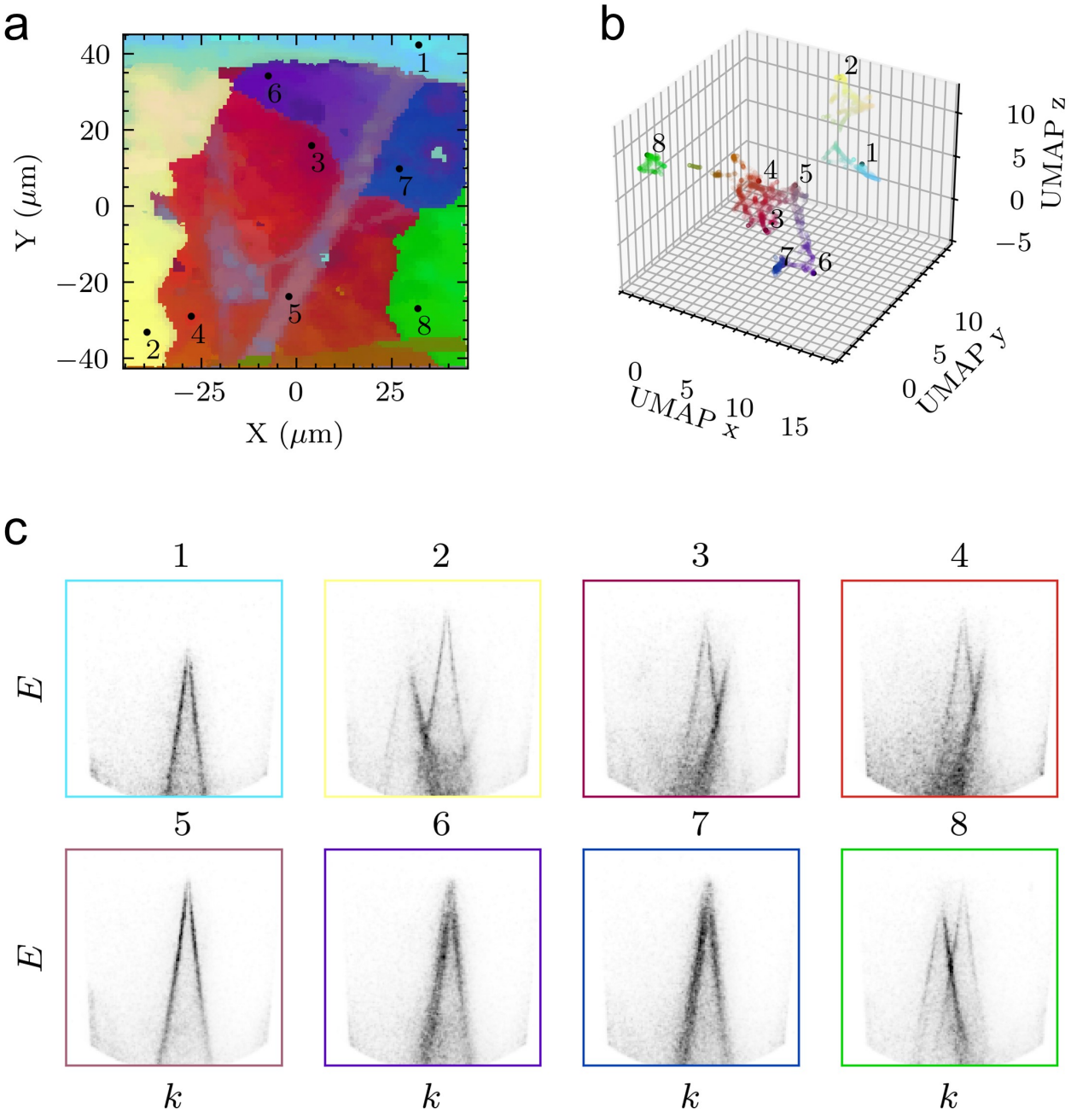

Figure 4.2: Colorized UMAP embeddings. (a) Spatial plot of the UMAP embedded ARPES data. The colors are made by scaling the range of the UMAP x, y, z coordinates to [0, 255] such that they can be displayed as an R, G, B color respectively. (b) The set of all ARPES spectra shown in their UMAP dimensionality reduced space with the markers colored based on the same procedure described in (a). (c) ARPES spectra taken at the locations indicated by the black marker and numbers in (a) and (b).

In Figure 4.2 (c) we show ARPES spectra collected on a hetero structure of SiO_2 / single-crystal graphene / poly-crystalline graphene. SiO_2 is an insulator with the valence band maximum much deeper than the graphene Dirac cones being probed. The single-crystal graphene layer has a single orientation over the whole field of view which is spectroscopically seen as the persistent Dirac cone that is near the center of the momentum window. The top polycrystalline graphene layer provides a secondary Dirac cone whose momentum varies with the twist angle between the two sheets of graphene. The twist angle and bonding strength of the two layers also effects the Fermi level which varies the energy of both Dirac cones. We performed simulated experiments on a ground truth dataset consisting of a 91×91 grid. At each position of this grid 3 measurements were taken: (1) ARPES of the Dirac cone, (2) XPS of the Si $2p$ core level, and (3) XPS of the C $1s$ core level. AARDVARK experiments were then simulated on these dataset to produce the results shown in this work. The positions and UMAP color visualizations of the spectra are shown in panel (a) and the 3D UMAP embedding is shown in panel (b). Various regions are seen in the UMAP color visualization that correspond to the following local characteristics in (c): (1) noisy spectra, (2, 3, 4, 8) various large twist angles between the poly-crystalline top sheet and single crystal bottom sheet, (5) regions where the top layer has cracked and reveal only the bottom layer, and (6, 7) regions with very small but slightly varied twist angles.

4.2.2 Gaussian Process Regression

A Gaussian process regression is a method for non-linear fitting that excels when one has a small dataset and does not know the functional form that the data should be fit to. Here, we utilize GPyTorch a GPU accelerated implementation of Gaussian processes from ref. [80]. The process of spatially exploring ARPES or XPS spectra of a sample fit both of these criteria because we start from no initial data and do not know the samples spatial makeup prior to the experiment. Many in depth explanations of the operation of a Gaussian process exist with some even targeting ARPES specifically so curious readers are encouraged to explore those resources [81, 82]. For this work we can take this as the effective definition of a Gaussian process: A model that can perform a non-linear fit to data and provide expected values and variances of measurements at inputs that have not been measured. Neural networks are another popular method for performing non-linear fits that do not fit our use case because they require a large amount of data relative to their fitting parameters to make useful predictions. Due to the lack of data inherent in searching a new sample a Gaussian process is better suited to the task than a neural network.

Identifying the interesting regions of a sample can be performed by using a multitask Gaussian process [83] hand tuned to your experiment. For ARPES experiments these hand tuned tasks may related to the intensity

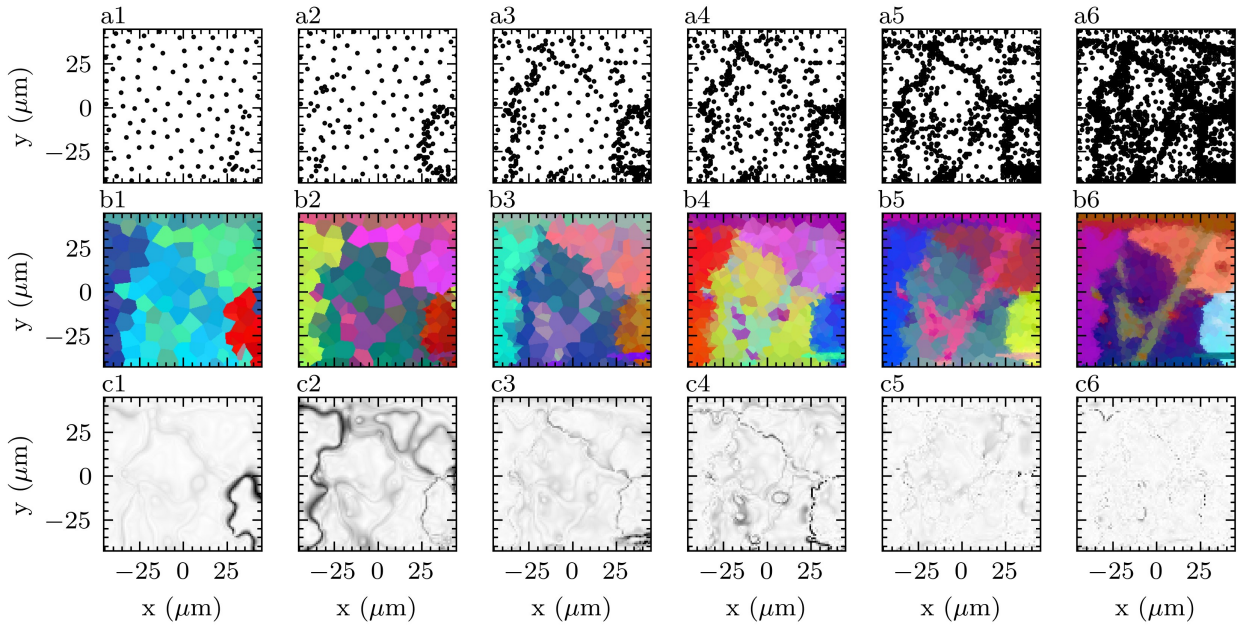

Figure 4.3: Progression of an AARDVARK scan on ARPES data. (a) Coordinates of sampled data with (125, 200, 400, 600, 1000, 2000) points measured are shown in (a1-a6) respectively. (b) Nearest-neighbor colorized 3-dimensional UMAP embeddings of ARPES spectra collected at the points shown in (a). Different colors indicate different spectral features as found by the dimensionality reduction method UMAP. (c) The acquisition function that is used to determine the priority of following measurements. Darker pixels indicate a higher measurement priority.

and curvature of the image. For an XPS experiment the tasks may be more specific, involving the line-shapes of the resolved peaks instead of simply their intensity. In this work we use UMAP as a dimensionality reduction step on both ARPES and XPS spectra and use the UMAP coordinates as Gaussian process targets. The use of the UMAP coordinates as a Gaussian process target allows the algorithm to be independent of the particulars of a given experiment and work for both XPS and ARPES experiments. To emphasize exploration of unknown spectra the algorithm fits a multitask Gaussian process to the UMAP coordinates and prioritizes the next measurements to be those whose UMAP coordinates furthest from any existing measurement. This process favors exploration of borders first by definition because the Gaussian process fits a continuous function to the existing measurements. Once the borders have been sampled up to the user's defined resolution, the algorithm is forced to explore the interior of the regions because duplicated measurements are not allowed within a tolerance specified by the user. The acquisition can be described by the following equation.

$$f_a(\mathbf{x}) = \min(\|\mathbf{U}(\mathbf{x}) - \mathbf{U}(\mathbf{x}_{\text{obs}})\|) \tag{4.1}$$

Where $\mathbf{U}(\mathbf{x})$ is the UMAP embedding predicted by the Gaussian process for the position $\mathbf{x}$ and $\mathbf{U}(\mathbf{x}_{\text{obs}})$ are the UMAP embeddings of the current measurements that the Gaussian process was trained on.

4.3 Results

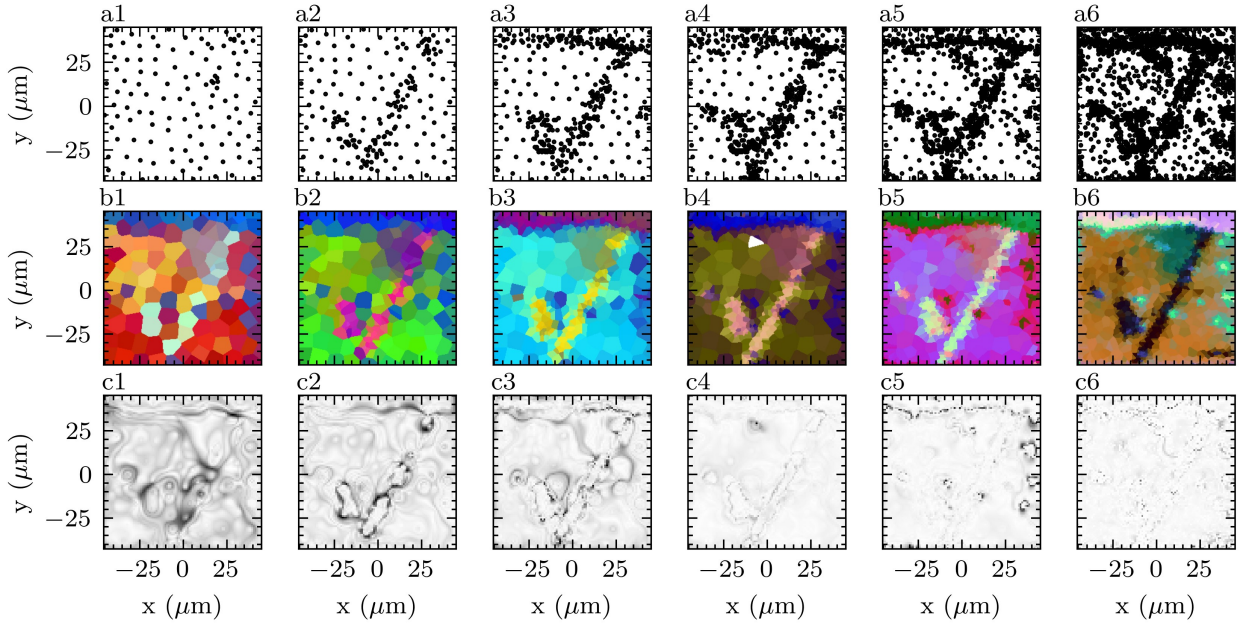

Figure 4.4: Progression of an AARDVARK scan on XPS data. (a) Coordinates of sampled data with (125, 200, 400, 600, 1000, 2000) points measured are shown in (a1-a6) respectively. (b) Nearest-neighbor colorized 3-dimensional UMAP embeddings of XPS spectra of the Si 2*p* core level collected at the points shown in (a). Different colors indicate different spectral features as found by the dimensionality reduction method UMAP. (c) The acquisition function that is used to determine the priority of following measurements. Darker pixels indicate a higher measurement priority.

In Figure 4.3 we show the progression of an AARDVARK experiment set to collect the ARPES spectra of the sample. The top row of panels (a1-a6) show the locations of measurements after (125, 200, 400, 600, 1000, 2000) measurements were taken. AARDVARK made new decisions for measurements every 6 seconds on average during this experiment. The middle row of panels (b1-b6) shows the colorized UMAP embedding of the ARPES spectra collected at the positions shown in panels (a1-a6). The lower row (c1-c6) shows the acquisition function described in equation 4.1 where the darker regions represent the highest acquisition value.

There are 6 dominant regions observed in the ARPES experiment that are shown in the full dataset in Figure 4.2 with their characteristic spectra shown in panel (c): (1, 2, 3/4, 5, 6/7, 8). After 400 measurements AARDVARK is able to find and define the borders of these major region as is observed in the locations measured (a3) and the colorized UMAP (b3).

In contrast to the ARPES experiment shown in Figure 4.3 we show the a simulated experiment on the XPS spectra of the Si 2*p* core level in Figure 4.4. Panels (a1-a6) again show the positions of the collected measurements after (125, 200, 400, 600, 1000, 2000) points had been taken. Figure 4.4 (b1-b6) show the colorized UMAP embedding of the XPS spectra collected at the points shown in (a1-a6). Panels (c1-c6)

show the evolution of the acquisition function over the course of the simulated XPS experiment.

The region surrounding the check mark feature are observed to be more uniform in their Si $2p$ XPS spectrum than that seen in the ARPES experiment in Figure 4.3 as indicated by their UMAP colorization in Figure 4.4 (b1-b6). In the Si $2p$ XPS spectra we observe only 4 dominant regions - pink, green, brown, and black in (b6) along with some small scattered features in teal. From the sharp and isolated Dirac cone seen in Figure 4.2 (c5) the check mark region is observed to be a region where the top polycrystalline graphene sheet has cracked and exposed only the mono crystalline graphene below it. The Si $2p$ core level originates from the substrate and can then be used as a proxy for the thickness of the heterostrcuture on top of it, as is seen where the check mark feature is contrasted from it's surrounding in the XPS colorized UMAP of Figure 4.4.

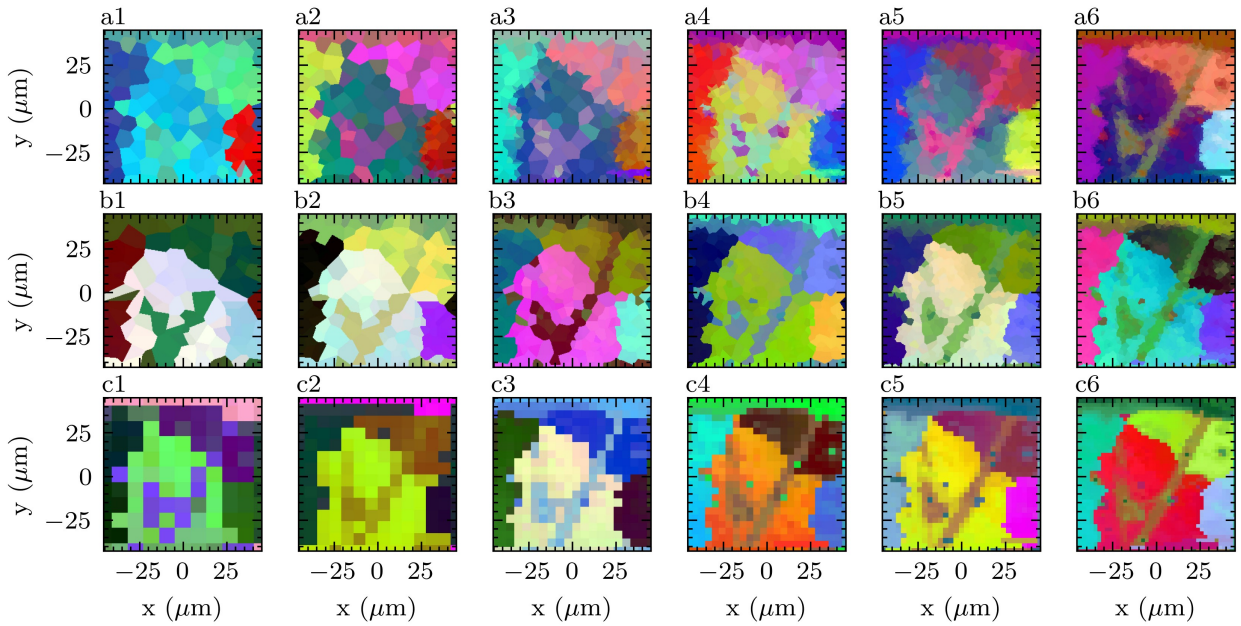

Figure 4.5: Comparison of AARDVARK operation on ARPES data with random or grid search. Rows (a-c) show the progression of scans using AARDVARK, random positions, and grid searches respectively. Panels (1-6) show colorized UMAP visualizations of an scans with (125, 200, 400, 600, 1000, 2000) points measured respectively. In the case of a grid search the closest square number is used to simulate a scan of approximately the same number of points (e.g. 121 instead of 125).

4.4 Discussion

Autonomous, ML/AI powered, and human-in-the-loop control systems are a fast advancing research topic that is accelerating experiments across fields. Previous work doing post-experiment analysis has shown that KMeans classification and Gaussian processes may be sufficient to explore a sample using ARPES [84]. Additionally, autonomous ARPES has been performed by employing a Gaussian process on tasks hand-tuned

to frequent goals of high intensity and sharp spectra [85]. Other works have demonstrated that real time ML can dramatically speed up experiment performance in X-ray microscopy experiments at synchrotrons [86]. AARDVARK deploys a modular architecture that allows for extension to new ML frameworks and demonstrates that UMAP as a general purpose Gaussian process target provides fast exploration of samples for both ARPES and XPS.

The most common method of sample exploration is a raster-grid search where a user specifies a range and step size to explore the sample in a grid. While common the raster-grid search requires the user to know the exact region to explore and at what resolution before performing the search. If too low of a resolution is chosen users will have to take another search over an updated range with better resolution. If too high of a resolution is chosen then the user must wait a long time to get information about the sample because the search sweeps across the sample.

An alternative method which is rarely used is a random search of the sample. A random search has the benefit of providing the user rapid feedback of the entire sample surface but fails to focus on any important features due to it's indiscriminate nature. A random search can also waste time by repeating measurements nearby other measurements in regions that can be expected to be relatively homogeneous from the prior data.

AARDVARK provides a method for searching the surface of a sample that provides the user with rapid feedback of the whole sample surface and focuses on defining region boundaries while being general purpose enough to work on ARPES or XPS data. In Figure 4.5 we show a comparison of an AARDVARK scan (a1-a6), a random search (b1-b6) and a set of grid searches (c1-c6) which all contain roughly the same number of measurements per column (125, 200, 400, 600, 1000, 2000) respectively. After 400-600 points collected the AARDVARK scan (a3-4) can be seen to show as much or more spatial information about the surface than either the random or the grid scan have at 1000-2000 points (b6, c6). In particular, AARDVARK locates and defines the boundaries of the regions as well as finding small features like the small crack on the lower right side of the sample. It should be noted as well that in a real world test a grid search would not appear as it does in the lower row (c1-c6) because the user must first specify the total number of points desired. The more direct comparison of a grid scan would then be a scan with the resolution of perhaps (c5) which only has seen 60% of the sample when compared to AARDVARK in (a4).

Figures 4.3 and 4.4 highlight the general purpose utility of AARDVARK as the same algorithm with no changes is able to effectively search a sample using different spectroscopic measurements. In the XPS spectra of the Si $2p$ core level there are spatial inhomogeneities where the thickness of the heterostrcuture is varied but little to no difference in the spectra from regions of differing twist angle. In contrast, the ARPES spectra show large spatial inhomogeneity where the twist angle changes due to the different location

of the polycrystalline graphene Dirac cone. The generality of the UMAP embedding approach allows for AARDVARK to account for this difference and explore the ARPES and XPS datasets in a different fashion, as seen in the locations of the measurements in Figure 4.3 (a1-a6) and Figure 4.4 (a1-a6). A raster-grid search or a random search would not be able to account for such differences and would then treat both experiments and datasets in the same manner. In addition to saving user beamtime during an experiment the AARDVARK scan can be used when there is a concern over beam radiation damage because it gives the user equal feedback with fewer measurements.

4.5 Conclusions

Here we presented AARDVARK, a modular and generalizable framework for sample exploration that uses dimensionality reduction and Gaussian process regression to guide initial sample searches of ARPES and XPS experiments. By utilizing UMAP as a target for a Gaussian process, AARDVARK efficiently identifies boundaries of spectroscopically distinct regions, dynamically adapting to variations in sample characteristics for ARPES and XPS measurements. This method reduces the time and resources needed for spatially resolved spectroscopy, reducing the time needed to understand the spatial structure of a sample over traditional raster-grid or random sampling strategies.

Our results demonstrate that AARDVARK adapts its measurement priorities based on observed data, ensuring a more thorough exploration of region boundaries with fewer data points than raster-grid searches or random searches. As shown in figures 4.3 and 4.4, AARDVARK identifies critical spectral variations across different measurement types, highlighting its utility in complex samples where intrinsic heterogeneity may vary between spectroscopic modes. This capability enables users of the Maestro beamline at the Advanced Light Source to access their desired scientific goals faster by reducing the time needed to spend measuring the spatial inhomogeneity of the samples. Through the application of a multitask Gaussian process on UMAP embeddings, AARDVARK enables real-time decision-making in measurement selection, optimizing data acquisition and presenting a robust method for future autonomous sample exploration in both ARPES and XPS studies.

Chapter 5

Spatial Heterogeneity and Machine Learning Analysis of $Co_3Sn_2S_2$

This chapter contains my contributions to a manuscript currently in preparation focusing on $Co_3Sn_2S_2$. I have spent more beamtime measuring this material than any other thanks to its diverse spatial heterogeneity and accessible topological phase transitions as a function of temperature. It was clear through our experience at beamtimes that the spatial heterogeneity of the ARPES spectra "correlated" strongly to that of the Sulfur $2p$ XPS spectra. My contributions to this project involved using machine learning to quantify and visualize the correlations that we observed.

5.1 Introduction

$Co_3Sn_2S_2$ exhibits surface heterogeneity with a variety of terminations that can broadly be classified as sulfur terminated, tin terminated, or mixed [38, 87, 88, 89]. In this chapter, I analyze the spatial dependence of ARPES and XPS measurements to explore the correlation in these datasets as the termination varies. Using both traditional techniques of integrating intensity inside person-chosen regions of spectra as well as machine learning, the relationship of the ARPES and XPS spectra of $Co_3Sn_2S_2$ is shown. This analysis provides a foundation for interpreting and correlating the spatial heterogeneity of hyper-spectral and spectral datasets such as ARPES and XPS.

The in depth experiments of spatial heterogeneity would not be possible without the ability to perform ARPES and XPS measurements with micro focused beam spots. The dataset explored in this chapter covers a region of approximately $500\mu m \times 300\mu m$ with a micro focused beam size of approximately $15\mu m \times 15\mu m$.

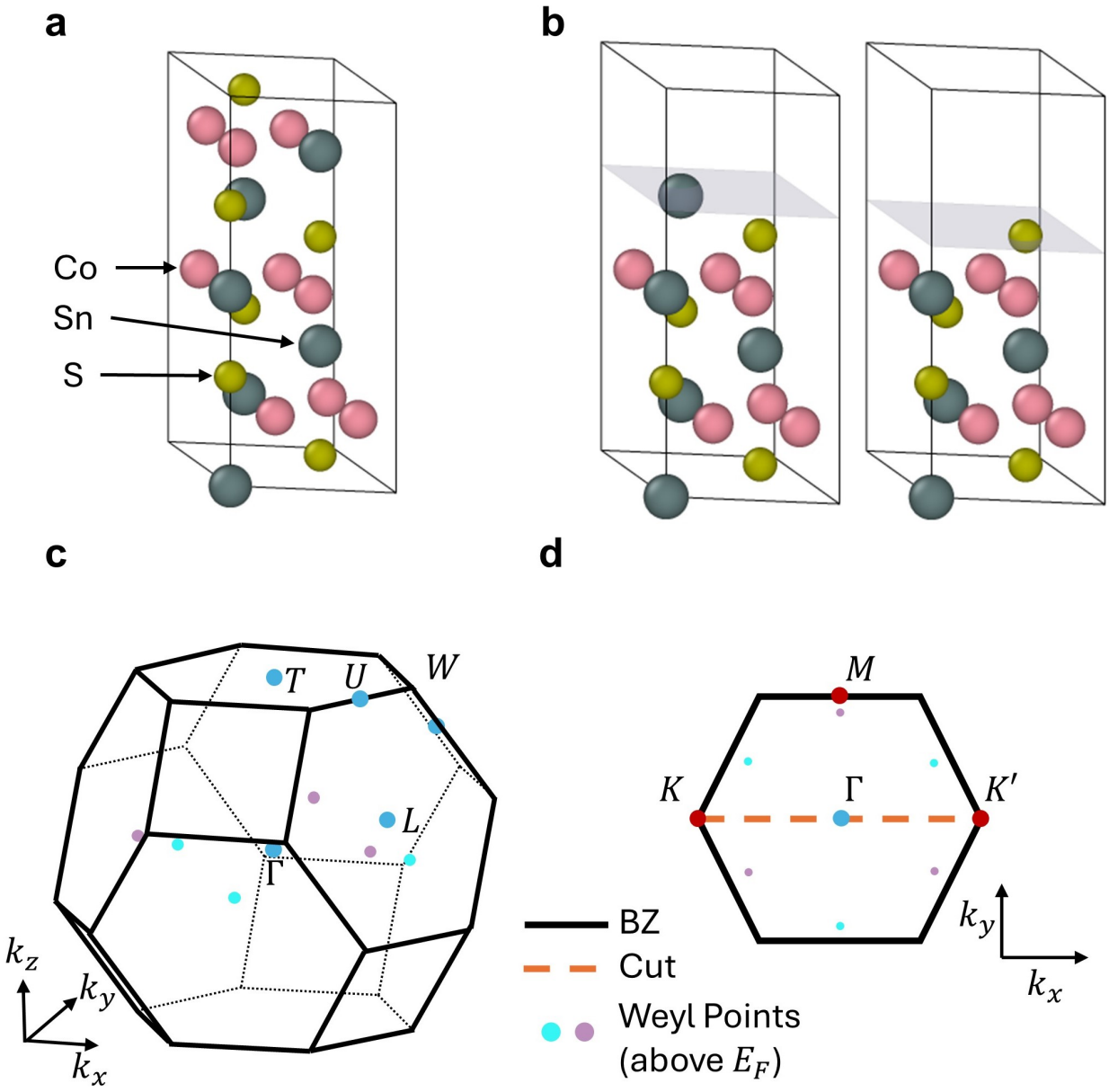

Figure 5.1: $Co_3Sn_2S_2$ crystal structure, terminations, and Brillouin zone. (a) Crystal structure of $Co_3Sn_2S_2$ with (pink, gray, yellow) spheres corresponding to the (Co, Sn, S) atoms respectively. (b) The two dominant cleavage planes. The left and right panels show the cleavage plane for the tin sulfur terminations respectively. (c) Three dimensional Brillouin zone with Weyl points and high symmetry points located. (d) Two dimensional Brillouin zone projected along the k_z direction indicating the ARPES cut orientation that was used for this study. Credit to Sudheer Sreedhar for making panels (a) and (b).

These experiments were performed at the Maestro beamline (7.0.2) at the Advanced Light Source. The importance of synchrotron light sources to modern ARPES experiments cannot be overstated. A home lab ARPES system can achieve an approximately $1cm$ spot size with a capillary on a discharge lamp such as a He discharge lamp. A micro focused beam spot is possible in a home lab with a laser light source but these have very low photon energies and cannot perform coincident XPS measurements. Currently the only way

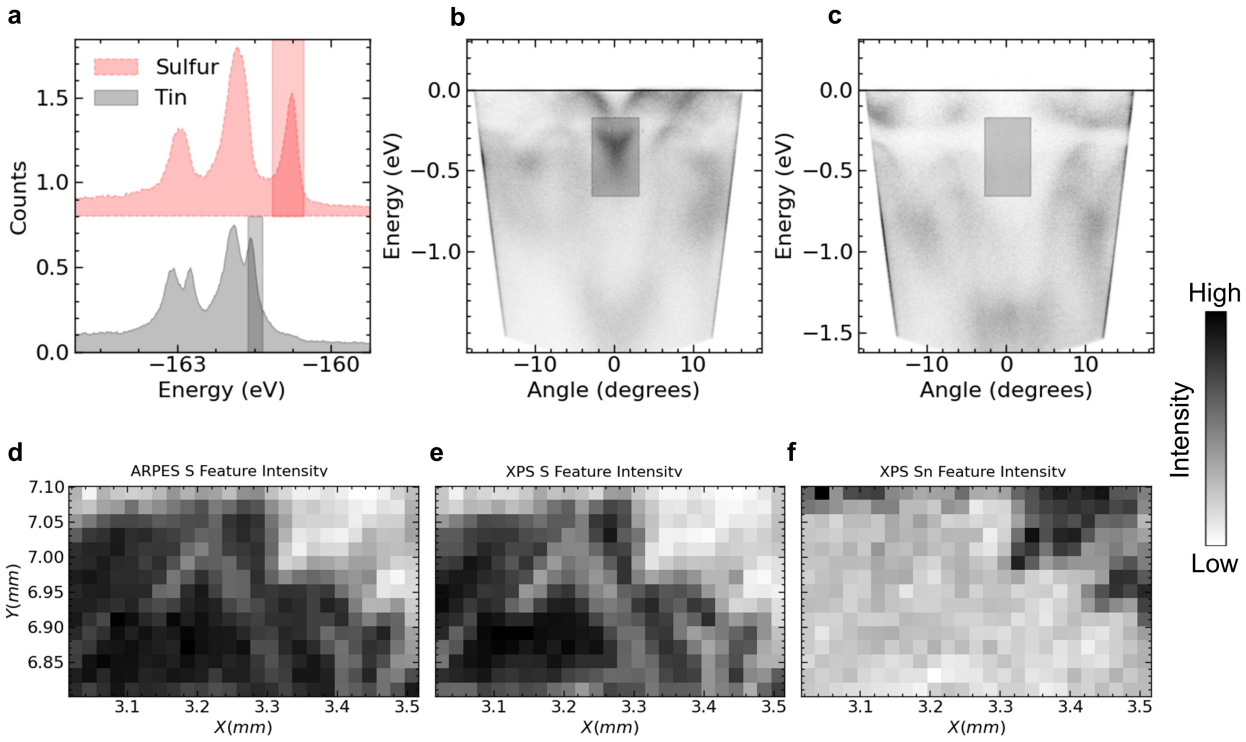

Figure 5.2: Spatial Dependence of ARPES and XPS on $Co_3Sn_2S_2$. (a) Characteristic XPS spectra of the S $2p$ core level on the terminations identified as tin (black, solid) an sulfur (Red, dashed). Gray and red shaded regions indicate the energy range that will be integrated to make spatial maps in (e) and (f) respectively. (b) Characteristic ARPES spectra of the so called sulfur termination. (c) Characteristic ARPES spectrum of the tin termination. The gray highlighted region in the center of the ARPES spectra in (b) and (c) indicate the region where intensity will be integrated to show a spatially resolved image in (d). (d) Spatially resolved image showing the intensity of the ARPES spectra in the region indicated in (b) and (c). (e) Spatially resolved intensity of the XPS spectrum integrated in the red sulfur region shown in (a). (f) Spatially resolved intensity of the XPS spectrum integrated in the gray tin region shown in (a).

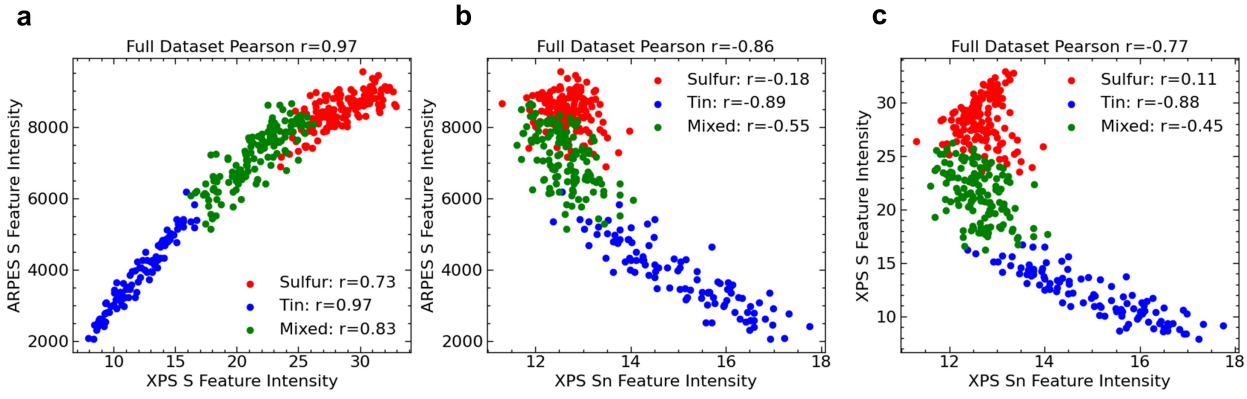

Figure 5.3: Correlation of XPS and ARPES spectral features. (a, b) The integrated intensity of the ARPES sulfur region is scatter plotted against the integrated intensity in the XPS (sulfur, tin) regions respectively. (c) A scatter plot of the integrated intensity in the XPS sulfur and tin regions. In all plots the points are colored based on a k-means clustering of the XPS spectra. The Pearson r correlations for the full dataset are shown above each panel and the cluster specific correlations are shown in the legends.

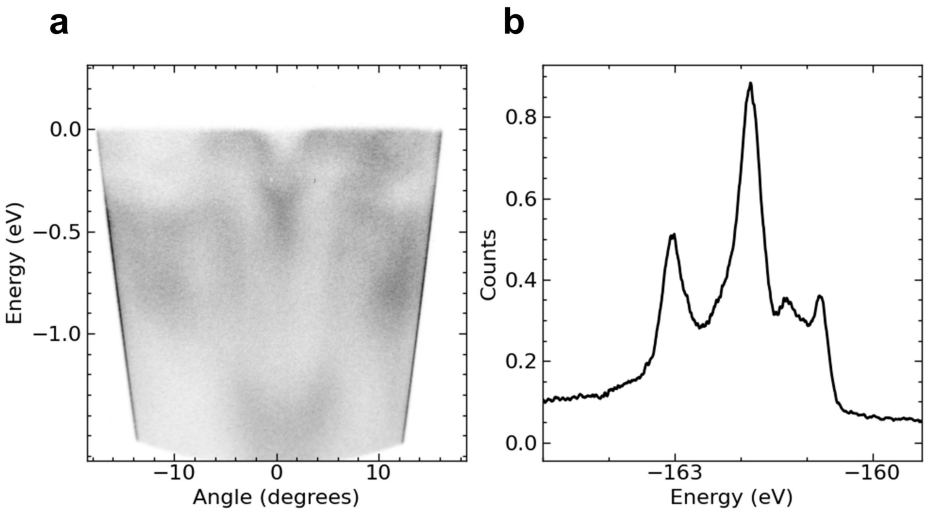

Figure 5.4: ARPES and XPS of the mixed termination. The spectra chosen to represent the mixed termination was that with the XPS spectrum closest to the mean of the mixed termination cluster using k-means clustering on the XPS data. (a) ARPES of the valence band. (b) XPS of the S 2p core level.

to perform both ARPES and XPS experiments with a micro (or nano) focused beam is using synchrotron light sources such as the Advanced Light Source or Stanford Synchrotron Radiation Lightsource.

The spatial dependence of the ARPES and XPS measurements on $Co_3Sn_2S_2$ is shown by analyzing the variations in the spectral features identified to originate from surface heterogeneity. The sulfur or tin nature of these terminations have been previously identified as such through STM, XPS, and ARPES studies and their XPS spectra have been computed with density functional theory. Figure 5.2 (a) shows characteristic XPS spectra of the S 2p core level for two distinct terminations: tin (black, solid) and sulfur (red, dashed). The other core levels we have investigated (Co 3s and 3p, Sn 4s, 4p, 4d) do not show substantial spatial variation so we will focus on the S 2p here. The regions shaded in gray and red correspond to energy ranges that are integrated to generate spatial maps in panels (e) and (f), respectively. ARPES measurements reveal distinct spectral features for the sulfur termination (b) and the tin termination (c), with the highlighted region in gray showing the specific energy and angle range from which spatially resolved intensity maps are shown (d). Panel (d) shows the ARPES intensity map of the highlighted region in (b) and (c), indicating regions identified as the sulfur termination with high intensity (black) and tin terminations with low intensity (white). Similarly, panels (e) and (f) show spatially resolved XPS intensities from the red sulfur and gray tin regions in (a), respectively. These results highlight the spatial heterogeneity of surface electronic states across the $Co_3Sn_2S_2$ cleaved surface. The visual correspondence of the ARPES map (d) and the intensity of the sulfur feature in (e) will be explored in more detail using machine learning (ML) in the following sections.

The sulfur feature identified in the ARPES data shown on panels (b, c) of Figure 5.2 belong to a surface

state of the sulfur termination. The XPS sulfur feature appears to correlate spatially to the ARPES sulfur surface state while the XPS tin feature appears to anti-correlate. The mixed region ARPES and XPS spectra are shown in Figure 5.4. The mixed termination ARPES spectrum in panel (a) is visually similar to a blurred out sulfur termination spectrum because it lacks the gap seen in the tin spectra. However, the XPS spectrum for the mixed termination shows peaks consistent with both of the pure terminations as well as distinct peaks. These distinct peaks likely originate from the variety of vacancy layouts not seen when the termination is purely tin or sulfur. In Figure 5.3 I explore the Pearson correlations of these three spectral features.

Figure 5.3 (a) demonstrates a high correlation ($r = 0.97$) between the sulfur features in the ARPES and XPS spectra. The sulfur feature correlations also hold when the dataset is clustered into (sulfur, tin, mixed) regions with Pearson correlations of $r = (0.73, 0.97, 0.83)$ respectively. The tin feature of the XPS spectra also shows an anti-correlation with the ARPES sulfur feature and XPS sulfur feature with Pearson correlations of $r = -0.86$ and $r = -0.77$ respectively. When the data are broken into clusters, the anti-correlation is strongest in the tin cluster. The only use of machine learning (ML) in these analyses was to investigate the termination dependent correlations where the XPS spectra were k-means clustered into three clusters after a transmission function and photon flux were corrected. These analyses demonstrate the correlation of the spectral features between the ARPES and XPS spectra in physically motivated way.

5.2 Machine Learning Identification of Surface Heterogeneity

5.2.1 k-Means Clustering

k-Means clustering is a method to break a dataset up into a known (k) number of groups. The algorithm for k-means operates by initially choosing k random (or sometimes educated guess) points as the centers of the clusters. All data points are then assigned to be within the cluster of the point which they are closest to. The k points are then shifted toward the mean of the data points by some distance and the cluster identification is repeated. This iterative procedure is repeated for either a fixed number of steps or until the mean points are no longer being shifted by more than some tolerance value chosen.

The reliance on measuring the distance from the mean point to all other points means that the k-means algorithm relies on a user defined metric (euclidean is the most typical). Like many other ML methods, k-means suffers from a phenomenon known as the 'curse of dimensionality' when the data points that are being clustered have many features. The curse of dimensionality can be viewed as a consequence of the euclidean distance between vectors in a higher dimensional space being more tightly distributed than those

in a low dimensional space. However, the different features in XPS (energy) and in ARPES (angle, energy) are strongly correlated with each other which reduces the effect curse of dimensionality is not as consequential as one may expect with datasets of such high dimensionality.

In this chapter I utilize k-means clustering to identify the tin, sulfur, and mixed terminations. The XPS spectra were first processed by dividing the spectra by an energy dependent transmission function. The transmission function was estimated by measuring a portion of the XPS spectrum far from any known peaks where the resulting spectrum should be roughly flat. This estimation also corrects for energy dependent sensitivity factors of the detector (detector background). Each spectrum was then normalized by the difference of the background above and below the peak complex as a proxy of the photon flux. The spectra were then fed into a k-means algorithm ($k = 3$) in order to determine the tin, sulfur, and mixed regions of the sample.

5.2.2 Dimensionality Reduction

Simple feature extraction by integrating regions of the spectra shows complex spatial variations as shown in figures 5.2 and 5.3. Machine learning - in particular dimensionality reduction methods - can provide a more general method for parameterize spectral variations with a low number of components.

The most common dimensionality reduction method known as principal component analysis (PCA) takes n datasets which have m parameters and uses linear algebra to find the specified number of most significant linearly independent components. The linear algebra performed for PCA is the same as an eigenvalue decomposition where the eigenvectors are the principal components and their significance is related to the eigenvalue. PCA being based in linear algebra can only perform linear transformations on the dataset. This linearity is sometimes considered to be a feature (e.g. when metric preservation is desired) or a drawback (e.g. when the data originates from a complex topology).

Non-linear methods for dimensionality reduction have been developed in to provide the reduction benefits of PCA while providing the ability to capture more topologically complex datasets. Uniform manifold approximation and projection (UMAP) is a non-linear dimensionality reduction method based on topological data analysis that has become an effective standard for non-linear dimensionality reduction in recent years. A deeper introduction to UMAP is given in Section 4.2.1.

Figure 5.5 shows both a PCA (a, b) and UMAP (c, d) dimensionality reduction of the XPS (a, c) and ARPES (b, d) spectra. In all panels the points are marked with a marker and color based on the cluster they have been identified to belong with. Because PCA relies on a linear transformation it can under perform other methods like UMAP for small numbers of embedding dimensions. To demonstrate this under performance, the silhouette score differences are shown in Figure 5.6. The silhouette score is a measure that

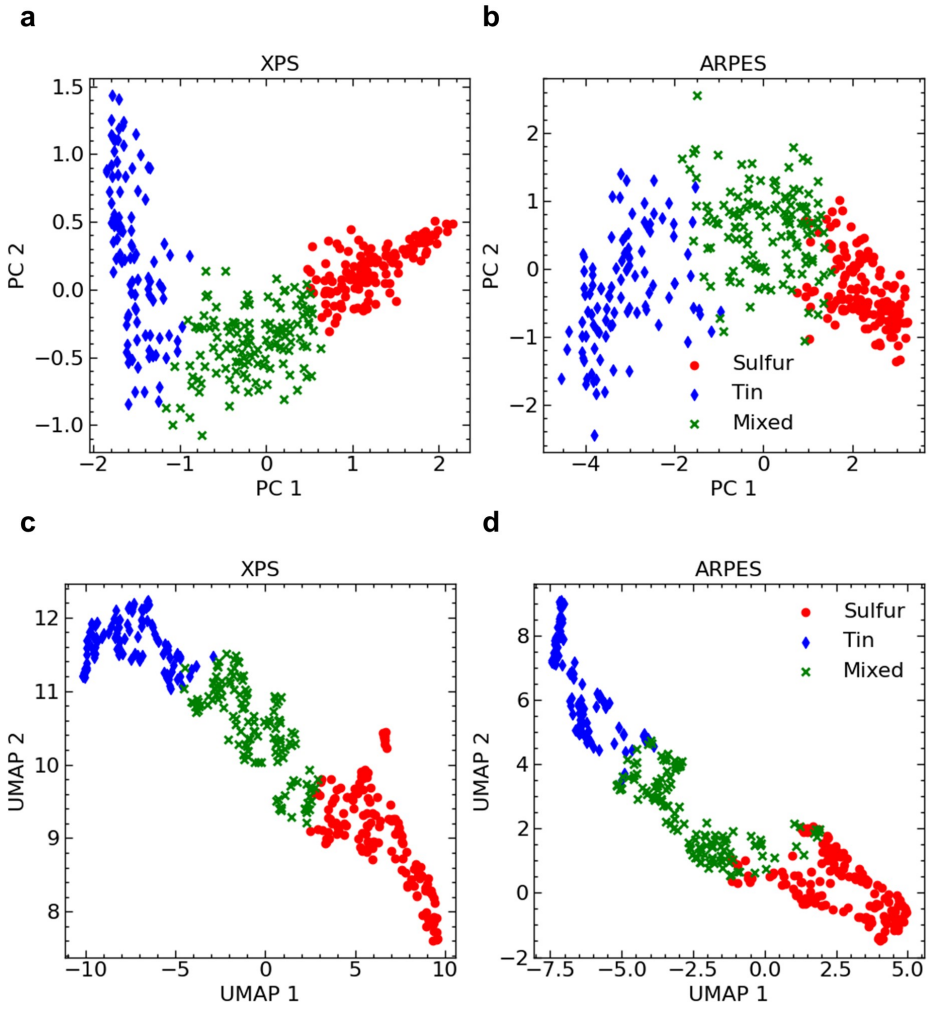

Figure 5.5: Dimensionality reduction methods applied to $Co_3Sn_2S_2$. (a, b) the (XPS, ARPES) data reduced to 2 dimensions each independently using PCA. (c, d) The (XPS, ARPES) data reduced to 2 dimensions using the UMAP algorithm. There were 375 XPS and ARPES spectra where the raw data had 1,200 and 988,800 channels respectively. The ARPES data was binned to (100,100) before performing the dimensionality reductions to aid in computational speed. In all panels the colors indicate a cluster label from a k-means clustering on the XPS spectra.

indicates how well grouped a point is to other members of its cluster while also being far from members of other clusters.

To visualize how UMAP captures spectral features that we can identify by eye we show the intensity of some spectral features as a color scale on the UMAP points in Figure 5.7. The (right, left) sections of each panel show the (XPS, ARPES) UMAP embeddings respectively. In all panels a redish-black indicates low intensity of the feature in question while blue indicates high intensity. Figure 5.7 (a) shows the whole integrated intensity of the ARPES images, the variation of ARPES intensity along the thin dimension of the ARPES UMAP demonstrates that UMAP can encode physically important features in an unsupervised manner. Panels (b, c) show the (ARPES, XPS) sulfur termination features that were indicated in Figure 5.2

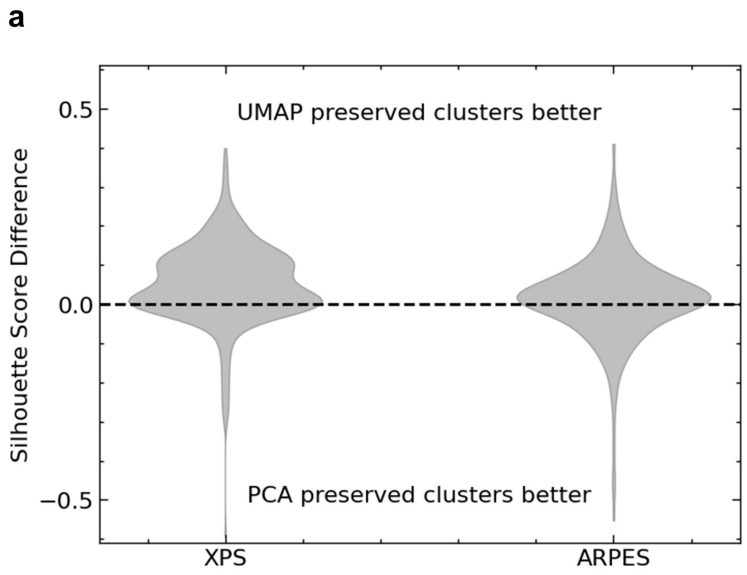

Figure 5.6: Silhouette score differences of PCA and UMAP embeddings. (a) Violin plot showing the distribution of silhouette score differences $s_{\mathrm{UMAP}} - s_{\mathrm{PCA}}$. A value greater than 0 indicates that the UMAP dimensionality reduction kept points of the same cluster closer to each other while being further from other cluster members. A value less than 0 would imply the same for PCA. A black dashed line is drawn at 0 silhouette score difference as a guide to the eye.

(a) respectively. Panel (b, right) indicates that UMAP found some features of the ARPES that are strongly correlated with the sulfur surface state as a useful variation to parameterize. Panel (c, left) indicates similar information but for the XPS sulfur feature instead of the ARPES sulfur surface state. The two feature intensities in (b, c) provide similar color maps which indicates the two features are correlated as we showed in Figure 5.3 (a). Finally Figure 5.7 (d) shows the tin feature intensity which which is anti-correlated with the XPS and ARPES features as seen in panels (b, c) and Figure 5.3 (b, c).

The UMAP colorization method described in Section 4.2.1 was also applied to the $Co_3S_2Sn_2$ dataset in Figure 5.8. Panels (a, b) show a three dimensional embedding of the (XPS, ARPES) dataset respectively. In both panels the points are colored by scaling their three UMAP coordinates to be in the range [0,1] independently and then displayed as rgb channels. This three dimensional embedding can be used to visualize the spectral variety spatially which is shown in Figure 5.9.

5.3 Analysis of ARPES and XPS Spectral Correlation

So far we have discussed three methods for visualizing spectral variation spatially using machine learning: (1) Colorization of the XPS UMAP embeddings, (2) Colorization of the ARPES UMAP embeddings, and (3) k-means clustering the XPS spectra. Figure 5.9 shows these three methods displayed spatially. Panels (a, b) show the XPS UMAP colorization embeddings of the (XPS, ARPES) data respectively. Panel (c) shows the

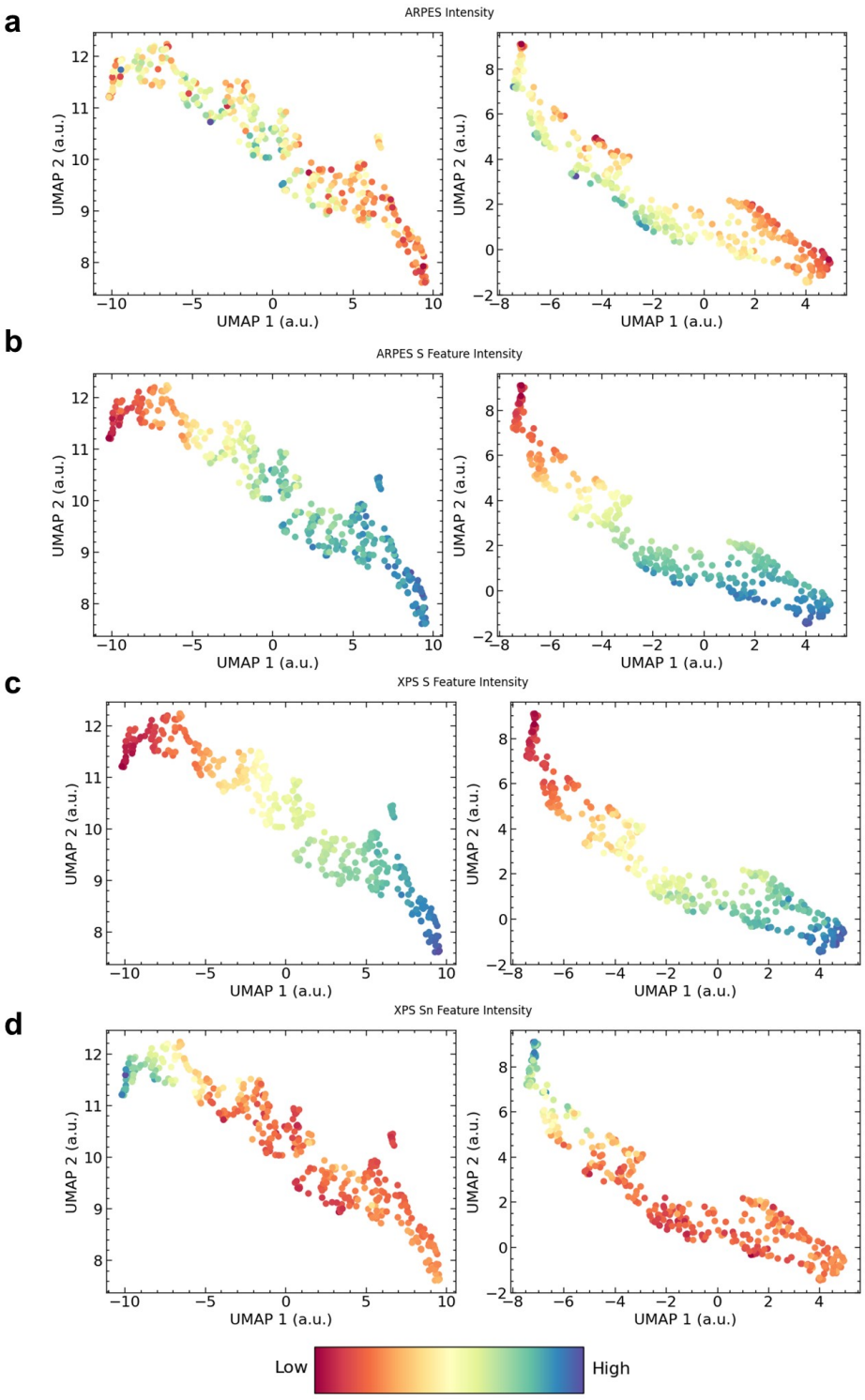

Figure 5.7: Spectral features relationship to UMAP embeddings. All plots show the UMAP embeddings from Figure 5.5 with the points colored based on different heuristics of the data. (a) The full integrated intensity of the ARPES data. (b) The ARPES intensity only in the sulfur identified region in Figure 5.2 (b,c). (c) The XPS intensity of the sulfur peak region identified in Figure 5.2 (a). The XPS intensity of the tin peak region identified in Figure 5.2 (a). The high and low of the color scale corresponds to the relevant integrated intensities discussed in each panel.

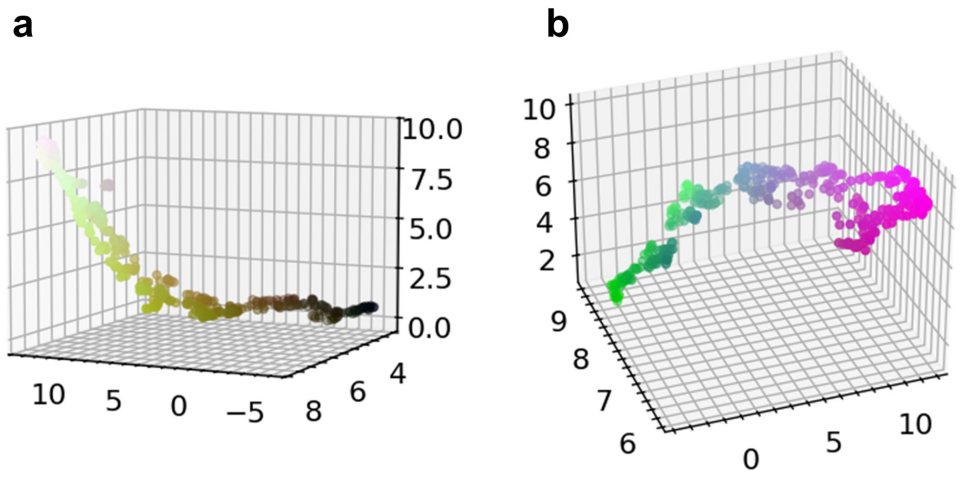

Figure 5.8: UMAP Colorization of XPS and ARPES spectra of $Co_3Sn_2S_2$. (a) XPS spectra dimensionally reduced to 3 dimensions using UMAP. (b) ARPES spectra dimensionally reduced to 3 dimensions using binning and UMAP. In both (a) and (b) the points are colored by scaling their UMAP (x, y, z) coordinates to be in the range [0, 1] and displayed as the (red, green, blue) channels respectively.

k-means clusters found by clustering the XPS spectra. The XPS UMAP colorization in panel (a) visualizes spectra consistent with the sulfur termination by a bight or white color while the tin termination spectra appear dark - intermediate murky colors are the range of mixed terminations. The ARPES UMAP resolves similar information as the XPS UMAP even though the dataset is distinct with the (pink, green) regions corresponding to spectra consistent with the (sulfur, tin) terminations and the blueish gray points indicate the mixed termination transition region. In both of the UMAP colorization cases we see an improvement in understanding the spectral variation when compared to the clustering technique. Using k-means requires prior knowledge of the correct number of clusters, while the UMAP colorization is agnostic and can work even in situations which have gradual changes instead of sharp cluster boundaries.

In order to asses the correlation in the XPS and ARPES spectra in a quantitative way, I compare the difference in spectra at distinct spatial points. If we take a pair of measurement locations and observe the absolute difference in their XPS spectra we expect their ARPES spectra to also differ. In Figure 5.10 (a) I show a scatter plot of this absolute difference for every pair of positions in our dataset. The Pearson correlation for the full dataset is $r = 0.95$ which indicates that as the XPS spectra differ from point to point so to do the ARPES spectra in a proportional manner. This correlation also holds for each category of spectra with panels (b, c, d) showing the (sulfur, tin, mixed) terminations having Pearson correlations of $r = (0.74, 0.81, 0.74)$ respectively which is summarized in panel (e). While the mixed region XPS has a series of unique peak structures due to the discrete local defect environment, the ARPES on the mixed region more resembles a blurrier and dimmer sulfur region. Such a divergence between the structure of the ARPES and XPS can be interpreted from the lower correlation of the mixed region. Similarly, the low correlation

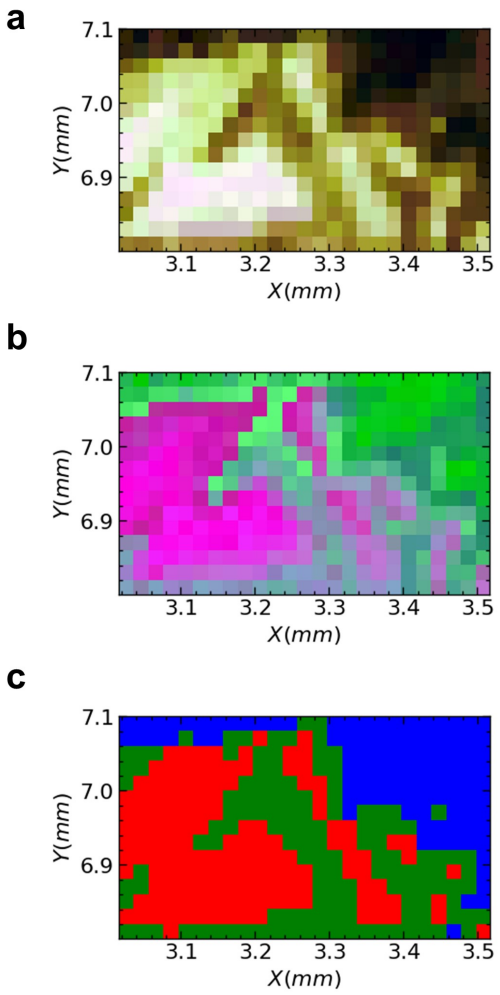

Figure 5.9: Spatial visualizations of machine learning on $Co_3Sn_2S_2$. (a, b) UMAP 3 dimensional embedding of the (XPS, ARPES) spectra visualized spatially as RGB. (c) Spatial image of k-means clustering labels of the XPS spectra where (red, green, blue) correspond to (sulfur, Mixed, and tin) termination regions respectively.

in the sulfur region there is a wide variability in the quality of the ARPES spectra for a given XPS spectra. For the tin region, a high quality XPS spectrum is more likely to indicate a high quality ARPES spectrum. The much higher correlation of the full dataset is indicative that measuring a tin or sulfur XPS spectrum is highly correlated with the expected tin or sulfur ARPES spectrum.

5.4 Conclusions

In this chapter I have shown an overview for understanding spatially dependent ARPES and XPS experiments, as well as correlating the features seen in those two. A common approach of integrating intensities in certain spectral regions of both ARPES and XPS was shown in Figure 5.2. An exploration of the correlations in the identified spectral features was shown per termination in Figure 5.3. I then demonstrated how UMAP

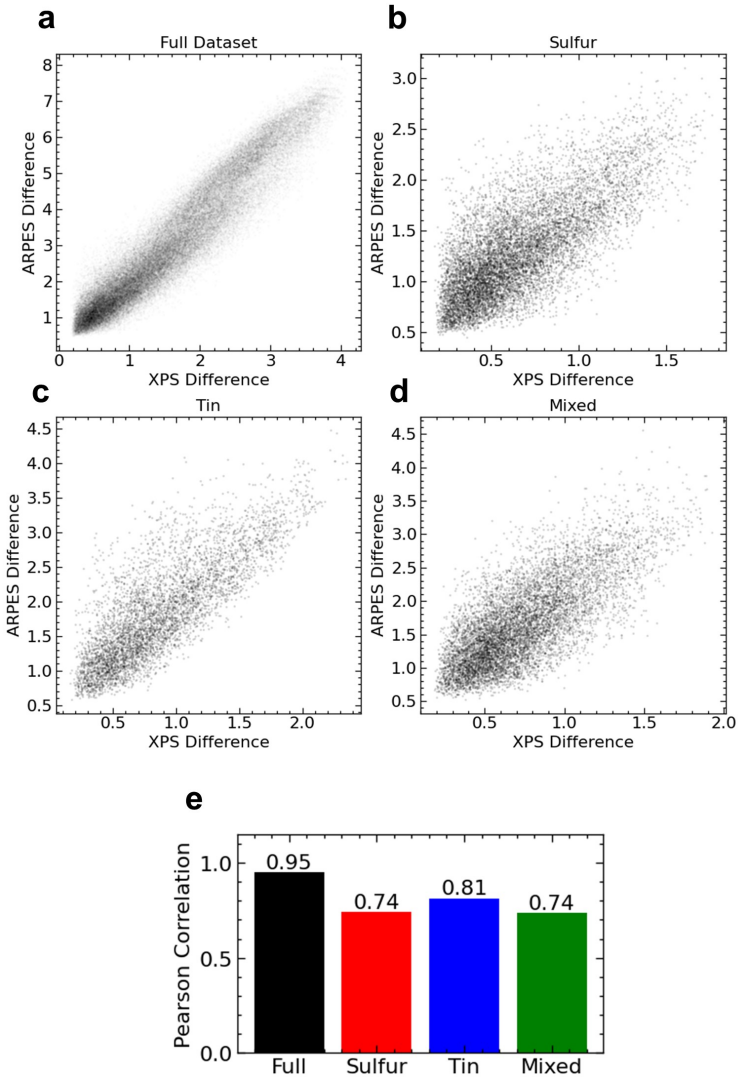

Figure 5.10: Relationship of ARPES and XPS spectra in $Co_3Sn_2S_2$. (a) Scatter plot of the difference in UMAP embeddings of the XPS and ARPES spectra for each pair of positions in the dataset. (b, c, d) Similar to (a) but for only the subset of data identified to be the (Mixed, sulfur, and tin) terminations respectively. (e) Pearson correlation coefficents for the differences in ARPES and XPS datasets shown in (a-d).

can be used to perform a non-linear dimensionality reduction and provide a more efficient packing of the data into small dimensions than the linear method of PCA in figures 5.5 and 5.6. By observing the dependence of the UMAP coordinates with traditionally understood spectral features I showed we can extract physically useful information from this unsupervised dimensionality reduction method. Using the UMAP colorization method in Figure 5.8 I demonstrate that we can get a broad understanding of the spatial heterogeneity of spectra with the visualization in Figure 5.9.

Finally I quantified the correlation in the ARPES and XPS spectra by analyzing the pairwise differences of those spectra in Figure 5.10. The correlations and difference plots are consistent with the following sense we have gathered while performing multiple experiments on this material: Performing a map of the sulfur

$2p$ core levels[1] provides a view of the sample that is highly correlated with finding desirable ARPES spectra by looking for the sharpest tin or sulfur feature in the XPS spectrum.

[1] A fixed energy window collection of this XPS is generally a faster scan than a similarly informative scan of the valence band with ARPES.

Chapter 6

Conclusions

To summarize, photoemission experiments offer a wealth of information about the electronic structure of materials and there exist both new materials and data analysis methods to explore with these techniques. ARPES has shown that the predicted symmetry enforced degeneracies of $LaNiGa_2$ do occur on the purported nodal plane. In addition, there exist many near degeneracies throughout the rest of the Brillouin zone which may support the predicted triplet pairing. XPS show that there is an increase in intensity consistent with the Ni $3d$ band providing support for the stated absence of magnetism in this Ni containing compound.

The utility of spatially resolved ARPES through micro- and nano- focused beam spots deserves to have attention drawn to it again here. Spatially resolved ARPES allowed me to measure the electronic structure in $LaNiGa_2$ along the k_y direction and demonstrate the predicted Dirac crossings throughout the purported nodal plane. This thin-edge cleave ARPES would not be possible to attain with a macroscopic beam spot as the crystals can only currently be grown in a platelet shape with the thin **b** axis only extending around 0.25mm. Further, we were able to probe the correlation between the XPS and ARPES spectra of $Co_3Sn_2S_2$ using a micro focused beam. This enabled a deeper understanding of the surface termination heterogeneity and provides a method to search for the desired ARPES spectra by understanding the relationship to the faster to collect XPS spectra.

My focus on spatially resolved photoemission spectroscopy lead me to apply for the ALS Doctoral Fellowship where I created a autonomous machine learning control for the Maestro beamline (7.0.2). This project enables users to search the spatial heterogeneity of their sample using 75% less measurements to attain a similar spatial understanding of the sample when compared to a traditional grid search. Discussions with other users of both the ALS and SSRL along with the Vishik group's experience suggest that the speedup enabled by AARDVARK could allow researchers to spend 15% more of their scarcely allotted beamtime

measuring their scientific goals instead of searching for a good location on the sample.

The information rich datasets of ARPES have successfully transformed our understanding of many materials through direct observation of the band structure. There exist many applications for modern data analysis techniques to ARPES and XPS datasets that range from neural networks, clustering algorithms, dimensionality reduction, image denoising, and many more. There is also a large phase space of parameters that can be used to tune ARPES (photon energy, temperature, strain, doping, spatial dependence, ...). This variety necessitates a population of researchers to apply these modern programming and data science principles to photoemission datasets.

Bibliography

[1] Jackson R. Badger, Yundi Quan, Matthew C. Staab, Shuntaro Sumita, Antonio Rossi, Kasey P. Devlin, Kelly Neubauer, Daniel S. Shulman, James C. Fettinger, Peter Klavins, Susan M. Kauzlarich, Dai Aoki, Inna M. Vishik, Warren E. Pickett, and Valentin Taufour. Dirac lines and loop at the fermi level in the time-reversal symmetry breaking superconductor $LaNiGa_2$. *Communications Physics*, 5, 12 2022.

[2] Matthew Staab, Robert Prater, Sudheer Sreedhar, Journey Byland, Eliana Mann, Davis Zackaria, Yunshu Shi, Henry J. Bowman, Andrew L. Stephens, Myung-Chul Jung, Antia S. Botana, Warren E. Pickett, Valentin Taufour, and Inna Vishik. Symmetry-enforced fermi surface degeneracies observed in the purported time-reversal symmetry-broken superconductor $LaNiGa_2$. *Phys. Rev. B*, 110:165115, Oct 2024.

[3] Nobel Prize Outreach. The nobel prize in physics 1921, 1921.

[4] Andrea Damascelli. Probing the electronic structure of complex systems by arpes. *Physica Scripta*, 2004(T109):61, Jan 2004.

[5] Jonathan A. Sobota, Yu He, and Zhi-Xun Shen. Angle-resolved photoemission studies of quantum materials. *Rev. Mod. Phys.*, 93:025006, May 2021.

[6] Andrea Damascelli, Zahid Hussain, and Zhi-Xun Shen. Angle-resolved photoemission studies of the cuprate superconductors. *Rev. Mod. Phys.*, 75:473–541, Apr 2003.

[7] C. N. Berglund and W. E. Spicer. Photoemission studies of copper and silver: Theory. *Phys. Rev.*, 136:A1030–A1044, Nov 1964.

[8] M. P. Seah and W. A. Dench. Quantitative electron spectroscopy of surfaces: A standard data base for electron inelastic mean free paths in solids. *Surface and Interface Analysis*, 1(1):2–11, 1979.

[9] V.N. Strocov. Intrinsic accuracy in 3-dimensional photoemission band mapping. *Journal of Electron Spectroscopy and Related Phenomena*, 130(1):65–78, 2003.

[10] H. Shinotsuka, S. Tanuma, C. J. Powell, and D. R. Penn. Calculations of electron inelastic mean free paths. x. data for 41 elemental solids over the 50ev to 200kev range with the relativistic full penn algorithm. *Surface and Interface Analysis*, 47(9):871–888, 2015.

[11] D. Geelen, J. Jobst, E. E. Krasovskii, S. J. van der Molen, and R. M. Tromp. Nonuniversal transverse electron mean free path through few-layer graphene. *Phys. Rev. Lett.*, 123:086802, Aug 2019.

[12] R. Zdyb, T. O. Menteş, A. Locatelli, M. A. Niño, and E. Bauer. Inelastic mean free path from reflectivity of slow electrons. *Phys. Rev. B*, 87:075436, Feb 2013.

[13] Liang Fu and C. L. Kane. Topological insulators with inversion symmetry. *Phys. Rev. B*, 76:045302, Jul 2007.

[14] D. Hsieh, D. Qian, L. Wray, Y. Xia, Y. S. Hor, R. J. Cava, and M. Z. Hasan. A topological Dirac insulator in a quantum spin hall phase. *Nature*, 452(7190):970–974, Apr 2008.

[15] D. Hsieh, Y. Xia, D. Qian, L. Wray, J. H. Dil, F. Meier, J. Osterwalder, L. Patthey, J. G. Checkelsky, N. P. Ong, A. V. Fedorov, H. Lin, A. Bansil, D. Grauer, Y. S. Hor, R. J. Cava, and M. Z. Hasan. A tunable topological insulator in the spin helical Dirac transport regime. *Nature*, 460(7259):1101–1105, Aug 2009.

[16] Y. Xia, D. Qian, D. Hsieh, L. Wray, A. Pal, H. Lin, A. Bansil, D. Grauer, Y. S. Hor, R. J. Cava, and M. Z. Hasan. Observation of a large-gap topological-insulator class with a single Dirac cone on the surface. *Nature Physics*, 5(6):398–402, Jun 2009.

[17] Haijun Zhang, Chao-Xing Liu, Xiao-Liang Qi, Xi Dai, Zhong Fang, and Shou-Cheng Zhang. Topological insulators in bi2se3, bi2te3 and sb2te3 with a single Dirac cone on the surface. *Nature Physics*, 5(6):438–442, Jun 2009.

[18] Y. L. Chen, J. G. Analytis, J.-H. Chu, Z. K. Liu, S.-K. Mo, X. L. Qi, H. J. Zhang, D. H. Lu, X. Dai, Z. Fang, S. C. Zhang, I. R. Fisher, Z. Hussain, and Z.-X. Shen. Experimental realization of a three-dimensional topological insulator, bi¡sub¿2¡/sub¿te¡sub¿3¡/sub¿. *Science*, 325(5937):178–181, 2009.

[19] Yi Zhang, Ke He, Cui-Zu Chang, Can-Li Song, Li-Li Wang, Xi Chen, Jin-Feng Jia, Zhong Fang, Xi Dai, Wen-Yu Shan, Shun-Qing Shen, Qian Niu, Xiao-Liang Qi, Shou-Cheng Zhang, Xu-Cun Ma, and Qi-Kun Xue. Crossover of the three-dimensional topological insulator bi2se3 to the two-dimensional limit. *Nature Physics*, 6(8):584–588, Aug 2010.

[20] S. A. Sreedhar, A. Rossi, J. Nayak, Z. W. Anderson, Y. Tang, B. Gregory, M. Hashimoto, D.-H. Lu, E. Rotenberg, R. J. Birgeneau, M. Greven, M. Yi, and I. M. Vishik. Three interaction energy scales in the single-layer high-T_c cuprate $Hgba_2Cuo_{4+\delta}$. *Phys. Rev. B*, 102:205109, Nov 2020.

[21] Sung-Kwan Mo. Angle-resolved photoemission spectroscopy for the study of two-dimensional materials. *Nano Convergence*, 4(1):6, Mar 2017.

[22] Chan young Lim, Sunghun Kim, Sung Won Jung, Jinwoong Hwang, and Yeongkwan Kim. Recent technical advancements in arpes: Unveiling quantum materials. *Current Applied Physics*, 60:43–56, 2024.

[23] Haifeng Yang, Aiji Liang, Cheng Chen, Chaofan Zhang, Niels B. M. Schroeter, and Yulin Chen. Visualizing electronic structures of quantum materials by angle-resolved photoemission spectroscopy. *Nature Reviews Materials*, 3(9):341–353, Sep 2018.

[24] Yongqiang Kang, Guangning Wu, Xueqin Zhang, Yijie Liu, Chaoqun Shi, Wenfu Wei, and Guoqiang Gao. Verification and analysis of flowing gas discharge – part ii. *IEEE Transactions on Dielectrics and Electrical Insulation*, 26(4):1056–1064, 2019.

[25] B. Keimer and J. E. Moore. The physics of quantum materials. *Nature Physics*, 13(11):1045–1055, Nov 2017.

[26] D. N. Basov, R. D. Averitt, and D. Hsieh. Towards properties on demand in quantum materials. *Nature Materials*, 16(11):1077–1088, Nov 2017.

[27] Oskar Vafek and Ashvin Vishwanath. Dirac fermions in solids: From high-tc cuprates and graphene to topological insulators and Weyl semimetals. *Annual Review of Condensed Matter Physics*, 5(Volume 5, 2014):83–112, 2014.

[28] M. Z. Hasan and C. L. Kane. Colloquium: Topological insulators. *Rev. Mod. Phys.*, 82:3045–3067, Nov 2010.

[29] Joel E. Moore. The birth of topological insulators. *Nature*, 464(7286):194–198, Mar 2010.

[30] A.M. Black-Schaffer T.O. Wehling and A.V. Balatsky. Dirac materials. *Advances in Physics*, 63(1):1–76, 2014.

[31] Viktor Ariel. Effective mass and energy-mass relationship, 2012.

[32] Viktor Ariel and Amir Natan. Electron effective mass in graphene, 2012.

[33] Alexander S. Mayorov, Roman V. Gorbachev, Sergey V. Morozov, Liam Britnell, Rashid Jalil, Leonid A. Ponomarenko, Peter Blake, Kostya S. Novoselov, Kenji Watanabe, Takashi Taniguchi, and A. K. Geim. Micrometer-scale ballistic transport in encapsulated graphene at room temperature. *Nano Letters*, 11(6):2396–2399, 2011. PMID: 21574627.

[34] Adam L Gross, Lorenz Falling, Matthew C Staab, Metzli I Montero, Rahim R Ullah, David M Nisson, Peter Klavins, Kristie J Koski, Nicholas J Curro, Valentin Taufour, Slavomir Nemsak, and Inna M Vishik. Copper migration and surface oxidation of $Cu_xBi_2Se_3$ in ambient pressure environments. *Journal of Physics: Materials*, 5(4):044005, Oct 2022.

[35] Yundi Quan, Valentin Taufour, and Warren E. Pickett. Nonsymmorphic band sticking in a topological superconductor. *Physical Review B*, 105, 2 2022.

[36] N. P. Armitage, E. J. Mele, and Ashvin Vishwanath. Weyl and Dirac semimetals in three-dimensional solids. *Rev. Mod. Phys.*, 90:015001, Jan 2018.

[37] B. Q. Lv, H. M. Weng, B. B. Fu, X. P. Wang, H. Miao, J. Ma, P. Richard, X. C. Huang, L. X. Zhao, G. F. Chen, Z. Fang, X. Dai, T. Qian, and H. Ding. Experimental discovery of Weyl semimetal taas. *Phys. Rev. X*, 5:031013, Jul 2015.

[38] Antonio Rossi, Vsevolod Ivanov, Sudheer Sreedhar, Adam L. Gross, Zihao Shen, Eli Rotenberg, Aaron Bostwick, Chris Jozwiak, Valentin Taufour, Sergey Y. Savrasov, and Inna M. Vishik. Electronic structure and topology across T_c in the magnetic Weyl semimetal $Co_3Sn_2S_2$. *Phys. Rev. B*, 104:155115, Oct 2021.

[39] Sean Howard, Lin Jiao, Zhenyu Wang, Noam Morali, Rajib Batabyal, Pranab Kumar-Nag, Nurit Avraham, Haim Beidenkopf, Praveen Vir, Enke Liu, Chandra Shekhar, Claudia Felser, Taylor Hughes, and Vidya Madhavan. Evidence for one-dimensional chiral edge states in a magnetic Weyl semimetal $Co_3Sn_2S_2$. *Nature Communications*, 12(1):4269, Jul 2021.

[40] Lukas Muechler, Enke Liu, Jacob Gayles, Qiunan Xu, Claudia Felser, and Yan Sun. Emerging chiral edge states from the confinement of a magnetic Weyl semimetal in $co_3sn_2s_2$. *Phys. Rev. B*, 101:115106, Mar 2020.

[41] Shama, R.K. Gopal, and Yogesh Singh. Observation of planar hall effect in the ferromagnetic Weyl semimetal $Co_3Sn_2S_2$. *Journal of Magnetism and Magnetic Materials*, 502:166547, 2020.

[42] M. Kanagaraj, Jiai Ning, and Liang He. Topological $Co_3Sn_2S_2$ magnetic Weyl semimetal: From fundamental understanding to diverse fields of study. *Reviews in Physics*, 8:100072, 2022.

[43] Shuo-Ying Yang, Jonathan Noky, Jacob Gayles, Fasil Kidane Dejene, Yan Sun, Mathias Dörr, Yurii Skourski, Claudia Felser, Mazhar Nawaz Ali, Enke Liu, and Stuart S. P. Parkin. Field-modulated anomalous hall conductivity and planar hall effect in $Co_3Sn_2S_2$ nanoflakes. *Nano Letters*, 20(11):7860–7867, Nov 2020.

[44] Hongyi Sun and Qihang Liu. Boosting the intrinsic anomalous hall effect through a topological phase transition in the magnetic Weyl semimetal $Co_3Sn_2S_2$. *Phys. Rev. B*, 107:205138, May 2023.

[45] A. A. Kordyuk. Iron-based superconductors: Magnetism, superconductivity, and electronic structure (review article). *Low Temperature Physics*, 38:888–899, 9 2012.

[46] V. B. Zabolotnyy, D. S. Inosov, D. V. Evtushinsky, A. Koitzsch, A. A. Kordyuk, G. L. Sun, J. T. Park, D. Haug, V. Hinkov, A. V. Boris, C. T. Lin, M. Knupfer, A. N. Yaresko, B. Büchner, A. Varykhalov, R. Follath, and S. V. Borisenko. (π, π) electronic order in iron arsenide superconductors. *Nature*, 457:569–572, 1 2009.

[47] Eduardo Fradkin and Steven A. Kivelson. Ineluctable complexity. *Nature Physics*, 8(12):864–866, 2012.

[48] Makoto Hashimoto, Inna M. Vishik, Rui-Hua He, Thomas P. Devereaux, and Zhi-Xun Shen. Energy gaps in high-transition-temperature cuprate superconductors. *Nature Physics*, 10(7):483–495, 2014.

[49] T. Yokoya, A. Chainani, T. Takahashi, H. Katayama-Yoshida, M. Kasai, and Y. Tokura. Extended van hove singularity in a noncuprate layered superconductor Sr_2RuO_4. *Phys. Rev. Lett.*, 76:3009–3012, Apr 1996.

[50] Q. H. Wang, C. Platt, Y. Yang, C. Honerkamp, F. C. Zhang, W. Hanke, T. M. Rice, and R. Thomale. Theory of superconductivity in a three-orbital model of Sr_2RuO_4. *Europhysics Letters*, 104(1):17013, Nov 2013.

[51] Veronika Sunko, Edgar Abarca Morales, Igor Marković, Mark E. Barber, Dijana Milosavljević, Federico Mazzola, Dmitry A. Sokolov, Naoki Kikugawa, Cephise Cacho, Pavel Dudin, Helge Rosner, Clifford W. Hicks, Philip D. C. King, and Andrew P. Mackenzie. Direct observation of a uniaxial stress-driven lifshitz transition in Sr_2RuO_4. *npj Quantum Materials*, 4(1):46, 2019.

[52] T. Shang, M. Smidman, S. K. Ghosh, C. Baines, L. J. Chang, D. J. Gawryluk, J. A. T. Barker, R. P. Singh, D. McK. Paul, G. Balakrishnan, E. Pomjakushina, M. Shi, M. Medarde, A. D. Hillier, H. Q. Yuan, J. Quintanilla, J. Mesot, and T. Shiroka. Time-reversal symmetry breaking in Re-based superconductors. *Phys. Rev. Lett.*, 121:257002, Dec 2018.

[53] Sudeep Kumar Ghosh, Michael Smidman, Tian Shang, James F Annett, Adrian D Hillier, Jorge Quintanilla, and Huiqiu Yuan. Recent progress on superconductors with time-reversal symmetry breaking. *Journal of Physics: Condensed Matter*, 33(3):033001, Oct 2020.

[54] Astrid T. Rømer, Andreas Kreisel, Marvin A. Müller, P. J. Hirschfeld, Ilya M. Eremin, and Brian M. Andersen. Theory of strain-induced magnetic order and splitting of T_c and T_{TRSB} in Sr_2RuO_4. *Phys. Rev. B*, 102:054506, Aug 2020.

[55] D Aoki, J-P Brison, J Flouquet, K Ishida, G Knebel, Y Tokunaga, and Y Yanase. Unconventional superconductivity in UTe_2. *Journal of Physics: Condensed Matter*, 34(24):243002, Apr 2022.

[56] Camron Farhang, Nader Zaki, Jingyuan Wang, Genda Gu, Peter D. Johnson, and Jing Xia. Revealing the origin of time-reversal symmetry breaking in Fe-chalcogenide superconductor $FeTe_{1-x}Se_x$. *Phys. Rev. Lett.*, 130:046702, Jan 2023.

[57] David J. Singh. Electronic structure and fermiology of superconducting $LaNiGa_2$. *Physical Review B - Condensed Matter and Materials Physics*, 86, 11 2012.

[58] N. L. Zeng and W. H. Lee. Superconductivity in the Ni-based ternary compound $LaNiGa_2$. *Physical Review B - Condensed Matter and Materials Physics*, 66:1–3, 2002.

[59] A. D. Hillier, J. Quintanilla, B. Mazidian, J. F. Annett, and R. Cywinski. Nonunitary triplet pairing in the centrosymmetric superconductor $LaNiGa_2$. *Physical Review Letters*, 109, 8 2012.

[60] Han Gyeol Suh, Yue Yu, Tatsuya Shishidou, Michael Weinert, P. M. R. Brydon, and Daniel F. Agterberg. Superconductivity of anomalous pseudospin in nonsymmorphic materials. *Phys. Rev. Res.*, 5:033204, Sep 2023.

[61] Zhanyang Hao, Weizhao Chen, Yuan Wang, Jiayu Li, Xiao Ming Ma, Yu Jie Hao, Ruie Lu, Zecheng Shen, Zhicheng Jiang, Wanling Liu, Qi Jiang, Yichen Yang, Xiao Lei, Le Wang, Ying Fu, Liang Zhou, Lianglong Huang, Zhengtai Liu, Mao Ye, Dawei Shen, Jiawei Mei, Hongtao He, Cai Liu, Ke Deng, Chang Liu, Qihang Liu, and Chaoyu Chen. Multiple Dirac nodal lines in an in-plane anisotropic semimetal. *Physical Review B*, 104, 9 2021.

[62] Shaozhu Xiao, Wen-He Jiao, Yu Lin, Qi Jiang, Xiufu Yang, Yunpeng He, Zhicheng Jiang, Yichen Yang, Zhengtai Liu, Mao Ye, Dawei Shen, and Shaolong He. Dirac nodal lines in the quasi-one-dimensional ternary Telluride $TaPtTe_5$. *Physical Review B*, 105, 5 2022.

[63] Peter Blaha, Karlheinz Schwarz, Fabien Tran, Robert Laskowski, Georg K. H. Madsen, and Laurence D. Marks. WIEN2k: An APW+lo program for calculating the properties of solids. *The Journal of Chemical Physics*, 152(7):074101, 2020.

[64] John P. Perdew, Kieron Burke, and Matthias Ernzerhof. Generalized gradient approximation made simple. *Phys. Rev. Lett.*, 77:3865–3868, Oct 1996.

[65] P. Sherpa, I. Vinograd, Y. Shi, S. A. Sreedhar, C. Chaffey, T. Kissikov, M.-C. Jung, A. S. Botana, A. P. Dioguardi, R. Yamamoto, M. Hirata, G. Conti, S. Nemsak, J. R. Badger, P. Klavins, I. Vishik, V. Taufour, and N. J. Curro. Absence of strong magnetic fluctuations or interactions in the normal state of $LaNiGa_2$. *Phys. Rev. B*, 109:125113, Mar 2024.

[66] Simon Moser. An experimentalist's guide to the matrix element in angle resolved photoemission. *Journal of Electron Spectroscopy and Related Phenomena*, 214:29–52, 2017.

[67] S. Tanuma, C.J. Powell, and D.R. Penn. Proposed formula for electron inelastic mean free paths based on calculations for 31 materials. *Surface Science*, 192(1):L849–L857, 1987.

[68] Z. F. Weng, J. L. Zhang, M. Smidman, T. Shang, J. Quintanilla, J. F. Annett, M. Nicklas, G. M. Pang, L. Jiao, W. B. Jiang, Y. Chen, F. Steglich, and H. Q. Yuan. Two-gap superconductivity in $LaNiGa_2$ with nonunitary triplet pairing and even parity gap symmetry. *Physical Review Letters*, 117, 7 2016.

[69] Shyam Sundar, M. Yakovlev, N. Azari, M. Abedi, D. M. Broun, H. U. Özdemir, S. R. Dunsiger, D. Zackaria, H. Bowman, P. Klavins, Y. Shi, V. Taufour, and J. E. Sonier. Gap structure of the nonsymmorphic superconductor $LaNiGa_2$ probed by μSR. *Phys. Rev. B*, 109:104517, Mar 2024.

[70] Sudeep Kumar Ghosh, Gábor Csire, Philip Whittlesea, James F. Annett, Martin Gradhand, Balázs Újfalussy, and Jorge Quintanilla. Quantitative theory of triplet pairing in the unconventional superconductor $LaNiGa_2$. *Physical Review B*, 101, 3 2020.

[71] Shyam Sundar, M. Yakovlev, N. Azari, M. Abedi, D. M. Broun, H. U. Ozdemir, S. R. Dunsiger, D. Zackaria, V. Taufour, and J. E. Sonier. Gap structure of the non-symmorphic superconductor $LaNiGa_2$ probed by μSR. *arXiv preprint arXiv:2311.00069*, 2023.

[72] S. Ghimire, K. R. Joshi, E. H. Krenkel, M. A. Tanatar, Yunshu Shi, M. Konczykowski, R. Grasset, V. Taufour, P. P. Orth, M. S. Scheurer, and R. Prozorov. Electron irradiation reveals robust fully gapped superconductivity in $LaNiGa_2$. *arXiv preprint arXiv:2311.12222*, 2023.

[73] H. M. Tütüncü and G. P. Srivastava. Origin of superconductivity in layered centrosymmetric $LaNiGa_2$. *Applied Physics Letters*, 104(2), 2014.

[74] J. F. Landaeta, D. Subero, P. Machado, F. Honda, and I. Bonalde. Unconventional superconductivity and an ambient-pressure magnetic quantum critical point in single-crystal $LaNiC_2$. *Phys. Rev. B*, 96:174515, Nov 2017.

[75] A. Pustogow, Yongkang Luo, A. Chronister, Y. S. Su, D. A. Sokolov, F. Jerzembeck, A. P. Mackenzie, C. W. Hicks, N. Kikugawa, S. Raghu, E. D. Bauer, and S. E. Brown. Constraints on the superconducting order parameter in Sr_2RuO_4 from Oxygen-17 nuclear magnetic resonance. *Nature*, 574(7776):72–75, 2019.

[76] Aaron Chronister, Andrej Pustogow, Naoki Kikugawa, Dmitry A. Sokolov, Fabian Jerzembeck, Clifford W. Hicks, Andrew P. Mackenzie, Eric D. Bauer, and Stuart E. Brown. Evidence for even parity unconventional superconductivity in Sr_2RuO_4. *Proceedings of the National Academy of Sciences*, 118(25):e2025313118, 2021.

[77] Leland McInnes, John Healy, and James Melville. UMAP: Uniform manifold approximation and projection for dimension reduction. 2020.

[78] Corey J. Nolet, Victor Lafargue, Edward Raff, Thejaswi Nanditale, Tim Oates, John Zedlewski, and Joshua Patterson. Bringing UMAP closer to the speed of light with GPU acceleration, 2021.

[79] RAPIDS Development Team. *RAPIDS: Libraries for End to End GPU Data Science*, 2023.

[80] Jacob Gardner, Geoff Pleiss, Kilian Q Weinberger, David Bindel, and Andrew G Wilson. Gpytorch: Blackbox matrix-matrix gaussian process inference with GPU acceleration. 31, 2018.

[81] Jie Wang. An intuitive tutorial to gaussian process regression. *Computing in Science Engineering*, 25(4):4–11, 2023.

[82] Carl Edward Rasmussen and Christopher K. I. Williams. *Gaussian Processes for Machine Learning*. The MIT Press, 11 2005.

[83] Edwin V Bonilla, Kian Chai, and Christopher Williams. Multi-task gaussian process prediction. 20, 2007.

[84] Charles N Melton, Marcus M Noack, Taisuke Ohta, Thomas E Beechem, Jeremy Robinson, Xiaotian Zhang, Aaron Bostwick, Chris Jozwiak, Roland J Koch, Petrus H Zwart, Alexander Hexemer and Eli Rotenberg. K-means-driven gaussian process data collection for angle-resolved photoemission spectroscopy. *Machine Learning: Science and Technology*, 1(4), 2020.

[85] Steinn Ýmir Ágústsson, Alfred J. H. Jones, Davide Curcio, Søren Ulstrup, Jill Miwa, Davide Mottin, Panagiotis Karras, and Philip Hofmann. Autonomous micro-focus angle-resolved photoemission spectroscopy. *Review of Scientific Instruments*, 95(5):055106, 05 2024.

[86] Saugat Kandel, Tao Zhou, Anakha V. Babu, Zichao Di, Xinxin Li, Xuedan Ma, Martin Holt, Antonino Miceli, Charudatta Phatak, and Mathew J. Cherukara. Demonstration of an ai-driven workflow for autonomous high-resolution scanning microscopy. *Nature Communications*, 14(1):5501, 2023.

[87] Noam Morali, Rajib Batabyal, Pranab Kumar Nag, Enke Liu, Qiunan Xu, Yan Sun, Binghai Yan, Claudia Felser, Nurit Avraham, and Haim Beidenkopf. Fermi-arc diversity on surface terminations of the magnetic Weyl semimetal $Co_3Sn_2S_2$. *Science*, 365(6459):1286–1291, 2019.

[88] Guowei Liu, Tianyu Yang, Yu-Xiao Jiang, Shafayat Hossain, Hanbin Deng, M. Zahid Hasan, and Jia-Xin Yin. Perspective: imaging atomic step geometry to determine surface terminations of kagome materials and beyond. *Quantum Frontiers*, 3(1):19, Sep 2024.

[89] Federico Mazzola, Stefan Enzner, Philipp Eck, Chiara Bigi, Matteo Jugovac, Iulia Cojocariu, Vitaliy Feyer, Zhixue Shu, Gian Marco Pierantozzi, Alessandro De Vita, Pietro Carrara, Jun Fujii, Phil D. C. King, Giovanni Vinai, Pasquale Orgiani, Cephise Cacho, Matthew D. Watson, Giorgio Rossi, Ivana Vobornik, Tai Kong, Domenico Di Sante, Giorgio Sangiovanni, and Giancarlo Panaccione. Observation of termination-dependent topological connectivity in a magnetic Weyl kagome lattice. *Nano Letters*, 23(17):8035–8042, Sep 2023.